Politecnico di Torino

ScuDo
Scuola di Dottorato ~ Doctoral School
WHAT YOU ARE, TAKES YOU FAR

Doctoral Dissertation
Doctoral Program in Physics (38^{th}cycle)

Modelling the neutron radiation environment of HTS magnets in thermonuclear fusion reactors

By

Federico Ledda

******

Supervisor(s):
Prof. Francesco Laviano, Supervisor
Dr. Daniele Torsello, Co-Supervisor

Doctoral Examination Committee:

Politecnico di Torino
2026

Declaration

I hereby declare that, the contents and organization of this dissertation constitute my own original work and does not compromise in any way the rights of third parties, including those relating to the security of personal data.

Federico Ledda
2026

* This dissertation is presented in partial fulfillment of the requirements for **Ph.D. degree** in the Graduate School of Politecnico di Torino (ScuDo).

I would like to dedicate this thesis to my loving parents

Acknowledgements

The years of my PhD have been among the most interesting, stimulating, and exciting of my life, and I would like to sincerely thank all the people who helped and supported me during this journey.

First of all, I would like to sincerely thank my supervisor, Professor Francesco Laviano, for his guidance, suggestions, continuous availability, and constant support throughout my PhD. The freedom he gave me to explore different fields of physics and different academic environments, while supporting me in several research visits, made this period extremely stimulating.

I would also like to sincerely thank my co-supervisor, Dr. Daniele Torsello, who spent a great amount of energy keeping me on track, helping me avoid dispersing my efforts and continuously pushing me to improve the quality of my work.

A special thanks goes to Dr. Davide Gambino, for acting as co-supervisor, teaching me the fundamentals of computational physics, supporting me during the most challenging periods, and hosting me for much longer than originally agreed in Sweden and Finland.

This period would not have been the same without the precious company of my colleagues and friends: Simone Sparacio, who introduced me to PhD life when I started and when there were only the two of us; Niccolò di Eugenio, who became an inseparable companion and is always available for the most interesting discussions; Fabio Calzavara, Niccolò Gallino, Simone Severo, Mattia De Stasio, and Martina Casciello, who joined the group over the years, making it increasingly special and adding sympathy and fun.

I also want to sincerely thank the other members of the group who, despite not working directly on the same topics, enriched this period with their experience

and support: Dr. Michela Fracasso, Professor Gianluca Ghigo, Professor Laura Gozzelino, and Professor Roberto Gerbaldo.

I would also like to acknowledge Professor Flyura Djurabekova and Professor Kai Nordlund, who hosted me at the University of Helsinki for more than one year.

Finally, a special thanks to my partner, Chloé, whom I met during this adventure and who made it even more special, and to my family, who have always supported my choices and tolerated the oddities that naturally come with developing a passion for science.

This work was partially supported by the National Recovery and Resilience Plan funded by the European Union-NextGenerationEU and by ENI s.p.a.

Abstract

Compact high-field fusion reactors based on high-temperature superconducting (HTS) magnets offer a promising route toward accelerated fusion development; however, their reduced size entails harsher radiation environments for the magnetic system, characterised by increased power deposition and neutron-induced lattice damage. Given the delicate nature of superconductivity, these effects represent a major risk and a potential bottleneck for the deployment of compact fusion reactors. Radiation damage in superconducting materials therefore becomes a critical design issue, requiring dedicated and carefully optimised neutronic analyses.

In this work, a Monte Carlo–centred multiscale framework is developed for the design and lifetime assessment of HTS magnet systems in compact fusion reactors. The conceptual design of ARC is adopted as a reference case, and neutron transport simulations are performed to characterise the radiation environment of the magnets and to evaluate candidate neutron-shielding materials. The assumptions underlying the neutronic calculations, in terms of transport code, nuclear data libraries, and physical models, are first benchmarked against independent calculations and then applied across different levels of geometric complexity, from a representative superconducting cable to the full reactor model. The radiation environment on the coils is subsequently compared with that expected in two additional reactor concepts with different size and design philosophy, namely VNS and DEMO.

Current reactor neutronic analyses primarily rely on dose-based metrics such as the displacement-per-atom (dpa) to quantify radiation damage, which provide an integral measure of damage but do not capture the sensitivity of complex oxides, such as YBCO, to the morphology and spatial distribution of irradiation-induced defects. Experimental evidence shows that identical dpa levels obtained under different irradiation conditions can lead to markedly different degradation behaviours, indicating the need for an enhanced description of radiation damage.

To address this limitation, a supplementary modelling layer is introduced to parametrise the defect characteristics associated with individual recoil events. This information, obtained from atomistic simulations of collision cascades, is condensed into physically motivated damage descriptors that can be directly integrated into Monte Carlo post-processing, extending standard dose metrics without altering the transport calculations themselves.

The capability of these descriptors to capture substantially different defect landscapes is first demonstrated by modelling well-controlled electron and fission-neutron irradiation experiments on YBCO single crystals. The enhanced Monte Carlo analysis is then applied to the assessment of neutron-shielding configurations for the inboard segments of the toroidal-field coils of ARC, enabling a comparative evaluation of candidate shielding materials and the estimation of magnet degradation times under fusion-relevant irradiation, relative to reference fission-neutron exposure.

Overall, this work provides a detailed and comparative analysis of the radiation environment expected in compact high-field tokamaks. In addition, it introduces a practical and physically informed extension of Monte Carlo radiation damage modelling, enabling improved interpretation of irradiation experiments and supporting the design of shielding architectures and lifetime assessment strategies for HTS magnet systems in fusion reactors.

Contents

List of Figures

List of Tables

Chapter 1

Introduction

1.1 Thermonuclear fusion and magnetic confinement

Over the past century, global energy demand has risen steadily (15), while growing awareness of climate change has rendered fossil-fuel technologies increasingly untenable. In response, renewable energy sources have gained significant traction and are now an integral part of the energy mix in most developed countries. Yet, despite rapid progress, renewables alone remain insufficient to achieve full decarbonization (16).

At the same time, the shifting geopolitical landscape has exposed the strategic vulnerability of energy-importing nations, renewing interest in domestic, low-carbon power generation. Within this context, nuclear energy has re-entered the political and scientific debate. Conventional fission reactors have demonstrated for more than six decades their ability to deliver large-scale, carbon-free baseload electricity (17). However, persistent concerns among the public opinion over reactor safety, long-lived radioactive waste, proliferation risks, and the use of rare or geopolitically sensitive materials continue to limit their societal acceptance across much of Europe (18).

In this frame, nuclear fusion has recently re-captured both public imagination and scientific attention, emerging as a promising long-term solution to the energy challenge. First conceived in the theoretical studies of stellar cores during the 1920s

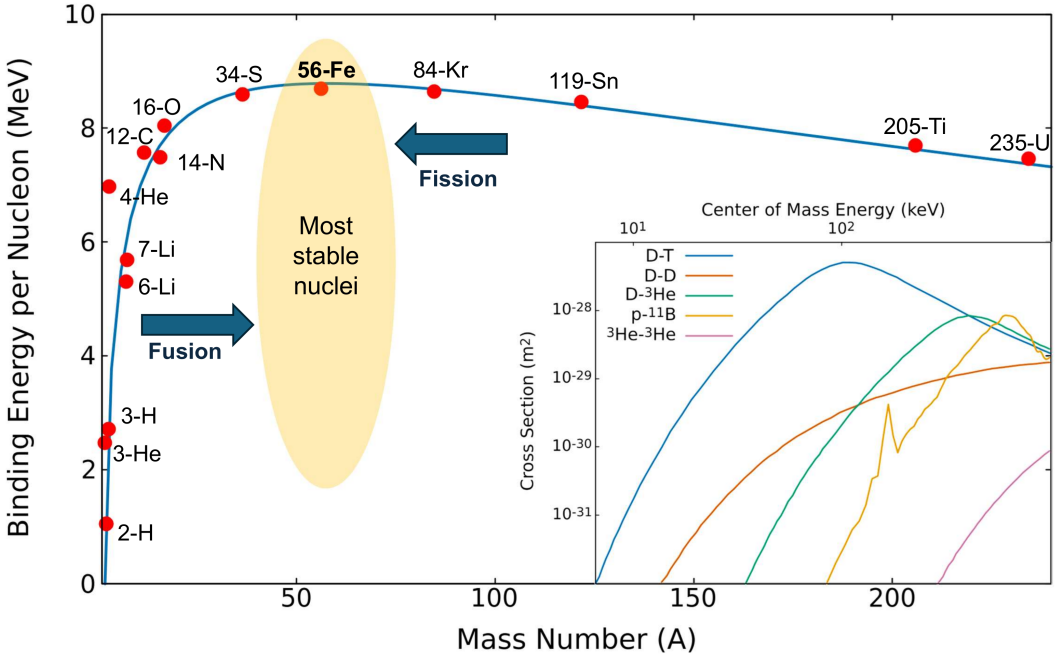

Fig. 1.1 Binding energy per nucleon as a function of mass number. The blue curve shows the binding energy per nucleon as computed using the semi-empirical Bethe–Weizsäcker mass formula, while the red points indicate values for selected isotopes. The region around 56-Fe corresponds to the most strongly bound nuclei. Nuclear processes that move systems toward this maximum release energy: heavy nuclei do so via fission, while light nuclei do so via fusion. Inset: Fusion cross sections for the main candidate reactions for thermonuclear applications, extracted from ENDF/B-VIII.0 evaluations. Among these, the D–T reaction exhibits the highest cross section at the lowest center-of-mass energies.

and 1930s (19, 20), fusion research has since evolved from astrophysical curiosity to a major technological endeavour.

Beyond the idea of reproducing on Earth the same process that powers the Sun, fusion offers several compelling advantages. It can achieve extremely high power densities, uncomparable with other renewable sources, relies on virtually inexhaustible fuels, and produces no greenhouse-gas emissions during operation. Its predicted overall carbon footprint, even on a full life-cycle basis, is among the lowest of any energy technology (21). Most importantly, fusion is inherently safe: the absence of chain reactions, since the reactants differ from the products, prevents any runaway in the event of a loss of control. Also the generation of long-lived radioactive waste can be drastically reduced, by careful selection of low-activation structural materials (22).

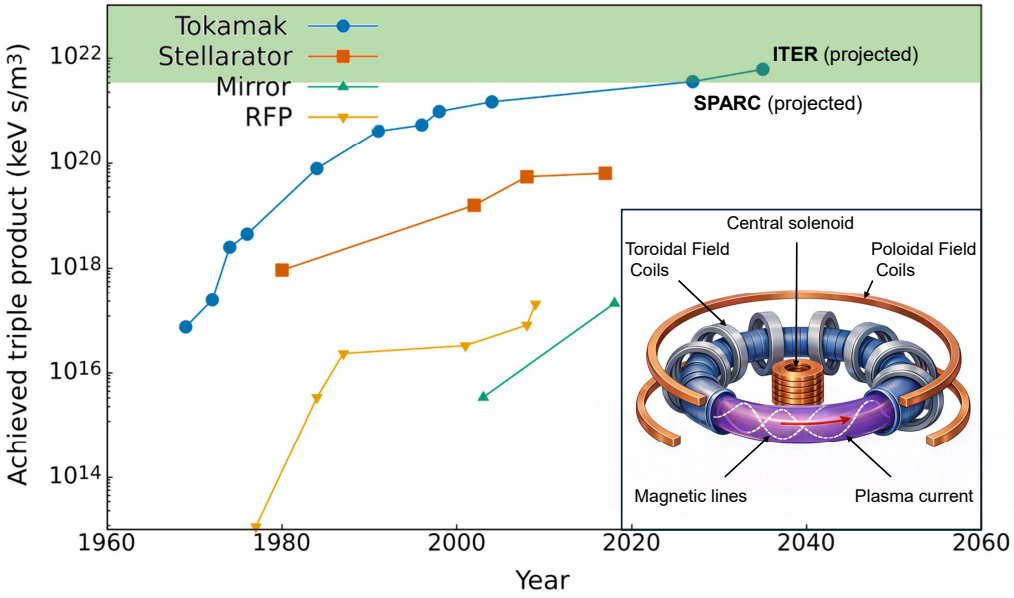

Fig. 1.2 Achieved triple product in different magnetic-confinement fusion concepts as a function of time. The green band marks the approximate triple-product threshold required for energy-producing fusion conditions. Tokamak experiments have steadily increased their performance over the decades and have consistently outperformed other magnetic-confinement configurations such as stellarators, mirror machines, and reversed-field pinches. Data from (1). Inset: Schematic illustration of the tokamak magnetic configuration, showing the combined toroidal and poloidal fields that generate the characteristic helical field lines confining the plasma.

As in fission, the energy released by nuclear fusion arises from the fact that the most energetically favorable nuclear configurations correspond to nuclides with the highest binding energy per nucleon, those around 56-Fe and 62-Ni (Fig. 1.1). Consequently, any nuclear transformation that moves toward this region of maximal stability in the nuclear chart can release energy, even though an activation energy is required to overcome potential barriers. For heavy nuclei such as uranium, greater stability is achieved by splitting the nucleus into lighter fragments (the process known as fission) which liberates the excess binding energy. Conversely, light nuclei can reach the same stable region from the opposite side of the curve, by fusing into heavier nuclei and converting part of their mass into energy according to Einstein's relation. Because nuclei are positively charged, they experience a strong Coulomb

repulsion, and fusion can occur only when the reacting particles approach closely enough for the strong nuclear force to overcome this electrostatic barrier. For this reason, the lightest nuclei are generally preferable as reactants because their lower electric charge reduces the Coulomb repulsion, making fusion more attainable under practical conditions. Among the various possible reactions, those involving hydrogen isotopes (²H, ³H, and ³He) or other light elements such as 11-B are the most relevant for energy production. The deuterium–tritium (D–T) reaction is by far the most favorable under accessible conditions, combining a large fusion cross section with comparatively moderate temperature requirements (Fig. 1.2, inset). Its products (an alpha particle and a 14.1 MeV neutron) carry a total energy release of 17.6 MeV per fusion event:

$$^{2}\mathrm{H} + {}^{3}\mathrm{H} \rightarrow {}^{4}\mathrm{He}\ (3.5\ \mathrm{MeV}) + n\ (14.1\ \mathrm{MeV}).$$

While fusion neutrons carry approximately two thirds of the released energy and are ultimately responsible for power extraction in a reactor, the role of the fusion-born alpha particles is equally fundamental in the overall energy balance of the system. In a D-T plasma heated toward thermonuclear conditions, the power deposited by fusion-born alpha particles indeed provides an increasing fraction of the total heating. When adequate confinement is achieved, a limiting situation can be reached in which alpha-particle heating alone is sufficient to balance the energy losses of the plasma. This self-sustaining regime, in which external heating can in principle be removed, is referred to as ignition (23).

The ignition condition can be conveniently expressed in terms of the triple product $nT\tau_E$, where n is the plasma particle density, T the ion temperature, and τ_E the energy confinement time. This quantity combines the requirements on plasma density, temperature, and energy confinement time. For D-T plasmas in the temperature range of approximately 10-20 keV, the corresponding threshold is commonly written as

$$nT\tau_E \gtrsim 3 \times 10^{21}\ \mathrm{m^{-3}\,keV\,s}. \tag{1.1}$$

A more general measure of fusion performance is provided by the energy gain factor Q, defined as the ratio between the fusion power produced and the externally supplied heating power,

$$Q = \frac{P_{\mathrm{fus}}}{P_{\mathrm{ext}}}. \tag{1.2}$$

While ignition corresponds to the limiting case $Q \to \infty$, large values of Q can be achieved without full ignition. In practical reactor concepts, external heating is therefore expected to play an important role for plasma control and stability, even when operating close to ignition conditions.

Sustaining fusion reactions in a controlled manner requires maintaining the reacting nuclei in conditions where the probability of interaction is sufficiently high. This demands extremely energetic particles and a physical state that allows them to move freely and collide with one another, conditions that are achieved in the plasma phase of matter, where reactants are at least partially ionized and exhibit collective behavior (24). To achieve these conditions, a fusion device must be able to bring the fuel to the required temperature and density and, crucially, to prevent their rapid loss, so that the plasma remains in a fusion-relevant regime for a sufficiently long time. This is the objective of confinement systems, whose role is to restrain the plasma expansion and maintain the thermodynamic parameters needed for fusion reactions. While this confining energy is naturally provided by the gravitational field in stars, producing and maintaining a plasma in a controlled regime on earth is a major scientific and engineering challenge, and several strategies have been developed to meet it. Among them, inertial and magnetic confinement represent the two principal approaches explored in fusion research (24–26).

Inertial confinement relies on the rapid implosion of small fuel capsules to reach the extreme densities and temperatures required for fusion. In the most common laser-driven schemes, a precisely shaped energy pulse ablates the outer layer of a spherical pellet, generating an inward-directed shock that compresses the fuel and heats it to several keV. The entire process unfolds on nanosecond time scales, with the fuel remaining in fusion-relevant conditions only for a very short interval, confined solely by its own inertia (27). The extremely short confinement time is compensated by the very high densities achieved during the implosion; however, the process is inherently impulsive and cannot sustain a plasma beyond a single burst.

Recent inertial-confinement experiments have demonstrated ignition in individual implosions (28), providing a remarkable validation of the extreme physical conditions achievable in laser-driven compression. Nevertheless, this achievement remains intrinsically limited to isolated, short-lived events. Conceptual reactor schemes would require operation at repetition rates of several hertz, together with precise synchronization of targets, drivers, and optics, a level of technological integration that

is well beyond current capabilities. In addition, the limited efficiency of present high-power laser systems represents a major obstacle to translating single-shot ignition into net electrical power production (29).

On the other hand, magnetic confinement seeks to maintain the plasma in fusion-relevant conditions by using strong magnetic fields to limit its expansion and isolate it from material walls. By exploiting the charged nature of the plasma constituents, magnetic fields can constrain particle motion through the Lorentz force $\mathbf{F} = q\,\mathbf{v} \times \mathbf{B}$, causing ions and electrons with a velocity component perpendicular to the field to gyrate around magnetic field lines.

In the idealized case of a straight and uniform magnetic field $\mathbf{B}$, charged particles follow helical trajectories composed of a circular motion in the plane perpendicular to the field while the center of the circle (the guiding centre) proceeds along the field direction. This gyration is characterized by the cyclotron (angular) frequency

$$\omega_c = \frac{|q|B}{m},$$

where q and m denote the particle charge and mass, respectively, and $B = |\mathbf{B}|$ is the magnetic-field magnitude. The associated radius of the circular motion, known as the Larmor radius, is given by

$$\rho_L = \frac{v_\perp}{\omega_c} = \frac{m v_\perp}{|q|B},$$

with $v_\perp$ indicating the component of the particle velocity perpendicular to the magnetic field.

Owing to their much smaller mass, electrons gyrate around magnetic field lines at significantly higher frequencies than ions, with correspondingly smaller Larmor radii; their negative charge also implies an opposite sense of rotation (30). In magnetic confinement devices, the Larmor radii of both ions and electrons remain much smaller than the characteristic dimensions of the system, typically of the order of millimeters, for effective plasma confinement (31).

While a straight and uniform magnetic field can provide radial confinement of a plasma, it does not prevent particle losses along the field direction. In the absence of axial confinement, particles can freely stream along magnetic field lines, rendering such a configuration unsuitable for practical fusion applications.

One attempt to overcome this limitation while preserving a relatively simple magnetic geometry was proposed at the very beginning of fusion research with the introduction of the so-called magnetic mirror configuration (30, 32, 33). In this approach, the magnetic field strength is increased at the ends of the system by means of additional coils. As a result, particles with sufficiently large perpendicular velocity components can be reflected, forming an open-ended magnetic trap.

This reflection mechanism arises from the fact that the kinetic energy of a charged particle can be decomposed into a component associated with motion parallel to the magnetic field and one associated with the gyration motion,

$$E = \frac{1}{2}mv_{\parallel}^2 + \frac{1}{2}mv_{\perp}^2$$

Assuming that the Larmor radius is small compared with the characteristic length scale over which the magnetic field varies ($\rho_L \ll L_B$, with $L_B = B/|\nabla B|$, the so-called adiabatic regime), the magnetic moment

$$\mu = \frac{mv_{\perp}^2}{2B}$$

is constant. As the particle moves toward regions of increasing magnetic field strength, conservation of μ requires an increase in the perpendicular kinetic energy. Since the static magnetic field performs no work on the particle, total energy conservation implies a corresponding decrease of the parallel kinetic energy. When the parallel component of the particle velocity is reduced to zero, the effective force associated with the magnetic-field gradient continues to act, causing the parallel velocity to reverse sign, so that the guiding center turns back along the magnetic field line. Particles are therefore reflected if this reversal occurs before reaching the point of maximum field present in the system (34).

Despite its conceptual simplicity, mirror confinement suffers from intrinsic limitations. Only a fraction of the particle population can be reflected, leading to continuous particle and energy losses along the field lines. These losses distort the velocity distribution away from a Maxwellian equilibrium and, together with collisional scattering that progressively transfers particles from the reflected population into velocity-space regions for which reflection is no longer possible, result in poor energy confinement and the onset of plasma instabilities.

Classical magnetic mirror confinement systems were abandoned in the 1980s as candidates for operational fusion reactors (31), but the research in the field has continued, with advanced mirror configurations demonstrating improved confinement regimes and promising performance as a neutron source for fusion materials testing (35).

A natural approach to address the issue of axial confinement is to bend the magnetic field lines, moving from a cylindrical geometry to a toroidal one. In this way, magnetic field lines are closed on themselves, eliminating open ends and the associated axial losses. From a conceptual point of view, the generation of a toroidal magnetic field is relatively straightforward, as it can be obtained by winding magnetic coils along the toroidal direction, resulting in a donut-shaped configuration.

However, the particle motion discussed above, simply characterized by gyromotion around magnetic field lines and motion along them, is valid only in the case of a straight and homogeneous magnetic field. In a toroidal geometry, the magnetic field cannot be made spatially uniform: due to the curvature of the field lines, the field strength exhibits an intrinsic radial dependence, being stronger on the inner side of the torus and weaker on the outer side (36).

This magnetic field inhomogeneity introduces additional particle drift motions that compromise radial confinement (34). The radial variation of the magnetic field strength implies that the Larmor radius of a charged particle is not constant along its orbit, being larger in regions of weaker magnetic field and smaller where the field is stronger. As a consequence, the gyration orbit becomes asymmetric, giving rise to a net drift perpendicular to both the magnetic field and its gradient. This so-called gradient-B drift occurs in opposite directions for ions and electrons and has a magnitude proportional to the ratio ρ_L/L_B and to the perpendicular particle velocity.

In addition, the curvature of magnetic field lines in a toroidal geometry introduces a further charge dependent drift component. Particles moving along curved field lines experience an effective centrifugal force associated with their parallel motion, resulting in the so-called curvature drift. In a purely toroidal magnetic field, the gradient-B and curvature drifts are directed in the same direction and therefore add up.

As a result, bending a magnetic field into a toroidal shape does not by itself provide radial confinement. It was soon realized, however, that magnetic fields could

be generated in such a way as to guide charged particles along trajectories capable of compensating these drift motions. This can be achieved if particle orbits do not lie on purely toroidal paths, but instead follow helically twisted magnetic field lines, allowing drift effects to average out over the trajectory. Already in the late 1950s, the first magnetic confinement device explicitly based on this principle was proposed by Spitzer et al. (37, 38) and named "stellarator".

In this reactor design, plasma confinement is achieved by generating a magnetic field with an intrinsically three-dimensional structure, providing the required rotational transform of the field lines. Such a transform can be obtained either by introducing a non-planar magnetic axis or by shaping the magnetic flux surfaces so that they are elongated and rotate poloidally as they wind around the torus. The resulting magnetic configuration is fully non-axisymmetric and is produced by external coil systems operating in steady state outside the plasma chamber (39).

While this approach appears, in principle, well suited to overcome the limitations of purely toroidal magnetic fields, the early realization of stellarator concepts proved to be technically challenging. Initial attempts to construct the required complex coil systems suffered from insufficient engineering accuracy and limited manufacturing capabilities, leading to significant magnetic field errors and degraded confinement properties (40). As a consequence, the performance of early stellarator experiments, such as the Model-C device, fell well below expectations (39).

Beyond these technological difficulties, stellarators also exhibit intrinsic design challenges. The three-dimensional nature of the confining magnetic field precludes axisymmetry, resulting in comparatively large machine dimensions and a substantial spatial separation between plasma and coils. Moreover, while some operational flexibility can be achieved by adjusting the currents in the external coils, the magnetic configuration is largely fixed once the device is constructed, limiting the range of plasma scenarios that can be explored within a given design. In addition, early experiments revealed that particle losses tended to increase with temperature, an effect attributed to the direct loss of particles trapped in local magnetic field minima inherent to complex three-dimensional configurations (39).

Although continued advances in coil engineering and experimental operation led to improved confinement in later stellarators, such as Heliotron-E (41) and W7-A (42), the combination of the lack of axisymmetry, the technological challenges associated with coil design, and the absence of a clear consensus on an optimal three-

dimensional magnetic configuration limited the pace of progress, contributing to an early shift the fusion community's attention toward a closely related confinement concept, the TOroidalnaya KAmera i MAgnitnye Katushki, Tokamak.

Developed in the early 1950s at the Kurchatov Institute by Sakharov and Tamm (43), the tokamak confinement concept was not openly published at the time owing to the classified nature of fusion research. Only partial elements, mainly related to high-current toroidal discharges, appeared in Soviet contributions to the Second United Nations Conference on the Peaceful Uses of Atomic Energy held in Geneva in 1958 (44).

Like stellarators, tokamaks rely on a twisted magnetic field topology to form closed magnetic flux surfaces. However, in contrast to stellarators, the required field-line twist is not generated solely by external non-coplanar coils. Instead, it arises from a toroidal plasma current, which produces a poloidal magnetic field component that twists the overall magnetic field configuration. In this sense, the plasma itself plays an active role in shaping the confining magnetic geometry (23).

The plasma current, which constitutes the defining feature of tokamaks, was originally generated inductively by means of a transient magnetic field produced by a central solenoid. Due to its inductive nature, such a current drive scheme inherently leads to pulsed operation, which is incompatible with the requirements of steady-state power production in reactor-grade devices. For this reason, alternative solutions have been developed to sustain the plasma current non-inductively, including external current drive mechanisms based on radio-frequency waves and neutral beam injection, complemented by the self-generated bootstrap current arising from pressure gradients within the plasma. Additional magnetic coil systems are employed to control plasma position and to provide stabilization against macroscopic instabilities (23).

The relative simplicity and robustness of this axisymmetric configuration enabled decisive experimental progress already in the late 1960s. In particular, the results obtained on the T-3 tokamak at the Kurchatov Institute, and their subsequent independent verification, marked a turning point in fusion research. From that point onward, tokamaks have consistently achieved the highest performance among magnetic-confinement concepts, showing a steady increase in attainable values of the triple product over several decades and establishing themselves as the most mature platform for fusion power (Fig. 1.2).

1.2 From large-scale tokamaks to compact high-field concepts

The proliferation of tokamaks around the world began shortly after the breakthrough results obtained on the T-3 device, triggering an intense international effort to design new tokamaks oriented toward reactor-relevant conditions. As early as 1968, the (at that time) recently built Princeton C-stellarator was converted into a tokamak (45), while in the Soviet Union the T-series continued to evolve (43). A first generation of tokamaks was rapidly constructed outside the USSR, including TFR in France (46), ORMAK in the United States and Pulsator in Germany successfully reproducing and extending the performance achieved on T-3 (47).

Already from early experiments, empirical scaling laws emerged indicating that the energy-confinement time increases with the characteristic dimensions of the device. This observation, together with the greater operational margins offered by larger machines, motivated a progressive increase in tokamak size. As an illustration of this trend, the plasma volume of the early Soviet T-1 device was of the order of 0.4 m^3, whereas the Joint European Torus JET, designed in 1971, features a plasma volume close to 100 m^3 (48, 49).

The subsequent generation of large tokamaks, exemplified by JET in Europe and JT-60 in Japan, began operation in the early 1980s and achieved several milestone results on the path toward fusion energy production. In particular, JET became the first tokamak to operate with a deuterium–tritium plasma, producing about 1 MW of fusion power in a discharge lasting approximately 2 s (50). Further high-performance results were obtained on TFTR and JT-60U (31), with a new milestone again reached by JET in 1997, when 16 MW of fusion power were produced for about 1 s thanks to the new confinement H-mode discovered at ASDEX, corresponding to a fusion gain of approximately 0.65 (51). In parallel, a number of smaller tokamaks equipped with superconducting coils demonstrated steady-state or long-pulse operation on time scales of hours, highlighting the feasibility of sustained plasma operation (52).

Although none of these experiments achieved net energy production, they demonstrated for the first time the ability to reliably create, control, and sustain plasmas capable of releasing fusion power at the megawatt level, thereby providing a crucial validation of the tokamak approach for reactor-scale applications. The natural next step was therefore to design a new, larger experiment, with dimensions guided by

the scaling laws derived from decades of tokamak operation and with the explicit objective of producing fusion power far exceeding the externally supplied heating power.

In the mid-1980s, this scientific trajectory converged with a major political initiative, when the United States and the Soviet Union agreed to pursue the widest possible international cooperation in fusion research, later joined by Europe and Japan, with the shared goal of developing a large experimental fusion facility (49).

This effort evolved into the International Thermonuclear Experimental Reactor ITER, a fully international project based on an intergovernmental agreement. Following conceptual and engineering design phases carried out between the late 1980s and early 2000s under the auspices of the IAEA, a complete and integrated design for ITER was finalized, providing the technical basis for construction. ITER is presently under construction at Cadarache, France, as the flagship experiment aimed at demonstrating a burning plasma regime and dominant alpha-particle self-heating in a tokamak (49).

The design of ITER represents an unprecedented step in the scale and integration of fusion engineering, combining a very large magnetized plasma volume with high magnetic fields, advanced superconducting magnet technology requiring extremely large cryogenic systems, multiple high-power auxiliary heating systems, highly sophisticated plasma control and protection schemes. The necessity for ITER to operate routinely with tritium further requires fully remote maintenance capabilities and the implementation of a dedicated nuclear safety framework (31).

These demanding requirements have acted as a powerful driver for technological development: many of the resulting solutions can already be adopted in other fusion experiments, including privately funded devices, while the associated growth in engineering capability and personnel expertise is expected to generate broader benefits beyond ITER itself.

From the physics perspective, ITER is designed to access regimes well beyond those explored in present-day experiments. In addition to demonstrating a burning plasma, ITER must address a set of critical challenges, including the management of extreme heat and particle exhaust, the control of edge-localized modes, and the prevention or mitigation of major plasma disruptions (53).

Despite its fundamental role as a physics and technology integrator, ITER was never conceived as a power-producing reactor. The excess fusion power generated in the device will not be converted into electricity, but dissipated, and ITER will not be equipped with one of the key technologies required for a reactor: a breeding blanket capable of using fusion neutrons to produce tritium in situ while simultaneously capturing and converting their energy (53).

For this reason, almost at the same time as the ITER agreement, the fusion community was already considering the subsequent step (54). While the construction of ITER was progressing, the concept of a European demonstration fusion power plant, DEMO, was proposed as the device intended to bridge the gap between ITER and a commercial reactor (55).

Conceived to produce net electrical energy, DEMO requires more demanding plasma parameters than ITER. Following the same scaling laws adopted for its predecessor, it is therefore designed to be even larger, with present concepts describing major radii in the range 7–9 m, compared with ITER's 6.2 m (31). Different blanket concepts are under investigation, including helium-cooled pebble-bed (56), water-cooled lithium-lead (57), and water-cooled ceramic breeder designs (58), aimed at simultaneously fulfilling three functions: conversion of neutron energy into heat, breeding of tritium, and shielding of sensitive components such as the superconducting magnets.

The magnetic system of DEMO relies on conventional low-temperature superconducting toroidal-field coils capable of producing magnetic field on-coil of the order of 13 T (59), together with a superconducting central solenoid and poloidal-field coils, employing technologies closely related to those developed for ITER. Superconducting magnets are in this case mandatory, as the resistive losses associated with copper coils would be incompatible with long-duration operation, and the use of resistive magnets represented a fundamental limitation for earlier devices such as JET (60). As in ITER, these coils are located at substantial distance from the plasma, thanks to the large size of the machine, and are protected by thick layers of in-vessel components and shielding structures (55). It is therefore reasonable to expect that the most severe radiation damage will primarily affect the plasma-facing components and the blanket.

The design philosophy underlying DEMO reflects a continuation of the conservative approach adopted for ITER, trying to take as most advantages as possible from

that experience (61). To mitigate technical risk, DEMO concepts generally favor large machine dimensions, well-established technologies (such as low-temperature superconductors), and substantial shielding thicknesses. Within the European fusion strategy, this conservative pathway is regarded as essential to ensure a credible transition from experimental demonstration to first-of-a-kind power plants.

However, the same design choices that enhance robustness also introduce significant challenges. The scale of ITER- and DEMO-class devices entails long construction times, complex supply chains, and very high capital costs. ITER is already several years behind its originally announced operational schedule (62), and the extended timelines associated with large fusion facilities can slow the feedback loop between design, construction, operation, and technological improvement, potentially limiting the pace at which fusion energy can be deployed more broadly.

Interestingly, the scaling of tokamak confinement performance with machine size is not the only route that has been identified to improve fusion performance, but rather the most straightforward one to pursue with the technologies available prior to the early 2000s. It is in fact also possible to increase the tokamak triple product by increasing the strength of the confining magnetic field. Since the fusion energy gain depends nonlinearly on both magnetic field and machine size, higher magnetic fields allow the same gain to be achieved in a more compact device, without invoking new physics assumptions (63).

This idea was already recognized early in the history of fusion research, as exemplified by the pioneering high-field, compact tokamaks of the Alcator series (64). However, these early concepts relied on resistive copper magnets, which are inherently unsuitable for reactor-scale applications because of the enormous resistive losses and associated heating. As a consequence, while the high-field path was physically attractive, it could not be realistically extended to high-gain or steady-state devices.

At the time ITER was designed, low-temperature superconductors represented the most advanced and mature magnet technology available for large-scale tokamaks, with practical limits corresponding to on-axis magnetic fields of roughly 5–6 T. Within these technological constraints, ITER can therefore be regarded as the smallest device capable of achieving its targeted performance.

This situation has changed significantly with the discovery and commercial availability of high-temperature superconductors (HTS), among which Rare-Earth

Barium Copper Oxides (REBCO) tapes stand out for their exceptionally high current density, enabling substantially higher magnetic fields in superconducting magnets and reopening the design space for high-field, compact tokamak configurations (63). Different design lines are pursuing this path, such as the Spherical Tokamak for Energy Production (STEP) developed in the United Kingdom (65), but the joint design effort of Commonwealth Fusion Systems and the Massachusetts Institute of Technology Plasma Science and Fusion Center, SPARC, is explicitly conceived as the first compact tokamak aimed at demonstrating net energy gain from fusion reactions. With a major radius of 1.85 m, a toroidal magnetic field on axis of 12.2 T, and a minor radius of 0.57 m, SPARC is projected to reach an energy gain of about 2 within approximately 2% of the plasma volume of ITER (66).

Should this demonstrator confirm the feasibility of achieving net energy gain in substantially smaller devices, with reduced construction times and costs, the natural next step would be the realization of a first power plant based on HTS technology, embodied in the ARC reactor concept (14).

Conceived as a compact, high-field tokamak, ARC is intended to simultaneously serve as a pilot fusion power plant and as a fusion nuclear science facility for integrated testing of materials and components under a deuterium–tritium neutron environment. The design targets a fusion power of approximately 525 MW and an energy gain of about three, while maintaining a major radius of roughly 3.3 m. Such a compact size is made possible by operating at an on-axis toroidal magnetic field of about 9.2 T, enabled by the adoption of high-temperature superconducting magnets.

A defining architectural feature of ARC is the proposed use of demountable toroidal-field coils (TFCs). Each TF coil should be segmented, allowing the magnetic structure to be opened and providing direct access to the vacuum vessel. This approach would enable a modular maintenance strategy in which the entire vacuum vessel, together with all in-vessel components, could be fabricated, assembled and tested externally before installation. In operation, the vessel module could be inserted once the TF coils are opened, thereby minimizing maintenance activities within the magnet volume and simplifying component replacement (14).

The vacuum vessel is foreseen to be manufactured from Inconel-718, selected for its mechanical strength and corrosion resistance at high temperature. Although its high nickel content leads to relatively high activation under neutron irradiation, this alloy represents a practical first-choice structural material for an initial reactor design.

The vessel has an approximately elliptical toroidal geometry and a double-wall structure, incorporating internal channels for coolant flow.

The demountable-coil configuration would also allow the adoption of an unconventional blanket concept based entirely on liquid FLiBe. In this scheme, the molten salt simultaneously functions as coolant, tritium breeder, neutron moderator and shielding material. The FLiBe would be contained in a large, low-pressure vessel known as the blanket tank, which would surround the vacuum vessel and act as the primary nuclear confinement boundary. As neutrons from fusion reactions would be absorbed in the FLiBe, their energy would be deposited as heat and tritium is produced; the bred tritium would subsequently be extracted from the circulating liquid outside the blanket tank (14).

The combination of high fusion power density and reduced machine size suggests that the radiation environment experienced by the superconducting magnets in compact reactors will be particularly severe when compared with that foreseen for conventional, large tokamaks, as indicated by previous studies (67). A detailed characterization of the radiation environment in the magnetic system therefore becomes a fundamental issue for the development of this class of reactors, especially considering that no existing experimental facility can directly reproduce the conditions experienced by superconducting coils in a fusion reactor (68).

Under these circumstances, computational neutronics analyses represent the primary tool for assessing neutron transport, energy deposition and radiation damage in magnet systems. A quantitative description of these quantities is essential to support design choices, identify potential weaknesses and guide the development of targeted experimental investigations (69).

In this context, the present work adopts the ARC concept as a reference high-field compact reactor, owing to its detailed public documentation and to the particularly demanding conditions it imposes on the magnet system. The radiation environment predicted for ARC magnets is evaluated using Monte Carlo techniques and is also compared with that expected in large reactor concepts such as DEMO, as well as with a compact volumetric neutron source (VNS) tokamak recently proposed within the EUROfusion programme as a viable test facility for materials under severe neutronic fluxes (70) (Fig. 1.3). These comparisons aim to elucidate the impact of machine size and design philosophy on the radiation conditions experienced by superconducting coils.

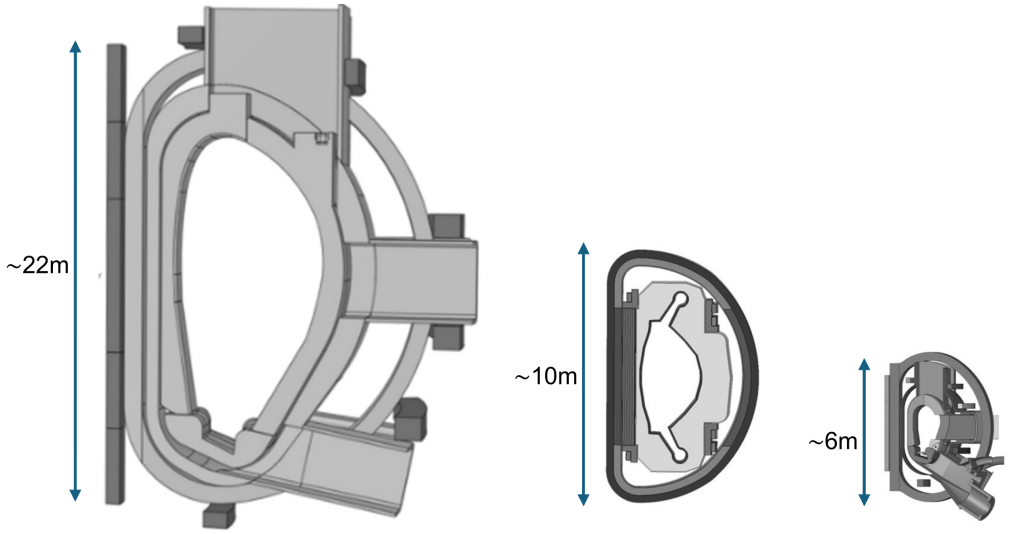

Fig. 1.3 Size comparison between european DEMO (left), ARC concept (center) and the VNS, in scale

Beyond the characterization of the radiation environment itself, a further key aspect of the present work is to translate such irradiation conditions into physically meaningful estimates of degradation in high-temperature superconducting materials. For this reason, a sound understanding of the physical properties and irradiation response of these materials is required.

1.3 High-temperature superconductors for fusion magnets: a focus on YBCO

Superconductors are materials that, below a critical temperature, can transport electrical current without significant resistive losses and sustain magnetic fields up to a critical value without energy dissipation (71). The technological potential of superconductivity was recognized almost immediately after its discovery in 1911. In a 1913 lecture, only two years after the discovery of the phenomenon, Kamerlingh Onnes suggested that the absence of electrical resistance could in principle enable the construction of extremely powerful electromagnets, far exceeding the capabilities of iron-core devices of the time (72). However, the materials then available belonged to what is now classified as type-I superconductors, which lose their superconducting

state under relatively weak magnetic fields, making them unsuitable for high-field applications.

Superconductivity therefore remained confined to laboratory and advanced physics research for several years, although the community continued to explore this appealing phenomenon from both theoretical and practical perspectives. By the middle of the twentieth century, the first tangible outcomes of these efforts emerged, with the identification, among type-II superconductors, of alloys capable of preserving superconductivity under significantly higher magnetic fields, compatible with technological applications (73).

In the same period, fundamental theoretical advances were also achieved, in particular the explanation of type-II superconductor behaviour by Abrikosov in 1957 (74), and, in the same year, the microscopic theory of superconductivity developed by Bardeen, Cooper and Schrieffer (75), laying the foundation for practical high-field applications.

Superconductivity was identified in Nb_3Sn in 1954 (76), followed seven years later, in 1961, by NbTi (77). These two alloys went on to dominate superconducting magnet technology for several decades (72). Like all other superconducting materials available at the time, their critical temperature lies below 20 K, and they are therefore retrospectively referred to as low-temperature superconductors (LTS).

Despite its earlier identification, Nb_3Sn was not the first material to find application. With a critical temperature of about 18 K, the A15 phase of niobium-tin is a type-II superconductor well suited for the generation of magnetic flux densities above the 10 T range; however, it is intrinsically brittle and difficult to process, and its critical temperature, critical current density, and upper critical magnetic field depend on applied stress and strain (78, 79). For these reasons, Nb_3Sn was adopted mainly for high fluxes applications, where other solutions were not suitable (73).

In contrast, NbTi possesses excellent mechanical properties and can be readily fabricated using conventional extrusion and wire-drawing techniques. Its superconducting properties depend primarily on alloy composition and are comparatively less sensitive to mechanical deformation. These features made NbTi the first choice material for a wide range of superconducting magnets (73). For practical applications, both materials are manufactured as composite multifilamentary conductors, in which the superconducting phase is subdivided into fine filaments and embedded in a

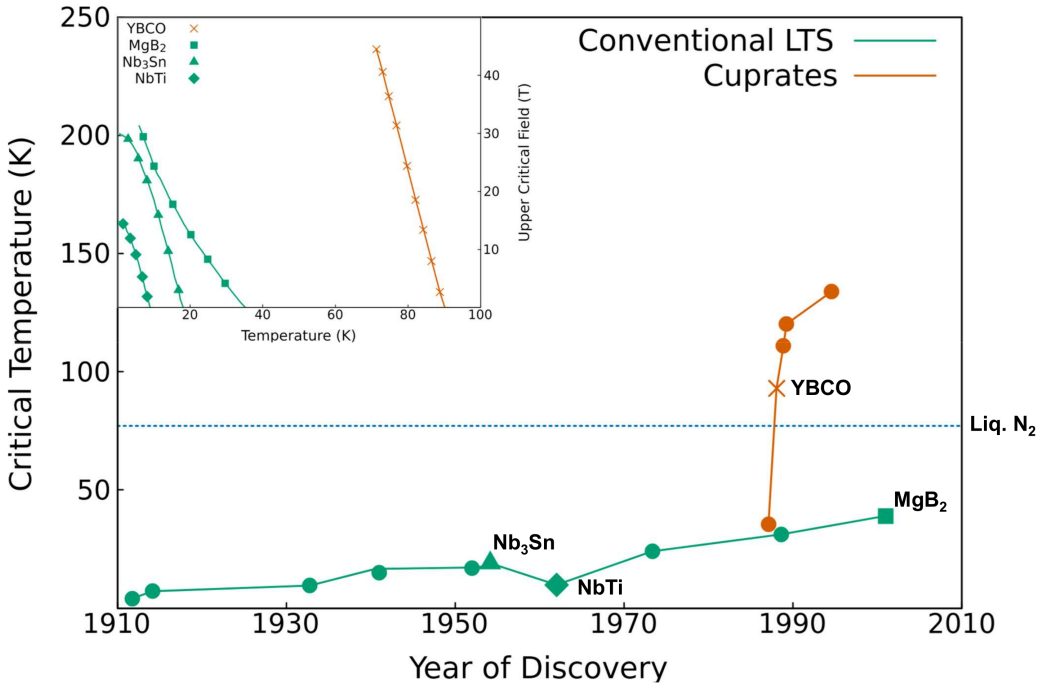

Fig. 1.4 Critical temperature of conventional LTS and cuprate superconductors as a function of their year of discovery (2). Conventional LTS compounds remain well below the boiling point of liquid nitrogen (dashed blue line), whereas cuprate superconductors exhibit critical temperatures that can exceed this threshold by a large margin. Inset: Upper critical field as a function of temperature for representative superconductors (YBCO, MgB_2,Nb_3Sn, NbTi). YBCO exceeds 30 T in upper critical field, outperforming all LTS and enabling much wider temperature operating margins (3)

low-resistivity normal-metal matrix, typically high-purity copper, providing thermal and electrical stability (Fig. 1.5A).

A major shift occurred in 1986, when Bednorz and Müller, then working in Zürich, reported evidence for a superconducting transition at a temperature of about 30 K in a Ba–La–Cu–O (80) (a compound originally synthesized at the University of Caen (81)), a result that was soon confirmed by independent experiments (82, 83).

Following this discovery, intense research activity focused on ceramic, perovskite-like cuprate compounds. Already in 1987, superconductivity was identified in Y-Ba-Cu-O compounds in the United States (84), with a critical temperature of approximately 93 K. One year later, superconductivity was reported in Bi–Sr–Ca–Cu–O compounds (BSSCO) in Japan (85), with critical temperatures approaching 105 K. With critical temperatures well above the boiling point of liquid nitrogen at 77 K

(see Fig. 1.4), these materials constituted the first representatives of what are now broadly referred to as high-temperature superconductors (HTS)

Despite the astonishing transition temperatures found in the cuprate family, translating these materials into practical conductors proved far more challenging than initially anticipated. Early efforts relied on the powder-in-tube (PIT) approach, in which a superconducting compound prepared in powder form is inserted into a ductile metallic tube, typically silver or a silver alloy for oxide superconductors, and subsequently processed by swaging, drawing, and rolling into wires or tapes. Heat treatments are then applied to promote phase formation and densification of the superconducting core. When this technique was applied to YBCO, the resulting conductors exhibited very low critical current densities in applied magnetic field, a limitation soon attributed to weak-link behaviour at grain boundaries(86, 87).

In parallel, PIT processing was explored for compounds of the BSSCO family, with early works on $Bi_2Sr_2CaCu_2O_x$ (Bi-2212) demonstrating substantially better transport properties (88). These results showed that round, multifilamentary Bi-2212 conductors could sustain large current densities and enable the generation of magnetic fields exceeding 20T at temperatures below 20K.

Building on these early successes, industrial development of Bi-2212 PIT conductors was pursued in several countries, with multiple manufacturers establishing production of wires and tapes. However, their performance improved only slowly over time. Only in 2011 porosity generated during ceramic processing was identified as a dominant factor limiting the achievable critical current density (89). In any case, Bi-2212 wires never reached wide commercial application, and industrial interest in this material progressively faded (90).

A different trajectory was followed by the other major compound of the BSSCO family, $Bi_2Sr_2Ca_2Cu_3O_x$ (Bi-2223). The first PIT-processed Bi-2223 tapes were reported shortly after its discovery (91) and, although the initial critical currents were modest, steady improvements were achieved over the following years, eventually reaching transport currents of about 200 A at 77K in self-field by the mid-2000s (92). In general, these developments established BSCCO wires as the first high-temperature superconducting conductors available on the market and they are consequently commonly referred to as first-generation (1G) HTS.

However, while BSSCO technology was advancing, significant progress was also being made on YBCO and related Rare-Earth Barium Copper Oxides (REBCO). In

attempting to overcome the weak-link limit that emerged with the first technologies, it was recognized that a high degree of biaxial texture was required, with the *c*-axis oriented perpendicular to the tape surface and misorientation angles in the *ab*-plane below a few degrees between adjacent grains (93, 94). Considerable effort was therefore devoted to developing techniques capable of producing long, biaxially textured tapes, and lengths exceeding 10 m were already demonstrated in the early 2000s (95, 96).

Two main strategies are employed to achieve the required crystallographic alignment in REBCO films (69). In the first approach, a polycrystalline metallic substrate (e.g. Hastelloy) is coated with a thin, highly textured layer, most commonly MgO, deposited by ion-beam-assisted deposition, which provides a quasi-single-crystal template for subsequent REBCO growth (97, 98). In the second approach, known as Rolling Assisted Biaxially Textured Substrates (RABiTS), the metallic substrate itself is mechanically processed to develop the desired biaxial texture (99, 100). In both cases, multiple buffer layers are introduced between the substrate and the superconducting film to serve different purposes. The REBCO layer is typically capped with a thin silver layer for protection, and an additional copper stabilizer is added when enhanced thermal and electrical stabilization is required (Fig. 1.5B). This conductor architecture, known as the coated-conductor technology, constitutes the second generation (2G) of HTS.

Although Bi-2223 tapes played a central role in the first deployment of high-temperature superconducting conductors, their technological development has progressively slowed as research and industrial efforts have shifted toward REBCO coated conductors, which offer superior mechanical robustness, larger critical current at high fields and greater long-term potential (90), making them a true enabling solution for compact tokamaks (63).

Decades after the discovery of superconductivity in cuprates, REBCO based conductors have reached a high level of technological maturity: they are commercially available in long-length formats and routinely exhibit high engineering current densities, making them suitable for advanced magnets applications (69). The first compound discovered in the class, YBCO, remained of main interested, becoming the most widely adopted choice for coated conductor due to its high critical current density, relatively favorable chemical stability, and compatibility with industrial deposition processes (90).

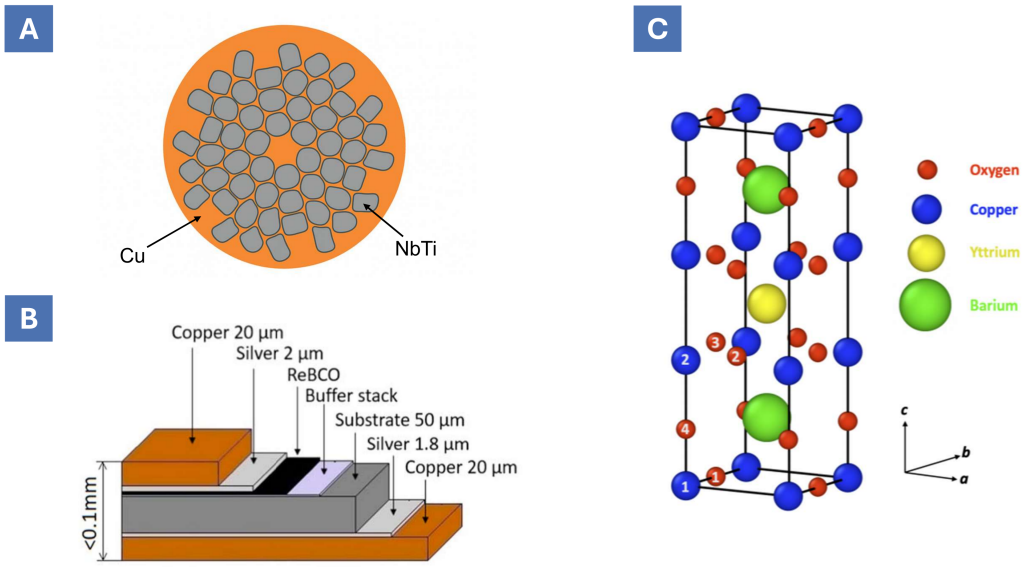

Fig. 1.5 (A) Schematic cross-section of a multifilamentary NbTi wire used for LTS cables. The NbTi filaments are embedded within a high-purity copper matrix that provides mechanical and thermal stability. (B) Schematic representation of a REBCO coated conductor tape. The layered architecture is shown, highlighting the extremely thin superconducting REBCO layer compared with the overall tape thickness. Image adapted from (4). (C) Crystal structure of YBCO. The unit cell is shown with the distinct oxygen sites (O1, O2, O3, O4) and copper sites (Cu1, Cu2) identified, together with Y and Ba positions.

YBCO crystallises in an orthorhombic, perovskite-derived structure characterised by a pronounced layering along the c-axis (Fig. 1.5C). Copper occupies two distinct crystallographic sites. The Cu(1) ions form the so-called Cu–O chains running parallel to the b-axis, located at the top and bottom of the unit cell (101). These chains act as the primary charge reservoir of the material: the degree of oxygen occupancy and ordering within them controls the hole concentration in the CuO_2 planes and is largely responsible for the orthorhombicity of the lattice (102). Variations in the chain oxygen content, parametrised by δ, therefore have a direct impact on the superconducting transition temperature (103).

The Cu(2) ions, on the other hand, are coordinated by five oxygen atoms in a square-pyramidal geometry (101). The basal oxygen atoms form the CuO_2 planes, the electronically active layers that host superconductivity. Supercurrents flow predominantly within these planes, leading to the strong anisotropy of YBCO and making their structural integrity and doping state crucial for achieving high critical current densities (104).

The Y ion occupies the central position of the unit cell and acts primarily as a structural spacer: it separates the two CuO_2 planes and helps stabilise the layered architecture of the crystal. In REBCO compounds the choice of the rare-earth element has in general only a minor influence on the superconducting properties, since the electronic states responsible for superconductivity reside almost entirely on the Cu–O network; the rare-earth ion contributes mainly to maintaining the correct lattice geometry (105, 106). Among the available rare-earth elements, Y, Gd, and Sm are the most commonly employed in coated conductors. However, Gd should generally be avoided under neutron irradiation or in the presence of significant neutron flux, as it is prone to nuclear reactions that can lead to an enhanced degradation of superconducting properties (107). In addition, mixing rare-earth elements with different ionic radii has been demonstrated to be an effective strategy for improving the in-field critical current density by introducing beneficial lattice disorder (108).

The two barium ions lie between the CuO_2 planes and the CuO-chain layer, where they help stabilise the perovskite-like framework and maintain the lattice parameters along the a and b axes through their coordination with surrounding oxygen atoms. Variations in Ba–O distances, which track the redistribution of charge between chains and planes, correlate with changes in orthorhombicity and reflect the evolving ordering of chain oxygens, that ultimately controls the doping of the CuO_2 planes (105).

The resulting crystal structure is therefore highly anisotropic and finely balanced: the superconducting properties rely on the integrity of the CuO_2 planes, on the oxygen ordering within the Cu–O chains, and on the structural support provided by the Y and Ba sublattices. It is therefore natural that the interaction between ionizing irradiation and this delicate architecture must be examined with particular care when assessing the suitability of REBCO conductors for operation in harsh environments. Of course, the effect of radiation over other, non functional parts of the tape, could have an effect.

1.4 Radiation damage mechanisms and their effects on YBCO

The history of irradiation studies in YBCO started almost immediately after the discovery of its superconducting state, with papers on neutron-induced damage effects already published in 1988, just two years after the discovery of the compound (109).

This early interest was largely motivated by the extensive experience previously gained on conventional LTS, where irradiation had been explored both to assess material reliability in radiation-harsh environments and to exploit the technologically attractive possibility of enhancing the critical current through the controlled introduction of defects, thanks to a phenomenon known as flux pinning (110).

In type-II superconductors indeed, for magnetic fields above the first critical field H_{c1} the superconducting state is not completely destroyed, as in type-I materials, but magnetic flux penetrates the superconductor in the form of quantized vortices (74, 111). Each vortex consists of circulating supercurrents that generate an axial magnetic field extending over a distance of the order of the penetration depth λ and carrying a single flux quantum Φ_0. At the vortex center there is a cylindrical region, with radius of the order of the coherence length ξ ($\xi \ll \lambda$ in high-temperature superconductors), where superconductivity is locally suppressed. Vortices can be regarded as interacting elastic objects that repel each other and, under ideal conditions, arrange into an ordered lattice representing the thermodynamic ground state of the mixed phase, i.e. the regime between H_{c1}, where flux starts to penetrate, and the upper critical field H_{c2}, where superconductivity is completely lost (71).

When an electric current flows through a superconductor, a Lorentz force acts on the vortices and tends to set them into motion. The displacement of the non-superconducting vortex cores leads to energy dissipation and thus to a finite, ohmic-like resistivity (111). Preventing vortex motion is therefore of primary technological importance, since the purpose of a superconducting wire or cable is to transport current without losses; accordingly, in type-II superconductors the critical current is commonly defined as the current at which vortices start to move.

Localized non-superconducting regions, like defects, can hinder vortex motion by providing sites where the energetic cost associated with the vortex core is lower than

in the surrounding material, effectively acting as potential wells. This phenomenon is known as vortex pinning: vortices remain pinned as long as the driving force exerted by the current does not exceed the maximum available pinning force, i.e. as long as the corresponding current density does not surpass the critical current (71, 111–113). Of course, the enhancement of the critical current depends on irradiation dose and on the pre-existing defect landscape. In general, an optimal defect density exists, beyond which further increasing the dose or the concentration of defects leads to a degradation of the superconducting transport properties and to a reduction of the critical current. Early irradiation studies on conventional superconductors already interpreted this behavior in terms of two competing effects: irradiation increases the density of pinning centers, which tends to enhance the critical current by hindering vortex motion, but simultaneously reduces the superconducting order, lowering of the critical temperature. The observed peak in the critical current thus results from the balance between these two opposing trends (114).

It was therefore natural that the interest of the superconductivity community rapidly turned to investigating irradiation effects also in high-temperature superconductors. In particular, the field gained strong momentum after the groundbreaking work by Van Dover et al. reported an increase of the critical current by up to two orders of magnitude under neutron irradiation (115). Subsequently, detailed and systematic experimental campaigns with neutron irradiation were carried out, most notably at the Atominstitut of Vienna, starting in the early 1990s and continuing to the present days (107, 116, 117).

Considering the practical difficulties inherently associated with neutron irradiation experiments (most notably the need for a nuclear reactor and the activation of both samples and experimental facilities), together with the interest in exploring the different kinds of damage that can be introduced in superconductors, research efforts progressively expanded to include a variety of other particle species. Irradiation studies were therefore carried out using electrons (7, 118), protons (6), and ions (119, 120).

The use of different particles and energies allows indeed to modify the way in which energy is transferred to the lattice. In particular, structural damage can be produced either through direct collisions with lattice nuclei (non-ionizing energy loss, or nuclear), a mechanism characteristic of fast neutrons, electrons and light ions

with energies up to a few MeV, or through electronic excitations, which dominate for heavy ions in the hundreds-of-MeV to GeV energy range (121).

In the nuclear-collision-dominated damage regime, when a projectile interacts with the lattice it transfers momentum to a lattice atom through an elastic collision, producing a primary knock-on atom (PKA). The PKA, displaced from its lattice site, may carry sufficient kinetic energy to displace further atoms, thereby initiating a sequence of collisions. This sequence constitutes a collision cascade, a highly non-equilibrium process in which atomic displacements occur on very short timescales (122). In the particular case of electrons, the small energy transferable to recoil can lead to a single or few displacements, representing the low-energy limit of the cascades regime.

The ballistic phase of the cascade develops within roughly 0.1–1 ps, during which atoms are displaced mainly by direct collisions. It is followed by a short thermalization stage lasting a few additional picoseconds, in which the energy deposited by the cascade is redistributed locally. At these early times, thermally activated diffusion processes do not yet play a significant role, and the resulting primary damage is determined almost entirely by the ballistic collision sequence (122).

After the ballistic stage of the collision cascade has dissipated and the system has locally equilibrated, the lattice is left with a population of defects whose nature depends primarily on the recoil energy and on the local bonding environment. Higher-energy PKAs tend to generate extended, locally amorphous regions (“large cascades”), whereas lower-energy recoils more often produce isolated Frenkel pairs or small defect clusters. These defects may subsequently evolve over much longer time scales through thermally activated processes such as migration, clustering, or partial recombination (122).

Conversely, a qualitatively different damage regime is accessed when energy deposition is dominated by electronic excitations, as in the case of swift heavy ions. In this regime, energetic heavy particles can induce highly localized electronic excitations along their trajectory, giving rise to cylindrical damaged regions whose morphology evolves from discontinuous tracks to continuous amorphous columns as the electronic stopping power increases (123).

For insulating materials such as $YBa_2Cu_3O_7$, a fully quantitative microscopic description of track formation is still lacking. Nevertheless, the process is commonly

associated with the breakdown of the insulating state caused by the extremely strong electric fields generated between the cloud of excited electrons near the ion path and the positively charged lattice left behind. This mechanism is often discussed in terms of dielectric breakdown or, in a closely related picture, a Coulomb explosion (124, 125).

Interestingly, not all defects have the same impact on superconducting properties. Their effects depend not only on their density, but also on their size, morphology, and, in the case of point defects, on their crystallographic location.

From the perspective of the critical current, defect size represents a primary parameter, and defects capable of confining extended portions of the vortex core provide significantly stronger pinning. In this respect, optimal pinning landscapes consist of non-superconducting columns aligned with the applied magnetic field and extending over large fractions of the sample thickness. To maximize the pinning force, the diameter of such columnar defects should be of the order of the coherence length (119). More generally, for non-spherical defects—including columnar and planar defects—the pinning efficiency depends on the relative orientation between vortices and defects, leading to pronounced anisotropic pinning effects (113, 126).

Point defects produced by light-ion irradiation, conversely, are generally not optimal pinning centers. When sparsely distributed, they pin only a small fraction of the vortex length, resulting in a low net pinning energy. Even in the case of a high density of point defects, where each vortex interacts simultaneously with many pins, the vortex experiences an effectively averaged potential and the resulting critical current is significantly smaller than what would be expected from a simple sum of independent strong pinning forces, as described within the collective pinning theory (119). Among small roughly spherical defects, however, the most effective pinning centers are those with dimensions comparable to, or slightly larger than, the vortex core diameter, i.e. of the order of a few coherence lengths (113).

The suppression of the critical temperature is instead primarily governed by pair-breaking scattering, which intrinsically depends on the scattering strength of each defect (127). It has been shown that point-like defects acting as strong scatterers in the CuO_2 planes are the most effective in reducing T_c; at low irradiation doses, oxygen rearrangements in the chains may regulate the carrier doping, whereas at higher doses defects increasingly involve the CuO_2 planes, leading to a much stronger suppression of superconductivity (107, 128, 129).

This pronounced sensitivity to defect morphology is especially relevant in fusion environments, where the neutron energy spectrum and the surrounding material composition can influence the character of the resulting collision cascades. Understanding and predicting the expected defect landscape is therefore essential both for the design of shielding components and for the lifetime assessment of REBCO-based fusion magnets.

1.5 Limitations of dose-based metrics and the need for atomistic modeling

Although the microscopic mechanisms of defect formation determine how YBCO responds to irradiation, assessing the damage that superconducting magnets experience in a fusion reactor, in a way that is useful for design, operation and lifetime evaluation, requires a completely different level of description. In a realistic device, the neutron spectrum, particle fluence and recoil-energy distributions vary strongly with position and depend critically on the reactor geometry, the materials inventory and the configuration of shielding components. These quantities cannot be deduced from microscopic considerations alone: they must be obtained through detailed particle-transport calculations.

In this context, Monte Carlo radiation-transport codes play a central role. Their ability to model complex three-dimensional geometries and to track the propagation and interaction of particles across heterogeneous materials makes them the standard tool for estimating neutron fluxes, energy deposition, recoil spectra and, ultimately, radiation damage throughout the magnet system. Within these frameworks, the most widely used metric to quantify atomic displacements is the Norgett–Robinson–Torrens displacement-per-atom (dpa) (13).

Originally developed for monatomic metals and calibrated on early numerical simulations, the NRT model was conceived to provide a rapid estimate of the nominal number of atomic displacements generated by a given radiation environment. In this formulation, the deposited recoil energy was translated into a predicted number of Frenkel pairs, with no attempt to describe how these defects arrange in space or how their topology depends on the details of the cascade. Already in studies on conventional LTS superconductors, attempts to correlate the integrated damage

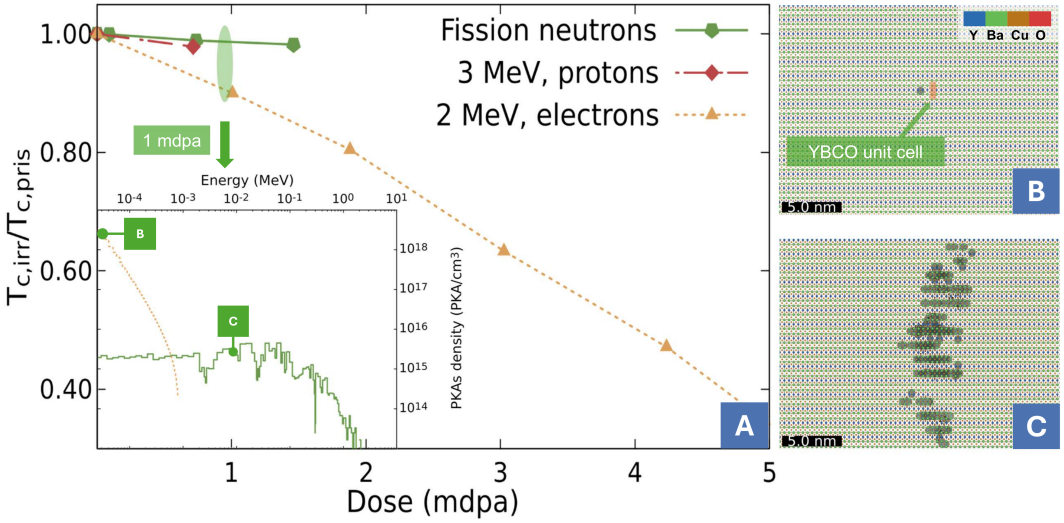

Fig. 1.6 (A) Reduction of the superconducting transition temperature T_c in YBCO single crystals under three irradiation conditions (namely fission neutrons (5), 3 MeV protons (6), and 2 MeV electrons (7)), shown as a function of the accumulated dpa. For the same dose, the resulting degradation differs substantially among irradiation types, demonstrating that dpa alone does not fully describe the impact on superconducting properties. The dpa values were reconstructed from the reported fluences and irradiation parameters. The inset displays oxygen PKA spectra corresponding to a dose of 1 mdpa. Electron irradiation produces mostly low-energy recoils (a few eV), whereas neutron irradiation generates a broad distribution extending to much higher energies. (B) Defect configuration generated by a 25 eV oxygen recoil at 20 K, obtained via molecular dynamics simulations. Interstitial atoms are shown using a translucent light-blue surface. (C) Example of a large defect cluster produced by a 7 keV oxygen recoil at 20 K in molecular dynamics simulations. Interstitials are again highlighted with a light-blue surface. Adapted from (8).

energy with the critical current were shown to fail (114), and also when extended to complex oxides, this reduction proves even more coarse: the same nominal dpa may correspond to fundamentally different defect landscapes depending on how the recoil energy is partitioned among primary knock-on atoms. Concentrating the available energy into a small number of high-energy recoils favours the formation of extended disordered regions, while distributing it among many low-energy recoils yields predominantly isolated point defects (113). Since these defect classes influence the superconducting state in markedly different ways, a dose metric that accounts for the damage energy on the lattice has limited relevance for YBCO.

Experimental observations employing different particle types (electrons (7), protons (6) and fission neutrons (5)) highlight this limitation with particular clarity.

Single-crystal irradiations performed with fully penetrating beams, and therefore free from extrinsic effects such as substrate induced strain, show that nominally identical NRT-dpa values can correspond to markedly different suppressions of T_c. Electron irradiation consistently produces the fastest degradation: even modest doses lead to a strong reduction of the critical temperature. Neutron irradiation, by contrast, yields a much milder T_c suppression at the same nominal dose (Fig. 1.5A). This divergence cannot be rationalised within the NRT framework and reflects the fundamentally different defect landscapes generated by the two irradiation types.

The origin of these differences becomes evident when comparing the corresponding PKA spectra at equal dose levels. For a representative case of 1 mdpa, electron irradiation generates almost exclusively low-energy oxygen recoils, with most events occurring below the 100 eV. Neutrons, instead, give rise to a broad and energetic recoil distribution extending up to several keV (Fig. 1.5A, inset). In other words, while electrons deposit energy through a very large number of weak individual kicks, neutrons channel it into a set of higher energetic recoils.

Although Monte Carlo transport does not provide structural information, the ensuing cascades can be simulated with other techniques, once the PKA energy is known (67) and a suitable interatomic potential is available (130). Molecular dynamics simulations show that recoils only slightly above the displacement threshold, which dominate under electron irradiation, create point-like events consisting of a few isolated Frenkel pairs confined within volumes comparable to a single YBCO unit cell (Fig. 1.5B). By contrast, keV-scale recoils typical of neutron interactions produce compact but extended collision cascades, generating tens to hundreds of defects clustered within locally disordered regions spanning several tens of unit cells (Fig. 1.5C).

For fusion applications, these limitations of the dpa is critical. Designing a magnet system based on REBCO requires a damage metric that allows one to distinguish between irradiation conditions that mainly generate extended defects, which may strengthen pinning, and those that produce a dense population of point defects, which efficiently suppress superconductivity. A scalar dose based only on the number of nominal displacements offers no guidance on which of these scenarios will prevail, and therefore provides little predictive power for assessing performance degradation or for informing shielding strategies.

In this thesis I also try to address this gap. Reactor-scale Monte Carlo simulations of compact high-field tokamaks are used to determine neutron spectra, recoil distributions and identifying hotspots and weak regions in shielding. To enable a connection between this information and the superconductor performance, an atomistic study of collision cascades in YBCO quantifies how individual recoils of different species and energies translate into stable defects, damaged volumes and clustering tendencies. By condensing this atomistic information into a transferable dataset, it becomes possible to integrate the essential physics of cascade formation directly into transport calculations, without the need to perform molecular dynamics simulations for each irradiation scenario.

The resulting approach preserves the practicality of the NRT-dpa while adding the microscopic insight needed to discriminate between defect topologies. It provides a route towards damage metrics that are both compatible with large-scale Monte Carlo tools and physically meaningful for predicting the superconducting response of REBCO in fusion environments.

Chapter 2

Methods

The multiscale nature of radiation damage in YBCO for fusion applications requires a methodological approach capable of linking the macroscopic irradiation environment of a fusion reactor to the microscopic defect structures generated by individual atomic collisions. As discussed in the introduction, no single simulation tool can capture this entire chain of phenomena: Monte Carlo transport accurately describes particle propagation in reactor-scale geometries, whereas atomistic simulations are needed to resolve the structure of collision cascades and the resulting defect populations. Binary-collision methods provide access to the high-energy ballistic phase of high energy cascades, which is inaccessible to molecular dynamics yet essential for reconstructing the damage induced by energetic neutrons.

This chapter outlines the computational framework developed to bridge these levels of description, with primary emphasis on the ARC compact high-field tokamak concept. The first section presents the Monte Carlo calculations used to determine neutron spectra, recoil-energy distributions, and displacement doses throughout the reactor environment. In addition, analogous calculations are reported for two further tokamak configurations developed within the EUROfusion program, the VNS and the DEMO reactor, in order to assess the differences in the radiation environment across different design philosophies and levels of engineering maturity.

The second section describes the MD simulations employed to characterise low and medium energy collision cascades in YBCO, quantifying defect production, clustering behaviour and characteristic damaged volumes. The third section introduces the Binary Collision Approximation (BCA) calculations used to model the

initial phase of high-energy cascades and to generate the recoil backbones for the cascades reconstruction. Finally, the combined approach is detailed, explaining how MD and BCA are integrated. Together, these methods form a consistent framework that enables the prediction of primary defect landscapes produced by collision cascades under arbitrary irradiation conditions, while maintaining compatibility with large-scale transport simulations. Because of the intrinsic timescale limitations of molecular dynamics, the framework captures the early stages of radiation damage. Nevertheless, for cryogenic irradiation conditions, where defect mobility is strongly suppressed, the predicted defect configurations are expected to provide a meaningful approximation of the as-produced damage state.

2.1 Monte Carlo calculations

Monte Carlo particle-transport codes are a primary tool for quantifying the effects of neutron irradiation in fusion devices. Their ability to model complex three-dimensional geometries, to account for detailed material compositions, to propagate particles over a broad energy range and to efficiently deal with deep shielding problems makes them indispensable for evaluating neutron fluxes, energy spectra and displacement damage in magnet systems. Unlike deterministic methods, which are generally more computationally efficient in simple shielding geometries, MC methods excel in treating arbitrary three-dimensional configurations of shielding, penetrations and diagnostic ports, and can follow secondary particles generated along the transport chain with high fidelity, provided that statistical uncertainties are kept sufficiently low. This flexibility comes at the cost of higher computational requirements, but is essential for assessing irradiation conditions in compact, high-field tokamak designs.

A wide variety of Monte Carlo transport codes exist, each optimised for specific applications ranging from cross-section evaluation to criticality studies and shielding design (131–134). In the present work, the Particle and Heavy-Ion Transport code System (PHITS) was adopted.

PHITS is a multipurpose, multiplatform Monte Carlo code developed by the Japan Atomic Energy Agency (JAEA). It models the transport and interactions of nearly all particle species (neutrons, ions, electrons, photons, positrons and hadrons) over a broad energy range, extending from 10^{-4} eV to the TeV domain (135). This

versatility has enabled its use in accelerator design, spallation studies (136), space-radiation analysis (137) and shielding optimisation (138) .

As in other general-purpose transport codes, the standard geometry description in PHITS relies on Constructive Solid Geometry (CSG), where complex structures are built by combining primitive shapes through Boolean operations. For simple or moderately structured systems this approach is effective, but when applied to reactor components with intricate spatial arrangements the CSG input can become extremely time-consuming to construct and maintain. In many cases, the number of required primitives and operations grows so rapidly that generating or modifying the geometry becomes impractical. A key advantage of PHITS for reactor-scale simulations is therefore its capability to import CAD-based geometries through tetrahedral meshes. This functionality enables an accurate representation of compact high-field tokamaks and, crucially, allows rapid redesigns without the burden of handling the increasingly complex CSG definitions that would otherwise be required.

The code supports MPI, OpenMP and hybrid parallelisation, enabling large simulations with high statistical fidelity. The native nuclear-data library distributed with PHITS is JENDL-4.0 in ACE format (139), although any library in ACE format can be employed. Moreover, for neutrons above 20 MeV different physical models are available to complement the transport.

In the present work, the MC framework was applied at progressively increasing levels of geometrical and physical complexity. First, simulations of a breeding blanket configuration were performed to validate the neutron transport model against an independent code. Second, neutron irradiation of a superconducting cable was simulated to guide a first estimate of shielding requirements and to test the coupling of MC results with finite-element calculations. Third, a complete ARC-like reactor configuration was modelled to quantify neutron irradiation under realistic operating conditions and to characterize the radiation environment expected for high-field fusion reactors. Finally, simulations were carried out on neutronic models of DEMO and VNS, tokamaks developed within the EUROfusion consortium, to enable a comparative assessment of the radiation environment across different reactor sizes and levels of design maturity.

PHITS has been extensively benchmarked against well-established transport codes such as MCNP (140–144), GEANT4 (142, 143, 145) and FLUKA (143, 146), consistently showing good agreement across shielding and particle-transport prob-

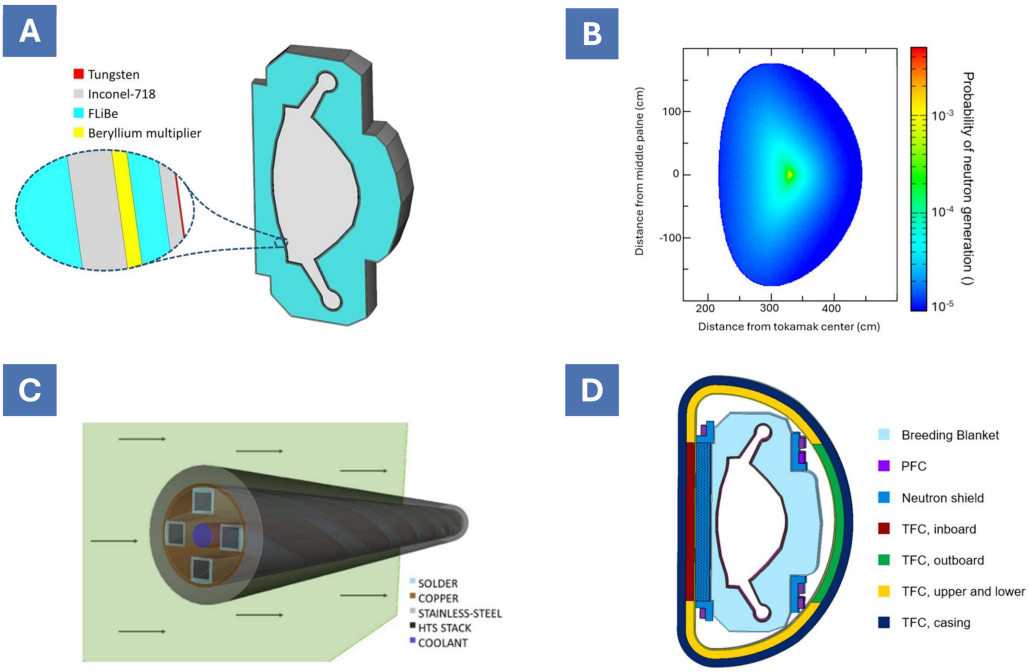

Fig. 2.1 A) SolidWorks model of the ARC-like reactor core employed for the MC workflow benchmark (9) B) Probability distribution of neutron generation for the plasma-shaped D–T source adopted in the simulations. C) Sketch of the VIPER cable and of the simulation layout (10) D) SolidWorks model of the complete ARC-like reactor, including the shielding elements and the coils (11)

lems. Previous applications in tokamak environments, particularly in shielding studies performed in Japan, further support its suitability for fusion-neutron calculations (147, 148). Within the first step of the present workflow, an additional comparison was carried out against the widely adopted OpenMC code (131) using the ARC reactor geometry, providing an independent validation of the PHITS results in a fusion-relevant configuration. The OpenMC neutron transport calculations were performed by Davide Pettinari within a collaborative project. Details of the model and simulation procedure are reported in Ref. (9).

This first set of MC simulations was performed on a detailed model of the vacuum vessel and breeding blanket of an ARC-like reactor (14), developed in SolidWorks. By focusing on the reactor core, the transport calculations could be carried out on a simplified yet fusion-relevant geometry, enabling both an efficient benchmarking of the MC framework and the characterisation of the neutron field upstream of the magnetic system, while remaining independent of assumptions on

its final design. The immersion blanket and the vacuum vessel are composed of seven concentric layers surrounding the plasma chamber (see Fig. 2.1A). Three of these layers are structural Inconel, while tungsten is employed as the plasma-facing first-wall material. A beryllium layer is included to enhance neutron multiplication and ensure that the required tritium breeding ratio can be achieved. FLiBe acts simultaneously as tritium breeder, coolant, and neutron moderator, occupying the remaining non-structural layers of the blanket.

A user-defined neutron source was implemented in PHITS to reproduce the spatial distribution of neutron emission expected from a D–T fusion plasma, and adopted for all the simulations at a reactor scale (Fig. 2.1B). The routine is based on the model introduced in Ref. (149), which parameterises the plasma geometry and reaction rate in terms of the relevant equilibrium quantities. The source has a toroidal geometry and its intensity varies according to the local plasma temperature and density profiles, both expressed as functions of the radial and angular coordinates. Neutron emission points are sampled by means of a rejection algorithm that enforces the desired spatial probability distribution, ensuring an accurate representation of the plasma-shaped source (see Fig. 2.1B). The neutron energy spectrum was taken as monochromatic at 14.1 MeV, corresponding to the primary D–T reaction energy. The Shafranov shift, elongation and triangularity were included in the definition of the source geometry, and the numerical values adopted in the present simulations are reported in Table 2.1. A total neutron yield of $1.8{\times}10^{20}$ n/s was adopted, corresponding to a fusion power of 525 MW (14).

Parameter	Variable	Value	Units
Major radius	R_0	3.3	m
Plasma semi-minor radius	a	1.13	m
Plasma elongation	κ	1.84	-
On-axis temperature	T_0	27	keV
On-axis density	n_0	$1.8 \cdot 10^{20}$	m^{-3}
Shafranov factor	-	0.44	-
Elicity	e	1.557	-
Triangularity	d	0.27	-

Table 2.1 Plasma parameters employed for the definition of the plasma source (14).

Within this model, the impact of different evaluated nuclear data libraries (JENDL-4.0 (139), ENDF/B-VIII.0 and JEFF), the adoption of a reduced com-

putational domain (a 10° sector of the reactor) with reflective boundary conditions, and the use of two different MC transport codes were systematically assessed. The most neutronically loaded region of the vacuum vessel was identified at the inboard midplane, and the corresponding outgoing neutron spectrum was selected as representative source for subsequent component-scale analyses.

For this purpose, the extracted spectrum was implemented in a planar neutron source emitting collimated neutrons toward a superconducting cable (Fig. 2.1C), allowing the transport problem to be decoupled from the full reactor geometry and enabling a substantial reduction in computational cost while preserving the physically relevant irradiation conditions experienced by the HTS. To approximate a periodic and symmetric arrangement representative of a cable embedded in a magnet winding, the superconducting cable was placed within a rectangular computational domain (defined as the outer boundary of the simulation volume, as required by the PHITS geometry specification) with reflective boundary conditions applied on the lateral faces.

The superconducting cable selected for this analysis was the VIPER design (150), originally conceived for application in compact fusion reactors and for which both the detailed geometrical parameters and the material composition are well documented. A three-dimensional model corresponding to one twist pitch of the cable was generated using COMSOL Multiphysics and imported into PHITS. Details about the model composition are provided in Table 2.2.

Table 2.2 Material composition in the VIPER model.

Component	Atomic mass fraction [%]														
	Fe	Cr	Ni	Pb	Sn	Mo	W	Mn	Co	Cu	N	Ag	Y	Ba	O
Solder	-	-	-	70	30	-	-	-	-	-	-	-	-	-	-
Internal jacket	-	-	-	-	-	-	-	-	-	100	-	-	-	-	-
Copper matrix	-	-	-	-	-	-	-	-	-	100	-	-	-	-	-
External jacket	71.9	16	10	-	-	2	-	-	-	-	0.1	-	-	-	-
HTS stack	2.08	8.08	29.7	-	-	8.86	1.56	0.52	1.3	42.32	-	4.73	0.16	0.49	0.2

From a geometrical standpoint, the cable consists of a copper-based structure hosting multiple stacks of HTS tapes distributed around its perimeter, embedded within a copper matrix and enclosed by an external structural jacket. A central channel is included to accommodate a cryogenic coolant, which was modelled as helium in the present work.

For simulations aimed at evaluating nuclear power deposition, a complete yet homogenised material composition of the superconducting stack was adopted, allowing an accurate estimation of energy deposition and heat generation in all constituent materials, as reported in Table 2.2. In contrast, for the evaluation of radiation-induced lattice damage, the superconducting stack was modelled as composed of pure YBCO, in order to isolate the effects of neutron irradiation on the superconducting phase. The cable configuration was analysed both in the absence of dedicated neutron shielding and by including a 50 cm thick ZrH_2 shielding layer between the neutron source and the superconducting cable, following (151, 152).

Despite the specific choice of the VIPER design, the detailed cable layout is not the focus of this study. Rather, the VIPER configuration is employed as a representative test case to quantitatively assess the irradiation experienced by an HTS conductor and its modification in the presence of a dedicated shielding layer under reactor-relevant conditions, thereby guiding subsequent shielding design choices. Variations in the specific cable layout are not expected to significantly affect the qualitative conclusions regarding radiation damage in the superconducting stack. Moreover, these simulations were also used to test the capability of directly coupling PHITS output with magneto-thermal analysis in COMSOL Multiphysics, generating a complete map of power deposition across the entire cable.

After the simulations of the cable, a complete ARC-like reactor model was developed to quantify neutron irradiation in a complete configuration. To this end, the reactor core described in the previous sections was complemented with the full magnetic system, including both PFCs and TFCs, their structural casings, and five dedicated neutron-shield elements, as proposed in ARC design studies (14, 151, 153) (see Fig. 2.1D). A summary of the main reactor components included in the model is reported in Table 2.3.

Consistently with the radiation-damage analyses discussed above, the superconducting winding pack was modelled as composed of pure YBCO, allowing a direct comparison between component-scale and reactor-scale damage estimates. Nine candidate materials were considered for the neutron-shield elements to protect the coils, namely GdH_3 (154), ZrH_2 (151), HfV_2 (155), VB (156), WB_4 (151), TiH_2 (157), WC (151), WB (151), HfH_2 (158, 159). These compounds were selected from materials documented in the scientific literature, spanning a range from widely used industrial materials, such as WC, a well-established compound employed in

Table 2.3 Thickness (evaluated at the outboard midplane) and total volume of each layer in the geometry definition of the model (20° sector).

Material	Component	Thickness (mm)	Volume (m^3)
Tungsten	First wall	5	9.70×10^{-2}
Inconel-718	VV inner structural material	20	3.95×10^{-1}
FLiBe	Coolant channel	20	3.97×10^{-1}
Beryllium	Neutron multiplier	10	2.00×10^{-1}
Inconel-718	VV outer structural material	20	3.96×10^{-1}
FLiBe	Coolant tank	1167	18.9
Inconel-718	Tank wall	30	7.94×10^{-1}
SS316L	TFC casing	40	1.13×10^{-1}
SS316L	PFC casing	10	1.96×10^{-2}
various	TFC shield	510	1.56
various	Outboard PFC shield	250	6.62×10^{-1}
YBCO	TFC	300	8.80×10^{-1}
YBCO	PFC	180	1.14×10^{-1}

nuclear and engineering applications, to more exotic candidates such as HfV_2, for which experimental data are available in the literature despite their more limited industrial use. To facilitate a quantitative comparison of the different shielding configurations, the toroidal-field coil was partitioned into four regions characterised by similar expected exposure levels. For each shielding option, integral damage metrics were evaluated over these regions, providing a compact set of figures of merit without the need to analyse full three-dimensional distributions at every stage.

To reduce the computational cost while preserving the correct neutron environment in the magnet region, only a 20° toroidal sector of the machine was modelled, with reflective boundary conditions applied at the two poloidal planes. This reduced CAD model was therefore imported into Altair SimLab to generate a tetrahedral mesh suitable for Monte Carlo transport, comprising approximately $3x10^6$ elements. A minimum element size below 5 mm was imposed to ensure an adequate representation of the thinnest structures in the reactor, in particular the first wall. This minimum size is enforced across all components, while the average element size is increased in large, relatively homogeneous regions (such as the FLiBe tank and bulk structural volumes) for simulation efficiency. Three-dimensional distributions of the relevant neutron-induced quantities were tallied on this mesh and later post-processed to extract both detailed maps and hot-spots values for the magnetic systems.

Once the radiation environment experienced by the coils of the ARC-like reactor had been determined, it was compared with that evaluated for two additional machines at a more advanced level of design, developed within the EUROfusion consortium, namely DEMO and VNS.

The model adopted for DEMO corresponds to the 2024 design of the DEMO Low Aspect Ratio (LAR) configuration, available in STEP format on the EUROfusion platform (160). The model includes the breeding blanket, the vacuum vessel, several ports, and the complete magnetic system (toroidal-field coils and casings, central solenoid, and poloidal-field coils, based on LTS).

The original CAD model did not correspond to the minimal symmetric sector of the reactor and presented several issues, including missing components in the port regions, overlapping geometries within the TFCs, and duplicated elements. The geometry was therefore processed and corrected using ANSYS SpaceClaim, where these inconsistencies were resolved. The model was then reduced to a 22.5° symmetric sector, corresponding to one sixteenth of the full torus, in order to optimise computational efficiency while preserving geometric fidelity.

A refined tetrahedral mesh was then generated in Altair SimLab and imported into PHITS using its native CAD-import tool. The mesh was constructed by adapting the element size to each domain, ensuring an accurate representation of the geometry.

A homogenised material composition was calculated for all reactor components, excluding the breeding blanket, based on data available in the literature (161). For the divertor, a homogenisation of the more complex structure proposed in the literature was performed, and the adopted values are reported together with those of the breeding blanket.

For the breeding blanket, a detailed volumetric breakdown was employed, derived from the CAD model of the water-cooled lithium–lead (WCLL) cassette available on the EUROfusion website (160). The specific material compositions were taken from the document “BB inputs for DEMO LAR EM model v1.0 – WCLL”, part of the official EUROfusion dataset (160), and are listed in Table 2.4.

Due to the large size of the DEMO model and the consequent high level of shielding, variance reduction techniques were required to achieve sufficient statistical precision in the coil regions.

Table 2.4 Elemental composition (wt%) adopted for the divertor and breeding blanket materials in DEMO.

Component	Weight fraction [wt%]																
	Fe	O	W	H	Cr	Cu	Mn	Ta	C	N	V	^{6}Li	^{7}Li	Ni	Si	Ti	Pb
Divertor	39.41	36.07	13.69	4.11	3.99	2.32	0.25	0.06	0.05	0.02	0.01	–	–	0.01	0.01	–	–
Breeding blanket	34.06	11.71	1.14	0.17	3.44	–	0.15	0.05	0.04	0.01	0.08	2.44	1.63	–	4.27	2.98	37.40

A set of neutron weight windows was generated using the native PHITS function T-WWG, applied directly on the same tetrahedral mesh used both to import the geometry and to tally nuclear quantities, with the aim of obtaining a more uniform spatial distribution of MC particles throughout the model, ensuring adequate sampling even in regions characterised by low particle flux (162).

The method assigns a statistical weight to each particle and defines an acceptable weight window for each mesh element. When a particle enters an element with a weight exceeding the upper bound of the local window, it undergoes splitting, producing multiple particles with proportionally reduced weight. Conversely, if a particle weight falls below the lower bound, it is subjected to Russian roulette, a probabilistic process in which the particle may be terminated. If it survives, its weight is increased to fall within the acceptable range. This selective treatment of particle weights reduces the computational effort associated with tracking low-importance particles in non-critical regions, allowing resources to be focused on more important and less frequently sampled areas of the geometry.

The weight window set was generated by PHITS through an iterative procedure based on the neutron flux distribution within the model. The process is considered converged when all relevant regions of the geometry are sufficiently sampled (162). In the present work, five iterations were required to achieve adequate convergence.

To further enhance computational efficiency, the low-energy unbiased method was applied. Specifically, the weight window for neutrons with energies below 1×10^{-2} MeV was set to be five times higher than that for higher-energy neutrons (162). As a result, only one in five low-energy neutrons survives the Russian roulette process. This approach allows PHITS to prioritise the transport of high-energy neutrons, which are most relevant for shielding calculations, thereby reducing computation time while preserving accuracy where it is most needed.

In accordance with literature data (163), a plasma fusion power of 1651.7 MW was assumed for the reactor, corresponding to a neutron yield of 4.43×10^{19} n/s

in the simulated sector. The same neutron source routine adopted for the ARC simulations was employed, with plasma parameters adjusted to the DEMO LAR configuration (163), as reported in Table 2.5.

Table 2.5 Plasma equilibrium parameters adopted for the DEMO LAR and VNS neutron source models.

Parameter	DEMO LAR	VNS	Unit
Major radius	8.66	2.55	m
Plasma minor radius	3.07	0.50	m
Triangularity	0.33	0.33	–
Plasma elongation	1.74	1.50	–
Shafranov factor	0.87	0.20	–

The other model adopted for comparison was the 2025 compact-tokamak design of the VNS, available in STEP format on the EUROfusion platform (164). The model includes the inboard and outboard breeding blanket, the divertor system (shield and divertor), the complete magnetic system, composed of toroidal-field coils (winding pack and casing), the central solenoid, and the poloidal-field coils, as well as the vacuum vessel with upper and lower ports, the port plug, the shield blanket, the neutral beam injector (NBI) liner, and the electron-cyclotron (EC) launcher. Differently from DEMO, in this case the poloidal-field coils are located inside the vacuum vessel. The simulations presented in this work adopted a magnet composition based on HTS, motivated by the interest of the consortium in exploring their radiation environment with a view toward their potential future use in reactor designs.

From the complete CAD model, a 60° sector representing the smallest repeatable unit of the reactor was extracted and processed in ANSYS SpaceClaim. The geometry was checked for potential issues, and unnecessary or duplicated surfaces, as well as overlapping regions, were removed. A refined tetrahedral mesh was then generated in Altair SimLab and imported into PHITS using its native CAD-import tool. The mesh was constructed by adapting the element size to each domain, ensuring an accurate representation of the geometry. The sector selected for the simulations does not include the EC launcher or the NBI liner, as these components were considered not relevant for the investigation of the magnetic systems.

A homogenized composition was calculated for all components based on their volume fractions, as recommended by EUROfusion internal communications, as summarized in Table 2.6

Table 2.6 Homogenised elemental composition (wt%) adopted for VNS components. Values marked as "–" indicate nuclides not included in the corresponding homogenisation.

Nuclide	Inner VV	Outer VV/ports/supports	Inboard blanket	Outboard blanket	Div. shield	Div. body	CS	PFC	TFC WP	TFC casing	Port plug
Fe	46.46	66.37	8.10	7.10	39.95	52.50	16.68	16.75	13.43	66.37	46.46
O	26.64	17.00	13.32	8.68	3.46	6.66	7.71	14.17	14.26	0.03	26.64
Cr	11.90	12.00	2.07	1.82	10.32	13.45	4.25	4.25	3.40	17.00	11.90
Ni	8.40	–	1.46	1.28	7.22	9.49	3.00	3.00	2.40	12.00	8.40
H	3.36	–	2.26	0.08	0.44	0.84	16.87	0.84	0.84	–	3.36
Mo	1.75	2.50	0.31	0.27	1.51	1.98	0.63	0.63	0.50	2.50	1.75
Mn	1.05	1.50	0.18	0.16	0.90	1.19	0.38	0.38	0.30	1.50	1.05
Si	0.35	0.50	0.06	3.59	0.30	0.40	3.42	5.89	5.86	0.50	0.35
N	0.07	0.10	0.01	0.01	0.06	0.08	0.03	0.03	0.02	0.10	0.07
C	0.02	0.03	0.04	–	0.02	0.02	5.61	9.81	9.81	–	0.02
W	–	–	58.30	–	31.70	13.40	–	–	–	–	–
Ti	–	–	13.91	–	–	–	–	–	–	–	–
Pb	–	–	–	73.50	–	–	–	–	–	–	–
Cu	–	–	–	–	4.07	–	30.00	37.14	41.79	–	–
Nb	–	–	–	–	–	–	17.53	–	–	–	–
Sn	–	–	–	–	–	–	7.47	–	–	–	–
Al	–	–	–	–	–	–	0.97	1.69	1.69	–	–
Ca	–	–	–	–	–	–	0.93	1.63	1.63	–	–
Mg	–	–	–	–	–	–	0.47	0.83	0.83	–	–
Ba	–	–	–	–	–	–	–	1.65	1.86	–	–
Y	–	–	–	–	–	–	–	0.53	0.60	–	–
B	–	–	–	–	–	–	0.16	0.33	0.28	–	–
Na	–	–	–	–	–	–	–	0.28	0.51	–	–

In accordance with literature data (165), a plasma fusion power of 30.4 MW was assumed for the reactor, corresponding to a total neutron yield of 1.1×10^{19} n/s. The value corresponding to a 60° toroidal plasma sector, 1.8×10^{18} n/s, was adopted as the emissivity of the neutron source in the Monte Carlo simulations. Also in this case, reflective boundary conditions were applied at the lateral boundaries of the model, and the PHITS plasma source routine was employed with parameters suited to the VNS configuration (165), as summarized in Table 2.5.

In all the simulations, neutron fluxes were calculated using the T-track tally, while energy deposition was obtained through the T-deposit tally. The displacement damage was evaluated with the T-dpa tally, and the spectra of PKAs were extracted using the T-product tally. The threshold displacement energies were set to the standard PHITS values, namely 25 eV for Y, Ba and O, and 40 eV for Cu (166).

2.2 Molecular Dynamics simulations

Once the reactor radiation environment has been described through MC transport simulations and the regions of highest displacement dose have been identified, the

next step is to resolve the microscopic structure of the damage and characterise the type of disorder effectively produced in YBCO. This information is required to formulate damage descriptors that go beyond a scalar displacement dose.

From the MC calculations, the spectra of PKAs can be extracted for each material region, providing the initial conditions for simulating individual collision events at the atomic scale. Molecular dynamics is used for this purpose: it integrates the equations of motion for the atoms within a simulation cell, with interatomic forces determined by a chosen potential. Starting from a primary knock-on atom of given species and energy, the resulting sequence of collisions is followed explicitly, allowing the cascade to be resolved and the stable defect structures to be identified.

All MD simulations presented in this thesis were performed with the CPU version of the LAMMPS code (167) , using a semi-empirical potential specifically developed at Lancaster University for radiation-damage studies in YBCO (130). In this model, short-range interactions are described by a Buckingham potential, while Coulomb terms between charged species account for the long-range electrostatics. As is customary in radiation-damage potentials, the universal Ziegler–Biersack–Littmark (ZBL) potential is smoothly joined to the Buckingham interaction at very short interatomic distances, in order to reproduce the screened nucleus–nucleus repulsion during high-energy collisions. This potential was selected as it represents, to the best of the author's knowledge, the most accurate description of interatomic interactions currently available for YBCO; the specific parametrisation of the hybridisation region is that defined in the original work (130), to which the reader is referred for full details.

T (K)	E_k PKA (eV)	Supercell size (replicas)
20, 300	1, 2, 5, 9, 15, 25, 50, 80	$30 \times 30 \times 10$
20, 300	140, 245, 430, 750	$45 \times 45 \times 15$
20, 300	1310, 2300, 4050	$60 \times 60 \times 20$
20, 300	7000	$60 \times 60 \times 20$
20	40×10^3, 60×10^3, 110×10^3 (only Ba PKA)	$480 \times 480 \times 160$

Table 2.7 Y, Ba, Cu, O PKAs, list and details of the performed simulations

It is well established that neglecting electronic stopping leads to a severe overestimation of the projected range of energetic ions (168). To avoid this artefact,

electronic energy loss was introduced in the simulations in the form of a friction term, obtained with the SRIM code (169).

Collision cascades were computed for PKAs of all atomic species present in YBCO (Y, Ba, Cu and O) at two temperatures, 20 K and 300 K. The PKA energies covered the interval from 1 eV up to 7 keV, sampled on a logarithmic grid as summarised in Table 2.7. Since the direction of the initial recoil has a pronounced influence in the low-energy regime, and given the structural complexity of YBCO, with four inequivalent oxygen sites and two distinct copper positions, a finer sampling was adopted for recoils below 100 eV. In this range, 21 random directions were selected for each crystallographic site; for higher energies, 11 directions per species were considered sufficient.

The size of the simulation cell was selected on the basis of the PKA energy, as summarised in Table 2.7. For each cascade event, a separate supercell was constructed, relaxed with the quickmin algorithm and subsequently equilibrated for 40 ps in the NPT ensemble. No common pre-equilibrated configuration was used, so that every run started from an independent state, avoiding correlations and eliminating biases associated with a specific initial condition. Periodic boundary conditions were applied in all three spatial directions (ppp condition in lammps) for every simulation cell.

During the cascade phase, the system was divided into two regions. A spherical core surrounding the PKA evolved in the NVE ensemble for 100 ps, allowing the collision sequence to unfold without external perturbations. The outer shell was coupled to a velocity-rescaling thermostat, to stabilise the simulation and remove the excess energy generated by the cascade (see Fig. 2.2).

For Ba PKAs at 20 K, additional reference cascades at 40, 60 and 110 keV were simulated in order to benchmark the high-energy events reconstructed through the BCA–MD coupling. Ten initial directions were sampled for each of these energies. Owing to the large system size required at such energies, the initial configurations were extracted from a single long equilibration trajectory by saving restart files at 5 ps intervals; each high-energy run was then launched from a different restart, ensuring independent starting states while reducing the computational cost associated with repeated equilibration.

The MD trajectories were analysed with the OVITO package (170), applying several post-processing routines tailored to quantify the primary damage. Point

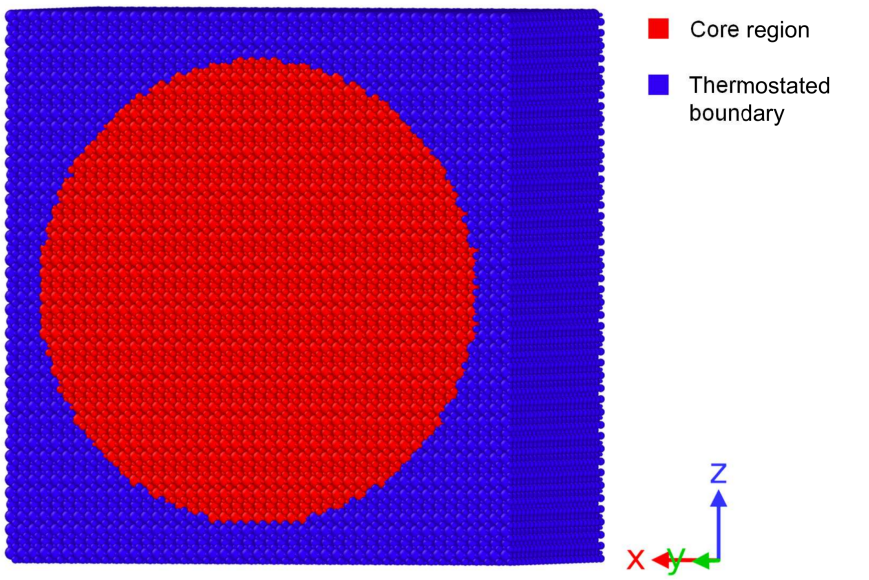

Fig. 2.2 Layout of the simulation cell used for cascade calculations, showing the central region (red) and the thermostated boundary layer (blue)

defects were identified through a Wigner–Seitz analysis, which compares the final atomic configuration to the ideal lattice and records vacancies, interstitials and antisite defects. For each PKA energy, the reported defect numbers correspond to averages over all sampled recoil directions, evaluated at 100 ps after the initiation of the cascade.

Since the spatial arrangement of defects plays a key role in determining their influence on superconducting properties, a clustering analysis was also performed. Using OVITO's standard modifiers, point defects were grouped according to a distance criterion, and each cluster was assigned a radius of gyration R_g, allowing the characteristic size of the damaged region to be quantified. When the distribution of defects is compact, as typically observed in low-energy cascades, the affected volume can be effectively approximated by a sphere of radius R_g.

Two defects were assigned to the same cluster if their mutual distance was smaller than a cutoff r_c. For YBCO, the natural length scale guiding this choice is the zero-temperature Cooper-pair coherence length, $\xi(0)\approx 1$ nm (171); accordingly, the cutoff was set to r_c=2 nm. With this threshold, all cascades in the sub-100 eV regime produced a single compact defect cluster with $R_g \approx 2$ nm, a property later exploited in the construction of the BCA-based cascade-reconstruction scheme.

2.3 Binary Collision Approximation

In a D–T fusion plasma, 14 MeV neutrons can generate in the magnets PKAs with energies that, for oxygen recoils, reach the MeV range (67). At such energies, a direct MD treatment of collision cascades would require very large simulation cells and small timesteps, making systematic sampling impractical. To access this part of the recoil spectrum, a BCA approach was therefore adopted in combination with MD.

In the BCA framework, the motion of energetic recoils is described as a sequence of independent two-body collisions between the PKA and target atoms, with trajectories determined by screened interatomic potentials and appropriate stopping models (169). This description is well suited to the high-energy, ballistic phase of a cascade, where many-body correlations are less important but the spatial extent and branching of the recoil tracks must still be captured. BCA simulations were therefore used to model the first stages of high-energy cascades beyond the energy range covered directly by MD, providing the distribution of secondary recoils and the basis for the overall geometry of large cascades.

All BCA calculations were carried out using the CASWIN code (12), developed at the University of Helsinki. To ensure consistency with the MD framework and with typical neutron-irradiation conditions, all PKAs were initiated within the bulk of the crystal. Reliable threshold displacement energies E_{d} were required for the simulations; these were determined specifically for this work through dedicated LAMMPS runs (167). Direction-dependent E_{d} values were computed for every atomic species, and the corresponding orientation-averaged thresholds used in the production calculations are reported in Table 2.8.

T (K)	Y	Ba	Cu1	Cu2	O1	O2	O3	O4
20	35.9	14.8	9.0	27.2	8.7	24.0	24.4	13.5
300	33.2	18.0	9.7	26.7	8.8	22.1	23.5	12.0

Table 2.8 Threshold Displacement Energies (in eV) used in the BCA simulations

For each element in YBCO, a total of 1250 cascades were simulated, sampling 27 recoil energies logarithmically distributed up to 3 MeV, at both 20 K and 300 K. A transition energy was selected to delimit the applicability of the BCA with respect to MD. During the BCA stage, each recoil was propagated until its kinetic

energy fell below this boundary. At that point, the simulation was terminated and its final state recorded for the coupling procedure. In particular, for every recoil, the atomic species, spatial coordinates, kinetic energy, direction of motion (polar and azimuthal angles), and its generation index (PKA, secondary, tertiary, and so on) were outputted, providing the information required for the subsequent multiscale analysis.

2.4 MD-BCA coupling scheme

The objective of combining MD and BCA calculations is to retain an atomistic description of defect production while extending the accessible recoil-energy range beyond that tractable by MD alone. In practical terms, the method aims to determine (i) the number of defects that survive after the cascade has cooled, (ii) the degree of defect clustering, and (iii) the characteristic size of the region structurally perturbed by the event, with MD precision. An overview of the workflow is presented in Fig 2.3.

In the hierarchical coupling scheme, each recoil produced in the BCA simulation is regarded as an independent initiator of a sub-cascade, i.e. a PKA. For every such recoil, the corresponding defect yield is obtained by interpolating the MD database as a function of recoil energy. The total number of defects associated with a given high-energy event is then computed by summing the interpolated yields over all recoils generated in the BCA cascade tree. For each PKA species and energy, the final defect yield was obtained by averaging these reconstructed defect counts over the 1250 cascades simulated with CASWIN.

To evaluate the reliability of the hierarchical procedure and to identify a suitable energy threshold separating the BCA-MD and the pure MD domains, the reconstructed cascades were benchmarked against full MD simulations of Ba PKAs at 40, 60 and 110 keV at 20 K. The comparison is summarised in Fig. 2.4A, where the total defect yield predicted by the coupled method is plotted as a function of the chosen transition energy, spanning cutoff values from some eV up to 7 keV. For all tested thresholds, the reconstructed defect counts fall within the statistical dispersion of the full-MD results, indicating that the assumptions underpinning the coupling procedure are consistent with explicit atomistic simulations. Moreover, once the cutoff exceeds

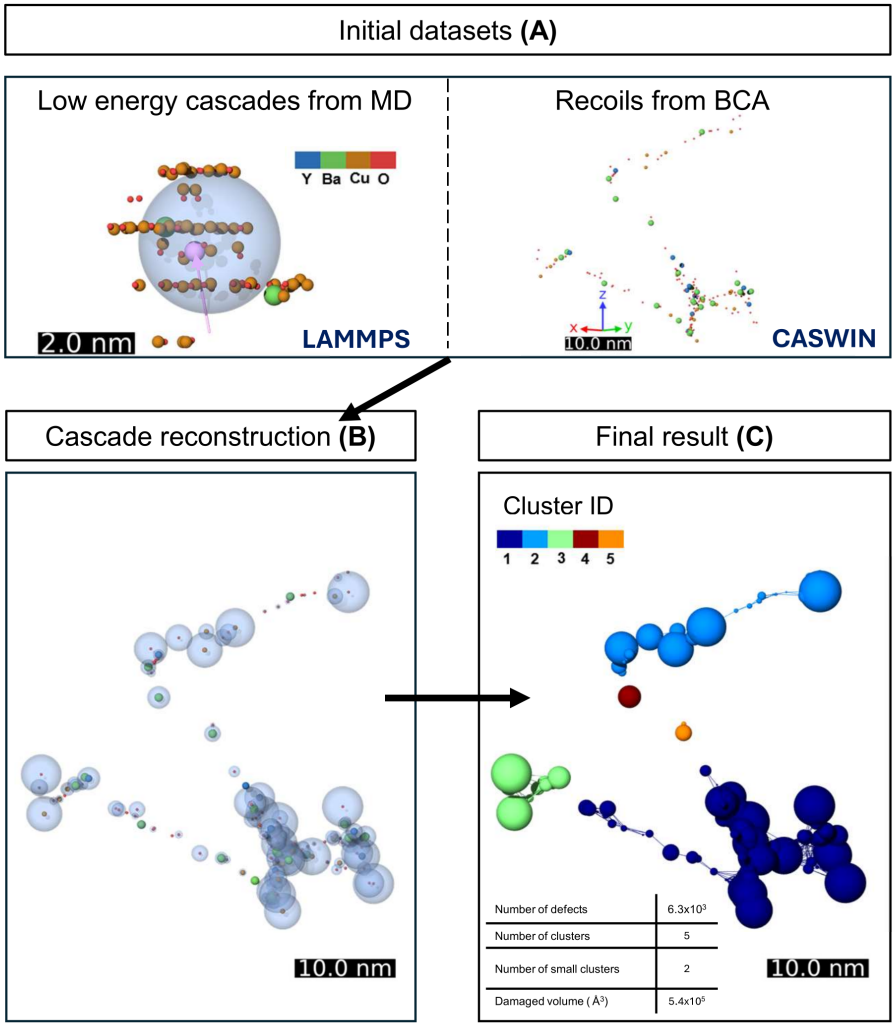

Fig. 2.3 A) Illustration of the input datasets. Top: example of a low-energy Ba cascade at 245 eV obtained from MD simulations, representative of the MD database up to 2 keV for the various atomic species. The resulting defect distribution forms a compact region that can be approximated by a sphere with radius of gyration R_g centered on the PKA initial direction of motion. Bottom: Example of the recoils generated by a 60 keV Ba PKA in CASWIN (12), showing the high-energy branching structure that defines the skeleton of higher energy cascades. B) Reconstruction procedure. Every BCA recoil falling within the MD energy range is mapped to a virtual spherical damage region, with radius R_g(E) and defect yield assigned through interpolation of the MD dataset. C) Reconstructed cascade and clustering analysis. Spheres are connected into clusters when the separation between their surfaces is smaller than 2ξ (with $\xi \approx 1$ nm the superconducting coherence length). The resulting geometry can be exported in CAD format, enabling the evaluation of the total damaged volume through Gmsh. Adapted from (8)

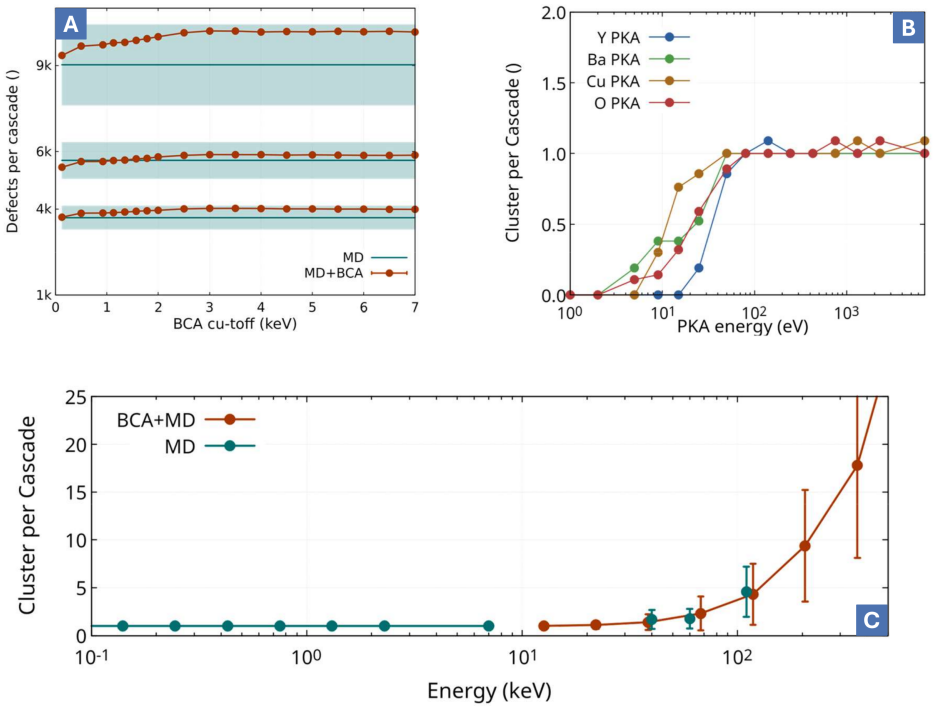

Fig. 2.4 A) Comparison between the mean number of defects per PKA obtained from full MD simulations and from the hierarchical BCA–MD reconstruction, shown as a function of the transition energy selected between the two methods (Ba PKA, 40, 60 and 110 keV). Across the entire range of tested cutoff values, the reconstructed results remain within the statistical spread of the MD data. B) Mean number of defect clusters generated in MD cascades with PKA energies below 2 keV at 20 K, evaluated using the clustering criterion introduced in the text. In this energy window, cascades almost always produce a single compact cluster, apart from occasional statistical outliers; this behaviour greatly facilitates the geometric reconstruction of higher-energy cascades within the BCA–MD framework. C) Predicted number of defect clusters per cascade for Ba PKAs at 20 K, obtained from full MD simulations (blue) and from the BCA–MD reconstruction (red). The two approaches exhibit an excellent agreement. Data from (8).

roughly 2 keV, the predicted defect number exhibits negligible dependence on the precise value of the transition energy.

For these reasons, a cutoff energy of 2 keV was adopted. This value is not only supported by the benchmark against full-MD simulations, but is also consistent with observations in other crystalline materials, where the onset of subcascade formation is typically reported around a few keV (172). Moreover, the 2 keV threshold is particularly convenient from a practical standpoint: all MD cascades below this energy generate a single compact defect cluster under the grouping criterion introduced in ch. 2, a useful property for the reconstruction procedure (Fig. 2.4B).

Evaluating clustering within a reconstructed cascade is necessarily different from the procedure used in direct MD simulations. In MD, each vacancy or interstitial has a well-defined atomic coordinate, allowing cluster identification through a straightforward distance criterion. In the reconstructed case, instead, the defect distribution is inferred from the recoil history: the number of defects associated with each recoil is obtained by interpolation from the MD dataset, and explicit defect positions are not generated.

To overcome this, a geometric surrogate informed by the MD results was adopted. Cascades in the MD energy window produce compact defect clouds whose extent is well characterised by the radius of gyration R_g; the defects produced by each recoil in the reconstructed cascade can therefore be represented by a spherical damage region centred along its propagation direction and assigned the corresponding MD-derived radius. This behaviour justifies the use of spherical damage regions in the reconstruction workflow and provides a consistent basis for defining defect clustering in the coupled BCA–MD framework.

Building on these considerations, every recoil generated by CASWIN was represented by a virtual spherical region. Its radius R_g was obtained by interpolating the MD database according to the recoil species and energy, while its centre was positioned along the recorded PKA trajectory, displaced by R_g from the recoil position so as to reflect the spatial extent of the corresponding MD cascade.

Since OVITO's distance-based clustering algorithm does not account for particle radii and relies solely on centre–centre separations, an explicit bond network was constructed. Two spherical regions were connected whenever the gap between their

surfaces fell below the prescribed cutoff r_c, namely when

$$d_{ij} - \left(R_i + R_j\right) \leq r_c,$$

where d_{ij} is the distance between the sphere centres and R_i and R_j their respective radii. Cluster identification was then carried out by applying OVITO's bond-based clustering routine to this graph.

High-energy Ba cascades obtained directly from MD were analysed in parallel and used as a benchmark for the reconstructed cascades. The comparison shows an excellent agreement between the full-MD and the MD-BCA results (Fig. 2.4A and C), confirming the reliability of the reconstruction procedure.

Once the cascades had been reconstructed in terms of virtual spherical regions, the volume of material affected by defects was estimated by exporting the geometry to a CAD format and computing the corresponding volumes with Gmsh (173). From the resulting cluster volumes, we determined the occurrence of small clusters, defined here as those whose volume is smaller than that of a sphere with radius ξ.

Chapter 3

Results

In this section, the results obtained in this thesis are presented following the logical structure of the adopted multiscale approach. The Monte Carlo transport framework is first validated on a compact fusion reactor core, assessing both its internal consistency within PHITS and its agreement with independent calculations performed using OpenMC.

Neutron spectra are initially compared using the full 360° reactor geometry, and subsequently employed to evaluate the impact of domain reduction and to justify the adoption of reflective boundary conditions. The sensitivity of the results to the choice of evaluated nuclear data libraries is then examined, providing the basis for the selection of the PHITS native library for all subsequent calculations.

Building on this validated transport framework, the analysis is extended from simplified reactor-core configurations to component-scale simulations, focusing on a representative superconducting cable, and finally to the complete ARC-like reactor model, where nine different shielding materials are systematically investigated.

The radiation environment predicted for this compact high-field reactor concept is then compared with that obtained for DEMO and VNS, enabling a cross-machine assessment of neutron irradiation levels in magnet systems across different reactor sizes and design maturity. The method is first applied to electron and fission-neutron irradiation scenarios discussed in the Introduction, demonstrating its capability to capture qualitative differences in the induced defect landscape, and is subsequently extended to the inboard segment of the toroidal-field coils. On this basis, estimates

of the time required to reach the damage levels identified for neutron irradiation at 4 mdpa are derived for the different shielding configurations.

3.1 Comparison of PHITS against OpenMC for fusion-relevant neutron transport

The results presented in this chapter are aimed at validating the Monte Carlo transport framework adopted in this thesis. A systematic comparison between PHITS and OpenMC is carried out on an ARC-like reactor model, progressively introducing and evaluating the modelling choices that are subsequently employed throughout the work. Neutron spectra were first compared on the Inconel-718 structural layers of the full 360° reactor model. In this initial comparison, no boundary conditions were applied, and the same evaluated nuclear data library was used in both transport codes, namely ENDF/B-VIII.0, which was selected as it is widely adopted in the fission neutronics community and is supported by both codes, ensuring a consistent basis for comparison (see Fig. 3.1).

The two codes yield very similar results for the first two structural layers, which are closest to the plasma source. On the other hand, for the third structural layer, located farther from the neutron source, some discrepancies are observed in the lower energy tails.

Nevertheless, the overall spectral features remain consistent between the two calculations, and noticeable deviations in the absolute flux appear only at energies below approximately 1 keV, a region of limited relevance for the neutronics quantities of interest in this work.

On the basis of the good agreement observed on the full 360° geometry, the analysis was extended to a reduced-domain configuration consisting of a 10° toroidal sector with reflective boundary conditions on the lateral faces. This allowed two independent comparisons to be performed: first, between the full and reduced geometries within the same Monte Carlo code, to assess the impact of domain reduction; and second, between PHITS and OpenMC for a given geometrical model, to quantify code-to-code differences also in this case.

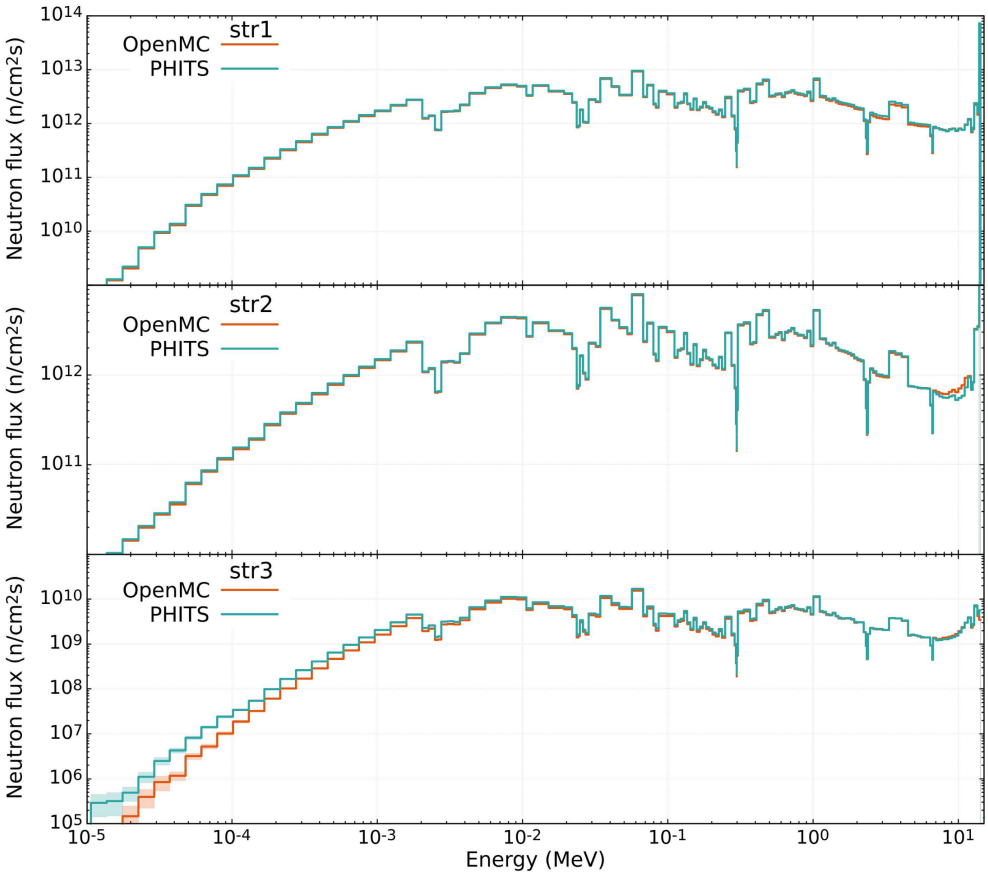

Fig. 3.1 Neutron spectra computed over the structural layers of the vacuum vessel with PHITS (teal lines) and OpenMC (orange lines). The calculations were performed over the complete model, adopting the ENDF/B-VIII nuclear library. Adapted from (9).

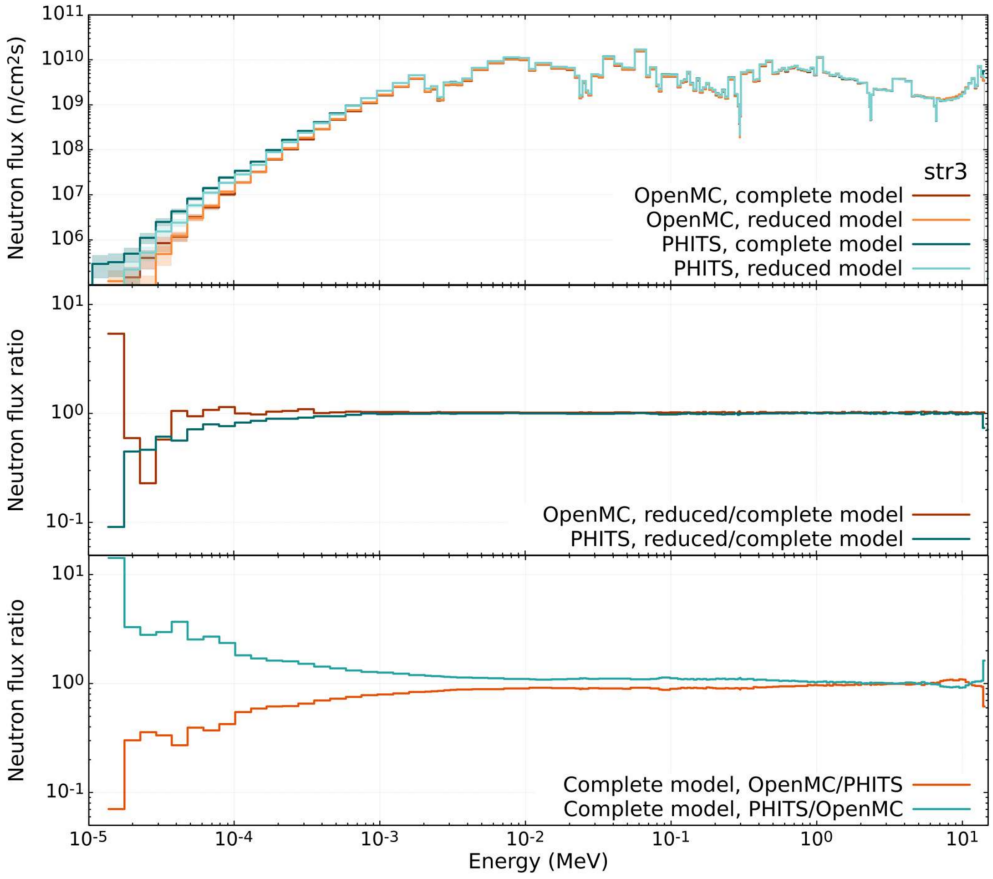

Fig. 3.2 Top panel: neutron energy spectra calculated on the outer structural layer str3, comparing the 10° sector model with reflective boundary conditions (light hues) against the full 360° geometry (dark hues), as obtained with PHITS (teal tones) and OpenMC (red tones). Middle panel: spectral ratios between the 10° sector and the corresponding 360° model results, evaluated separately for each Monte Carlo code. Bottom panel: Spectral ratios between PHITS and OpenMC results for the full 360° configuration. Adapted from (9).

The neutron spectra evaluated on the third Inconel structural layer, chosen as a conservative scenario, being the layer with the largest discrepancies, remain in close agreement when switching from the full model to the reduced-domain representation within a given code. A similarly good qualitative consistency is observed when comparing PHITS and OpenMC predictions for the same geometry, even in this conservative case (Fig. 3.2, top).

A quantitative analysis based on flux ratios further clarifies the relative impact of the two modelling choices. Above approximately 1 keV, neither the transport code nor the adoption of reflective boundary conditions significantly affects the predicted spectra. At lower energies, differences associated with the Monte Carlo implementation become more apparent, while the effect of domain reduction emerges only below about 100 eV. A minor discrepancy between the two codes is also observable at the highest energies, in the MeV range; however, this deviation is small in absolute terms and becomes apparent only when examining flux ratios. In the energy range most relevant for displacement damage and primary knock-on atom production, both effects therefore remain limited.

Integral quantities support these observations. For power deposition, excellent consistency is found between full and reduced geometries within each code, while differences between PHITS and OpenMC remain within the 5–15% range, with the largest deviations occurring in the beryllium neutron-multiplying layer (Fig. 3.3A). These results are also in agreement with values reported in the fusion-neutronics literature, despite differences in reactor geometries and modelling assumptions (152, 153, 174). The tritium breeding ratio (the ratio between the number of tritium nuclei breeded in the reactor and the number of triutium nuclei burnt in the plasma per second (24)) exhibits an equally robust behaviour. The values obtained with PHITS and OpenMC differ by only 1–2%, and the effect of to the adoption of a reduced computational domain appeared negligible (Table 3.1).

As part of the benchmark analysis, neutron spectra were evaluated at several locations along the vacuum vessel, in order to characterise the spatial variation of the neutron field downstream of the reactor core. This analysis allowed the identification of the inboard midplane as the most neutronically loaded region of the vessel, extracting neutron spectrum outgoing from the vacuum vessel at this location, to be adopted as a representative and conservative reference for the subsequent component-scale analyses.

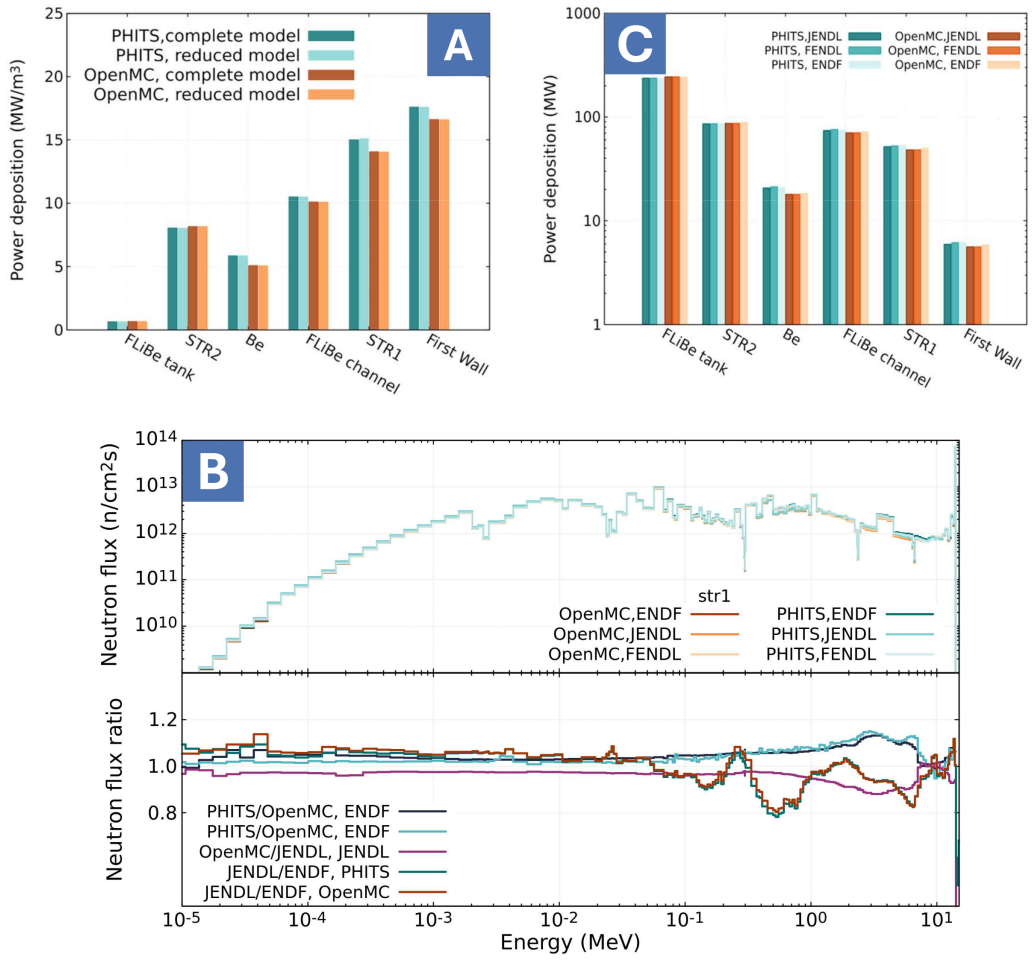

Fig. 3.3 A) Volumetric power deposition as computed by PHITS (teals tones) and OpenMC (red tones) for the reduced and complete model, evaluated with ENDF/B-VIII.0 nuclear libraries B) Upper panel: neutron energy spectra evaluated on the first Inconel layer within the reduced computational domain, obtained using the JENDL-4.0, FENDL-3.2, and ENDF/B-VIII.0 nuclear data libraries. Results are shown for PHITS (teal tones) and OpenMC (red tones). Lower panel: selected flux ratios derived from the spectra in the upper panel. The curves illustrate code-to-code discrepancies for JENDL-4.0 (purple), ENDF/B-VIII.0 (black), and FENDL-3.2 (cyan), as well as differences between the default libraries adopted by each code when considered independently (teal for PHITS and red for OpenMC) C) Total power deposition for each domain of the model, as computed by PHITS (teal tones) and OpenMC (red tones) with all the tested nuclear libraries. Adapted from (9).

Code	Geometry	Library	TBR value ± uncertainty (1 σ)
PHITS	full domain	ENDF/B-VIII.0	1.0766 ± 0.0001
PHITS	full domain	JENDL-4.0	1.0736 ± 0.0001
PHITS	full domain	FENDL-3.2	1.0703 ± 0.0001
PHITS	10° domain + reflective BC	ENDF/B-VIII.0	1.0761 ± 0.0001
OpenMC	full domain	ENDF/B-VIII.0	1.0626 ± 0.0001
OpenMC	full domain	JENDL-4.0	1.0737 ± 0.0001
OpenMC	full domain	FENDL-3.2	1.0495 ± 0.0001
OpenMC	10° domain + reflective BC	ENDF/B-VIII.0	1.0625 ± 0.0001

Table 3.1 TBR values computed with the two MC codes for the different geometries and libraries considered.

A final sensitivity study was performed to quantify the influence of the nuclear data library on the predicted neutron spectra, tritium breeding ratio and power deposition. The same transport calculation on the reduced-domain model was repeated using three different evaluated datasets, ENDF/B-VIII.0, JENDL-4.0 and FENDL-3.2, while keeping the geometry, source definition and numerical settings unchanged. The neutron spectra comparison was performed on the first Inconel structural layer, which exhibits the smallest relative statistical uncertainty among the analysed regions (Fig. 3.1B).

Differences in the neutron spectra arising from the choice of nuclear data are more pronounced than those associated with domain reduction. This is evident from the comparison of flux ratios between the various libraries: at low energies, relative deviations remain below approximately 10%, while in the fast-neutron region above 1 keV discrepancies can reach values on the order of 20%. Despite these differences, the overall spectral features relevant for magnet irradiation remain consistent across the tested datasets (Fig. 3.3B).

In contrast, integral quantities display a differentiated degree of robustness depending on the comparison level. When a single Monte Carlo code is fixed (e.g., PHITS), power deposition values obtained with the three different nuclear data libraries are in excellent agreement. Conversely, when different codes are compared using the same library, the agreement remains good and reproduces the behavior already observed in the PHITS–OpenMC comparison performed with the ENDF/B-VIII.0 library for different geometrical models (Fig. 3.3C). The tritium breeding ratio, conversely, shows a higher sensitivity to both the transport code and the nuclear data library (Fig. 3.1). For all datasets except JENDL-4.0, OpenMC predicts

systematically lower TBR values than PHITS, while good agreement between the two codes is recovered when using JENDL-4.0. The largest discrepancy is observed for the FENDL-3.2 library. It should be noted that both JENDL-4.0 and FENDL-3.2 are not distributed as native OpenMC libraries and were processed by the authors. Nevertheless, the observed differences remain of the order of a few percent and in general within a given transport code, variations associated with the nuclear data choice remain limited and do not alter the qualitative conclusions drawn from the neutronic analysis.

On the basis of these results, the reduced-domain ARC model combined with PHITS and the JENDL-4.0 nuclear data library was adopted for all subsequent Monte Carlo calculations. The benchmark against OpenMC demonstrates that this setup provides a reliable description of the neutron environment relevant for fusion reactors, while offering the computational efficiency required for reactor-scale and multiscale analyses.

3.2 Neutron irradiation and shielding assessment at cable scale

Having established the reliability of the Monte Carlo workflow on a reactor-relevant configuration and identified the neutronically most loaded region downstream of the reactor core, the analysis was extended to the irradiation environment experienced by a superconducting cable representative of HTS conductors. The cable was exposed to a collimated neutron field generated by a planar source, with an energy spectrum corresponding to that identified at point A of the vacuum vessel in the previous chapter.

In the absence of any dedicated neutron shielding, the neutron spectrum evaluated on the superconducting cable closely resembles the spectrum emerging from the vacuum vessel (Fig. 3.4A, top panel). Besides the expected attenuation of the high-energy component, a pronounced increase in neutron flux is observed on the HTS stack at energies below approximately 5 MeV, as becomes evident when examining the spectral ratio between the HTS spectrum and the vacuum-vessel outgoing spectrum (Fig. 3.4A, bottom panel). Given the reduced dimensions of the cable and the relatively small population of neutrons in the highest energy groups of

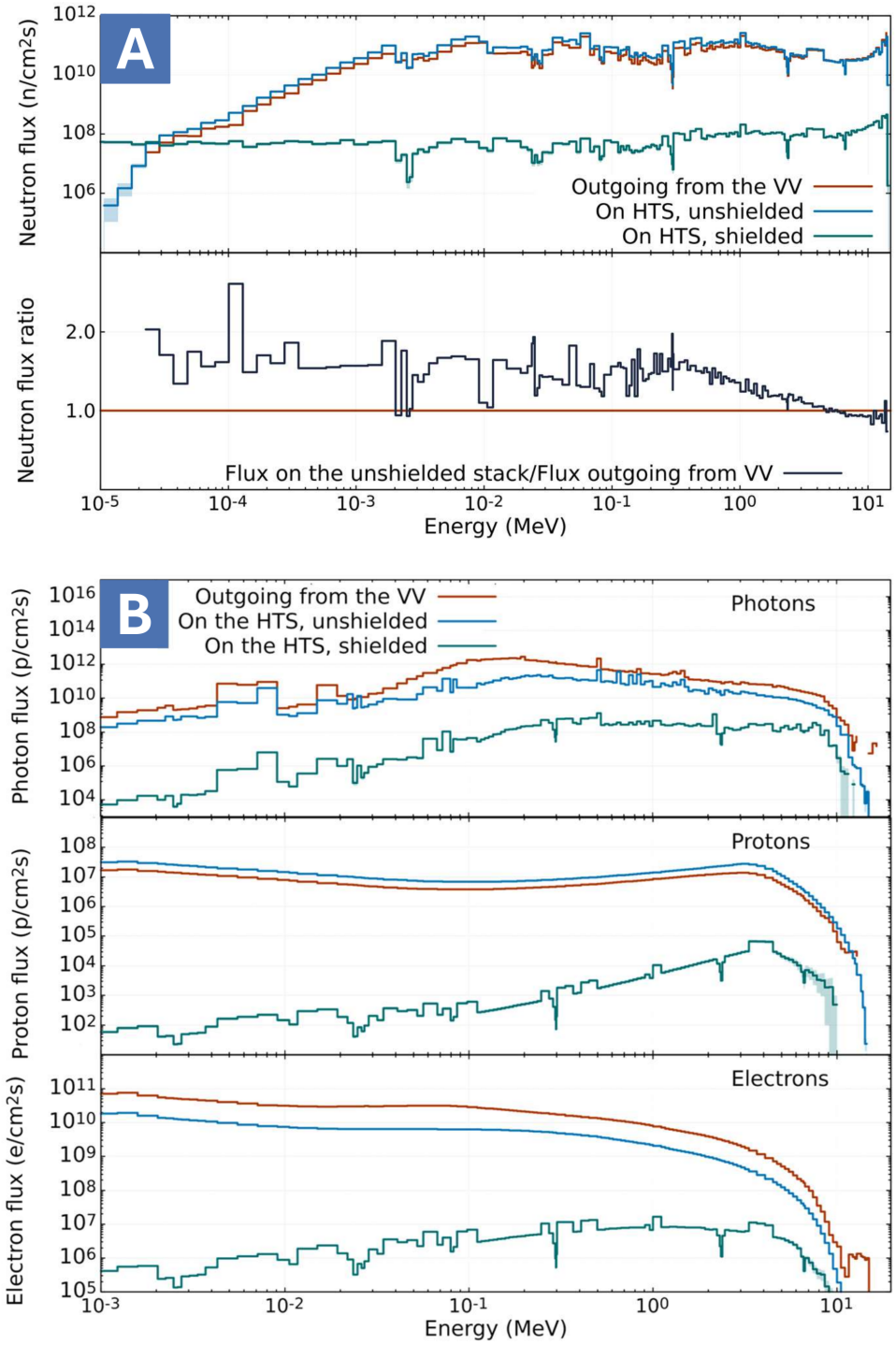

Fig. 3.4 A) Neutron, electron, proton and photon spectra on the HTS stack, with and without shielding. B) Integral power deposition on the domains of the cable, without (left) and with (right) shielding C) Power deposition distribution over the cable. Adapted from (10).

the source spectrum (3.6–14.1 MeV) compared to the low-energy tail, this behaviour cannot be explained solely in terms of a spectral shift due to neutron moderation.

Rather, the results indicate a genuine increase in the total neutron population, pointing to the contribution of neutron multiplication processes, primarily associated with inelastic (n,xn) reactions occurring within the cable materials. This interpretation is supported by the increase in total neutron flux, which rises from $7.7 * 10^{12} \pm 2 * 10^{11}$ n/cm^{2}s at the source boundary to $1.13 * 10^{13} \pm 1 * 10^{10}$ n/cm^{2}s on the HTS stack.

The observed increase in the neutron population can be interpreted in light of the nuclear properties of the materials composing the cable. The external jacket is primarily based on stainless steel, with Fe, Ni and Cr as dominant constituents, while Pb and Sn are employed in the solder. The HTS stack and the internal matrix are largely composed of Cu and Ni, with copper also present in the internal jacket.

For the most abundant isotopes of these elements in natural composition, non-negligible (n,2n) reaction cross sections are present at fusion-relevant neutron energies. In particular, cross sections exceeding approximately 100 mb are found for incident neutron energies above about 11 MeV, with lower thresholds (around 7 MeV) for isotopes such as 208Pb and Sn (175). These characteristics are consistent with the occurrence of neutron multiplication processes contributing to the flux increase observed in the unshielded configuration. This interpretation is further supported by the medium-wise collision statistics provided by PHITS, which show a comparable frequency of (n,xn) reaction rates across all cable materials, alongside a predominance of capture reactions in stainless steel and the copper matrix. A dedicated pathway analysis performed with the FISPACT-II inventory code independently confirmed the contribution of (n,xn) reactions as a primary source of neutron multiplication, consistently with the cross-section arguments outlined above.

In addition to neutrons, the spectra of secondary photons, electrons and protons generated by neutron interactions were analysed both at the reactor boundary (point A) and within the superconducting cable (Fig. 3.4B). The electron spectra produced in the cable closely resemble those originating from the reactor structures, reflecting the local nature of electron generation and the similar elemental composition of the two systems, which are both dominated by Ni, Cu, Fe and Cr. Analogous considerations apply to the proton and photon spectra.

Owing to the short attenuation lengths of secondary radiation, these particles produce predominantly localised effects, with characteristic ranges spanning from centimetres for photons down to micrometres for charged particles (176). As a consequence, secondary radiation generated in the vacuum vessel will not directly contribute to the irradiation of the superconducting system, being largely attenuated by the intervening cryostat structures.

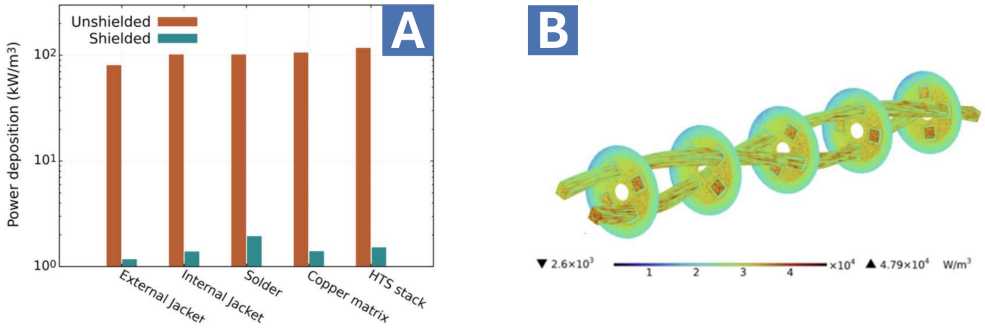

Fig. 3.5 A) Integral power deposition on the domains of the cable, without (teal) and with (red) shielding C) Power deposition distribution over the cable. Adapted from (10).

Being extremely relevant for superconducting performances, the power deposition was computed on each subdomain of the cable. As can be noted the most sensitive element in the cable, the HTS stack, is also the most heated per unit volume, with about 117 kW/m^3 (Fig. 3.5B). This is due to the material composition of the stack, including a not negligible amount of Ni, prone to nuclear reactions. This result exceeds the 50 W/m^3 design limit commonly adopted for nuclear heating in DEMO toroidal-field coils (177). However, it should be noted that this reference value was established for low-temperature superconducting magnets and is mainly driven by cryogenic power considerations. The relevance of this limit for high-temperature superconducting magnets depends on the specific cooling-system design, details of which are not presently available.

Thanks to the capabilities of PHITS, the power deposition on the whole cable was also detailed mapped over the whole cable (Fig. 3.2C), allowing to adopt the output of a MC calculation for finite element analysis of the thermomagnetic behaviour. The details of these calculations are beyond the interest of this thesis, but details can be found at Ref. (178).

The radiation damage suffered by the lattice strongly supports the necessity of a proper shield for the cable, with an NRT displacement damage of 0.4 dpa per full-power year of operation.

Experimental studies under fission neutron irradiation indicate that superconducting properties start to degrade significantly beyond a dose of approximately 4 mdpa, a threshold inferred from critical temperature degradation rates reported in (179), combined with critical current degradation curves from neutron irradiation experiments (107). When this value is used as a rough reference metric, and under the simplifying assumption that fission and fusion neutrons induce comparable damage regimes in terms of dpa, the corresponding threshold would be reached after roughly 4 days of operation. Even within this conservative, order-of-magnitude framework, such a timescale is clearly incompatible with the operational requirements of a fusion reactor.

It is worth noting that transmutation and the associated decay-recoil cascades represent an additional potential source of radiation damage not explicitly addressed in this work. Accounting for this contribution would require a substantially more complex workflow, involving the evaluation of time-averaged activities, decay spectra reconstruction, and cascade analysis for transmutation products. The present work is therefore deliberately focused on prompt ballistic damage induced by neutron irradiation, which represents the dominant damage mechanism during operations, and which constitutes the current primary focus of the fusion neutronics community for HTS magnet assessment.

The introduction of a simple 50 cm thick ZrH_2 shielding layer has a strong impact on the neutron flux incident on the cable, leading to a substantial reduction of the neutron field and to a pronounced thermalising effect. In particular, the total neutron flux computed on the HTS stack decreases to $3.91 \times 10^{10} \pm 9 \times 10^{6}$ $\mathrm{n\,cm^{-2}\,s^{-1}}$, corresponding to an abatement of about three orders of magnitude (Fig. 3.4A). This mitigation of the neutron field is also reflected in the emission of secondary particles: their energy spectra are significantly altered by the moderated neutron flux, and the overall secondary-particle fluxes are reduced by several orders of magnitude (Fig. 3.4B). In addition to limiting permanent lattice damage, suppressing these secondary charged-particle and photon fluxes is equally important, as their presence may induce transient perturbations of the superconducting condensate and affect the stability of the superconducting state.

The introduction of neutron shielding significantly improves the irradiation conditions, reducing the power deposition across all cable subdomains by approximately two orders of magnitude (Fig. 3.5B). Under these conditions, the predicted displacement damage decreases to 0.6 mdpa per full-power year, corresponding, within the adopted damage metric, to an estimated magnet lifetime of approximately 6 FPY; however, the inclusion of a 50 cm-thick dedicated shield within the reactor represents a non-negligible integration constraint, owing to the substantial thickness required.

It should finally be emphasized that this result constitutes a preliminary step toward bringing the system back into an acceptable operational window, for which the present shielding configuration proves sufficient in terms of radiation damage. Further extensions of the expected magnet lifetime are expected to arise primarily from an optimized choice of shielding materials rather than from additional increases in shield thickness, which would impose increasingly severe constraints at the reactor level.

3.3 Radiation environment of the ARC-like reactor model

Having established the necessity of a dedicated neutron shield and identified a representative shield thickness at the inboard midplane providing a significant reduction of radiation damage, the ARC reactor model was extended to include both TFCs and PFCs, according to the most recent models published in the literature (152). The shielding elements were incorporated into the geometry in order to investigate the radiation environment experienced by the magnetic system under reactor-relevant conditions. Due to their proximity to the breeding blanket, the PFCs were also equipped with dedicated shielding, thought with a reduced thickness compared to that adopted for the TFC.

In order to rapidly screen the shielding performance of the proposed materials, integral neutron flux and power deposition were evaluated in the inboard midplane region of the TFC, identified as the most critical location in the previous steps, while displacement damage was assessed for all four regions defined for the TFCs as well as for the three symmetric poloidal-field coils.

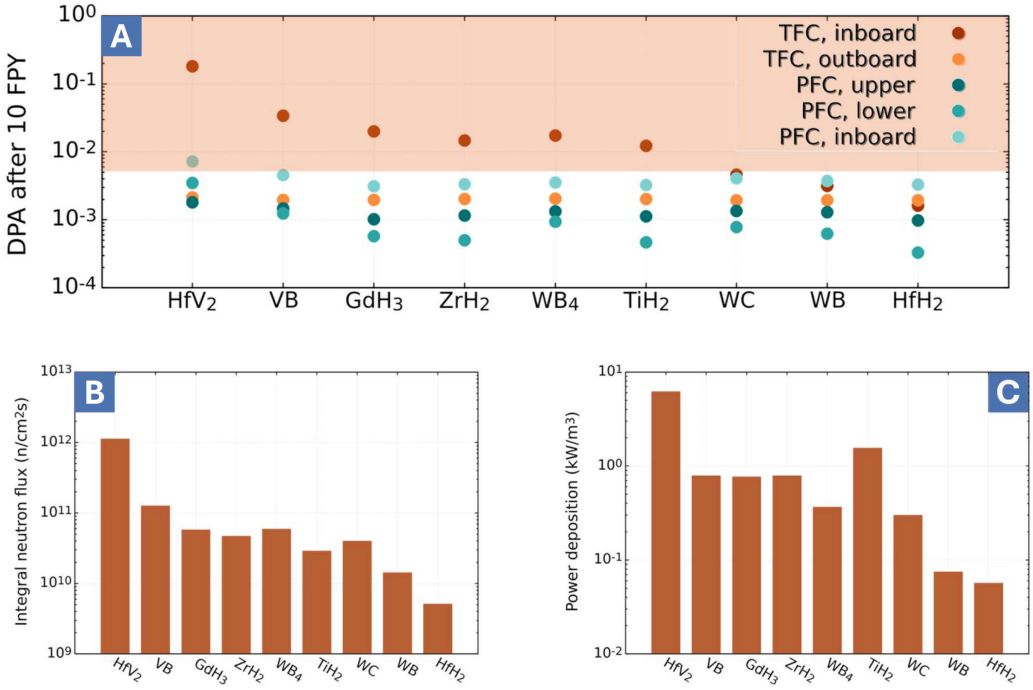

Fig. 3.6 A) Radiation damage dose accumulated over 10 FPY at the TFC inboard and outboard segments, and in the poloidal field coils. Regions where the damage exceeds the commonly adopted reference threshold of 4 mdpa are highlighted in red shading to provide a preliminary screening of the irradiation response. B) Integral neutron flux over the inboard segment of the TFC. C) Volumetric power deposition within the inboard segment of the TFC. Adapted from (11).

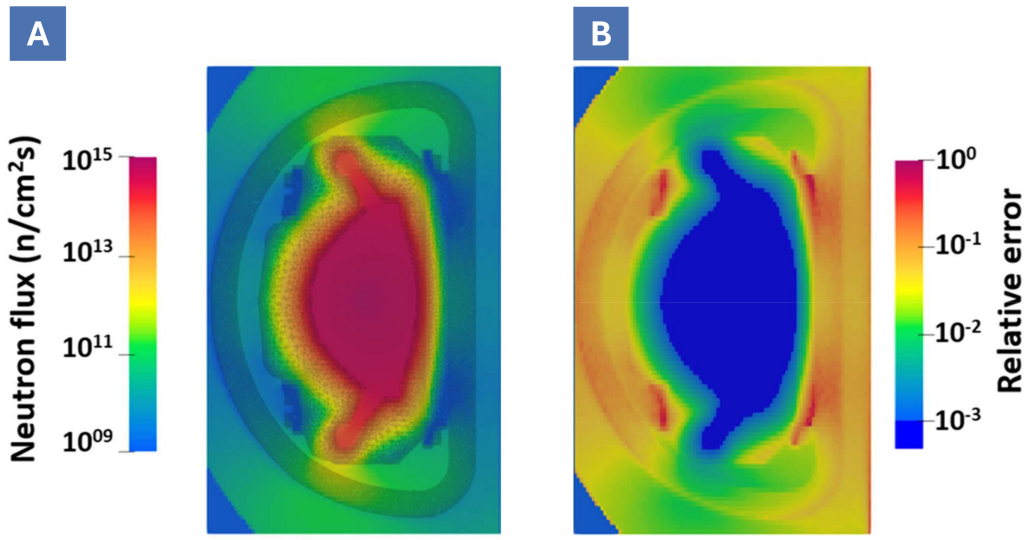

Fig. 3.7 Total neutron flux map (left) with its uncertainty (right), considering the best shielding option, HfH_2. Adapted from (11).

These integral metrics confirm that the toroidal field coils remain, on average, the most heavily irradiated components of the system. In particular, when focusing on the inboard region of the TFCs, both power deposition and displacement damage closely follow the modulation of the incident neutron flux, with material-dependent deviations arising from differences in neutron spectral shaping and photon production cross sections of the shielding materials (Fig. 3.8).

Compared with the unshielded configuration discussed in the previous chapter, radiation damage levels are consistently reduced across all shielding options. This reduction is especially pronounced for the PFCs, which remain well below the adopted reference threshold of 4 mdpa in all configurations. For the TFCs, while all shielding materials ensure a multi-year operational lifetime according to this metric, only three candidates indicate the potential to reach a 10-year lifespan.

Conversely, the resulting integral power densities remain of the order of a few kW/m^3 for all materials, a level higher than the reference limits recommended for DEMO magnets. However, as discussed in the previous chapter, this reference value is very conservative, and the actual details of the cooling system, and consequently the final limits for the allowable power deposition, are not defined at this stage for a conceptual reactor like ARC. Among the materials considered, HfH_2 provides the best overall performance in terms of flux attenuation, power deposition

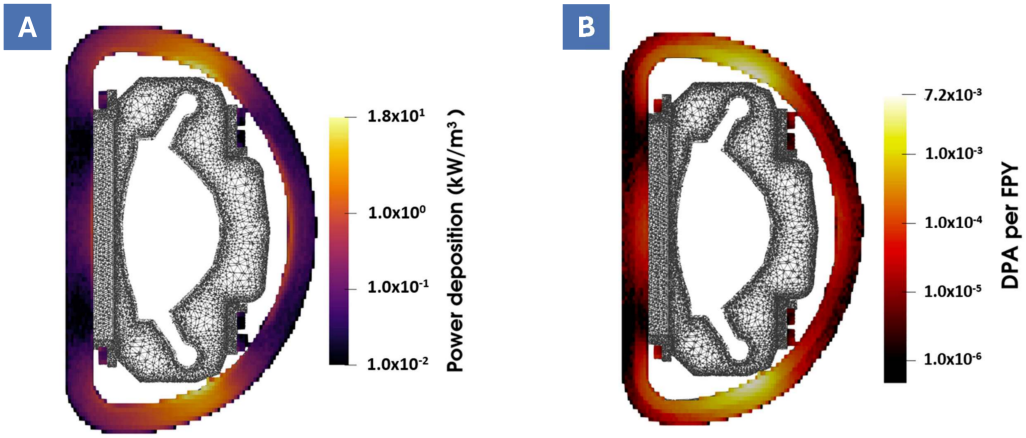

Fig. 3.8 Power deposition (A) and Radiation damage dose (B) over the full reactor, considering the best shielding option, HfH_2. Adapted from (11).

and displacement damage reduction, followed by WC and WB. These three top-performing compounds are all documented and employed in nuclear and industrial contexts. Their practical viability is therefore not merely hypothetical: they are not expected to pose exceptional safety concerns nor to entail prohibitive costs, although a comprehensive engineering assessment lies beyond the scope of this work.

It should be noted, however, that the results discussed so far are based on quantities integrated over relatively large coil regions. As a consequence, localized irradiation hot spots may be partially masked by spatial averaging. To address this limitation, the integral neutron flux was mapped directly onto the tetrahedral mesh used to import the reactor model, enabling a spatially resolved characterization of the radiation environment throughout the magnetic system. This mapping procedure was carried out for all nine candidate shielding materials; however, for clarity, only the results corresponding to the best-performing option, HfH_2, are shown in the figure 3.4.

Consistently with the indications obtained from the cable-scale and integral analysis, the neutron shield results in an average suppression of the neutron flux on the inboard segment of the TFC by several orders of magnitude, down to average values of the order of 10^9 ncm^{-2}s^{-1}. Nevertheless, when the neutron flux is mapped over the full reactor geometry, a markedly inhomogeneous spatial distribution emerges, with highly localized hot spots exceeding 10^{10} ncm^{-2}s^{-1} at the midplane.

Moreover, the reduced blanket thickness above and below the divertor regions shifts the locations of maximum irradiation, giving rise to two distinct regions characterized by undershielded neutron fluxes of the order of 10^{11} ncm^{-2}s^{-1}. These features are not apparent when considering region-averaged quantities alone and highlight the dominant role of geometrical constraints in shaping the local radiation environment experienced by the magnets.

These local hot spots, which become apparent only through a detailed spatial mapping of the reactor, are clearly reflected in the power deposition distribution. While the power density remains within acceptable limits over the whole magnetic system, pronounced local maxima are observed (Fig. 3.8A). It is worth noting that, in the current design of the SPARC toroidal-field model coil, the helium outlet is located in proximity to one of these high heat-load regions, coinciding with the location where the quench was initiated during the experimental test campaign (180).

The impact of irradiation hot spots becomes even more critical when considering displacement damage. The average damage level accumulated over the entire toroidal-field coil amounts to approximately 0.64 mdpa per full-power year, which would correspond to an estimated lifetime of about 6.25 years when adopting 4 mdpa as an approximate degradation threshold. However, the effective lifetime is dictated by the most severely irradiated regions: near the divertor, local damage levels reach up to 7.2 mdpa per full-power year, implying a lifetime shorter than seven months (Fig. 3.8B).

In contrast, the poloidal-field coils appear comparatively well protected in the present configuration. Owing to their smaller dimensions, the average and peak displacement damage values within each PFC are similar, and no pronounced local hot spots are observed.

As discussed above, the assessment of magnet lifetime has so far relied on a simplified criterion based on a damage level of approximately 4 mdpa, commonly adopted as a rule of thumb for the onset of superconducting property degradation. However, these experimental results are largely based on fission neutron spectra, which can differ substantially from the fusion-relevant spectra considered here. Moreover, the use of different shielding materials can introduce additional spectral modifications even within fusion environments.

Given the large variability in superconducting degradation observed at comparable displacement doses, there is no guarantee that identical dpa values correspond

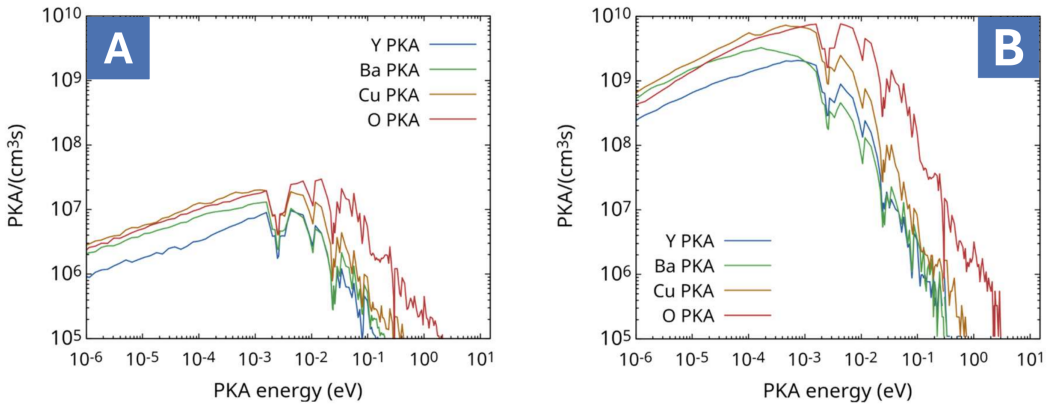

Fig. 3.9 PKA spectra at the TFC inboard midplane, for the best (A, HfH_2) and for the worst (B, HfV_2) shielding solution. Adapted from (11).

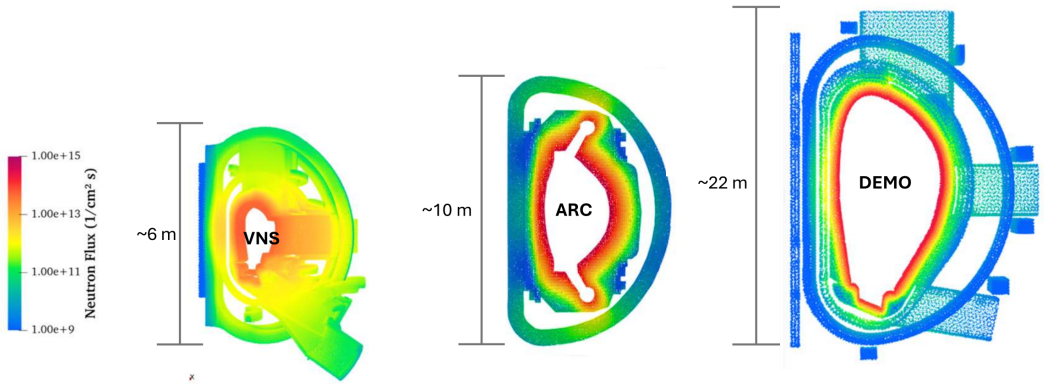

Fig. 3.10 Integral neutron flux on the VNS, ARC and DEMO. The relative errors on the magnets are within 5%

to similar defect populations or damage mechanisms. In order to overcome this limitation, PKAs spectra were extracted at TFC inboard as shown in Fig. 3.9 for the best and worst shielding solution. These spectra provide the input required for the atomistic analyses presented in the following chapters, where radiation damage is characterised beyond the dpa approximation.

3.4 Comparative assessment of radiation environments in ARC, DEMO and VNS

Before proceeding with the multiscale approach and the atomistic analysis, it is useful to compare the radiation environment identified for ARC with that expected in two machines at a more advanced level of design maturity, namely DEMO and VNS. The different sizes of the three devices play a major role in neutron propagation: the minor radius of DEMO is approximately six times larger than that of VNS and almost three times larger than that of ARC (see Fig. 3.10).

In DEMO, the magnetic system is effectively shielded, with neutron flux values of the order of 10^9 n cm^{-2} s^{-1} almost everywhere, except at the inboard midplane of the toroidal-field coils. In contrast, in VNS the neutron flux exceeds 10^{12} n cm^{-2} s^{-1} in the toroidal-field coils and, in particular, in the poloidal-field coils. In ARC, the neutron flux distribution is particularly heterogeneous, with irradiation levels lying between those of DEMO and VNS depending on the location.

In addition to machine size, specific design choices have a substantial impact on the location of the most heavily irradiated regions. In ARC, the presence of a dedicated HfH_2 shielding layer appears particularly beneficial, strongly reducing the neutron flux at the inboard midplane to levels comparable to those predicted for DEMO. Moreover, the large thickness of the immersion blanket significantly mitigates the neutron flux at the outboard midplane of the toroidal-field coils, while the dedicated shields provide additional protection for the PFCs. Conversely, the double-null plasma configuration, combined with the reduced amount of material surrounding the divertor regions, leads to localized neutron-flux hot-spots near the upper and lower divertors. Although detailed geometrical models of the ARC divertor are not currently available, these results indicate that careful consideration of divertor-region shielding will be required to ensure adequate protection of the magnetic system.

In VNS, the most heavily irradiated region of the toroidal-field coils is the inboard midplane, followed by the outboard midplane, due to the presence of a large equatorial port, which allows neutron streaming despite the presence of a port plug. In addition, the location of the poloidal-field coils inside the vacuum vessel, without dedicated shielding, results in particularly high neutron fluxes for these components.

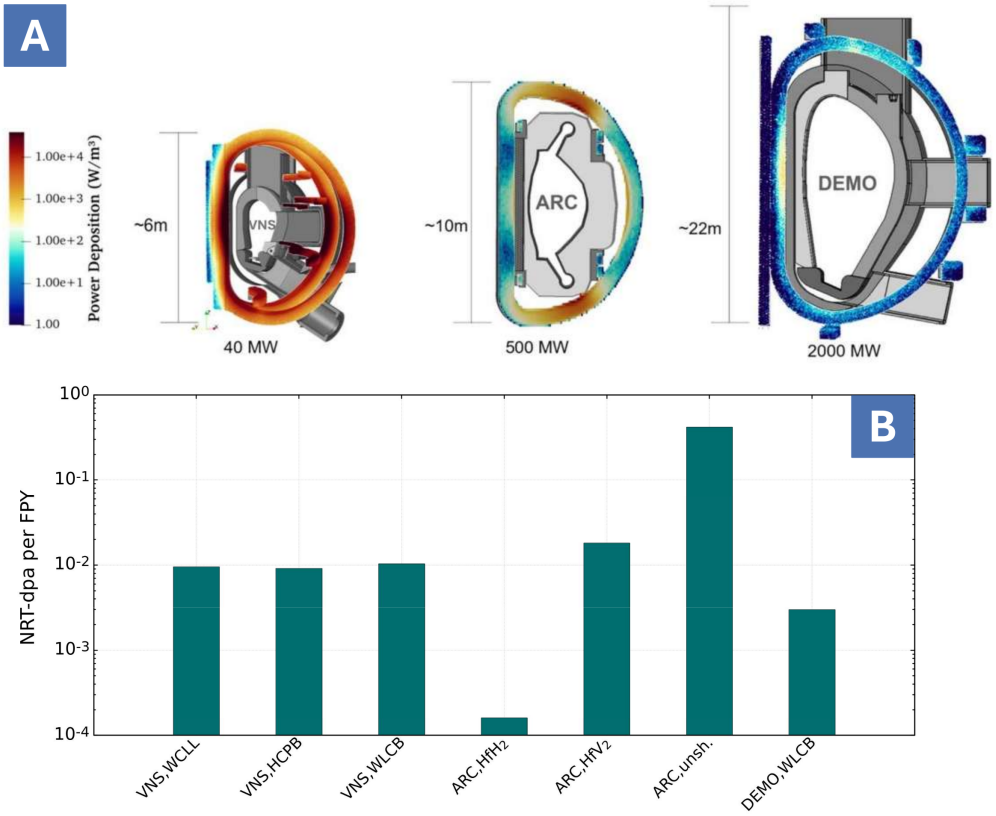

Fig. 3.11 A) Volumetric power deposition in VNS, ARC (with HfH_2 shielding) and DEMO. The relative errors on the magnets are within 5% B) NRT-dpa per full-power year at the inboard midplane of the toroidal-field coils for VNS, DEMO and ARC, considering the unshielded case and the worst and best shielding configurations.

The spatial distribution of power deposition follows the same overall trends identified for the neutron flux (see Fig. 3.11A). In VNS, the midplane of the toroidal-field coils and the poloidal-field coils located close to the equatorial port experience power-deposition levels approximately two orders of magnitude higher than those predicted for ARC and DEMO. Between the latter two devices, DEMO exhibits a higher hot-spot at the inboard midplane, although the rest of the magnetic system remains below about 50 W/m^3.

Finally, the lattice damage at the inboard midplane, expressed in terms of NRT-dpa per full-power year, is compared for VNS (considering three different breeding-blanket concepts), ARC (for the best shielding configuration, the worst shielding configuration, and the unshielded case, the latter derived from the cable irradiation study), and DEMO (Fig. 3.11B). In the absence of dedicated shielding, ARC experiences radiation damage at least one order of magnitude higher than both VNS and DEMO. However, even the least effective shielding option considered for ARC reduces the damage to a level comparable to that of VNS. DEMO appears, in this comparison, as the best-protected configuration. The best shielding option tested for ARC further reduces the damage at the inboard midplane by nearly two orders of magnitude with respect to VNS and by approximately one order of magnitude with respect to DEMO.

3.5 Multiscale damage assessment: coupling Monte Carlo transport with atomistic descriptors

As described in the Methods, the combined use of Molecular Dynamics and Binary Collision Approximation enables the direct investigation and analysis of a statistically relevant number of collision cascades over the full energy range relevant for radiation damage in YBCO under fusion conditions, spanning from a few eV up to 3 MeV. The resulting dataset quantifies a set of damage descriptors beyond the dpa approximation, including the defect yield (Fig. 3.12, upper panel), the damaged volume (Fig. 3.12, lower panel), and clustering statistics (Fig. 3.13), for each PKA species across the entire recoil-energy spectrum.

The sublinear increase in defect production with increasing recoil energy reflects a progressive reduction in damage efficiency. This behaviour is rooted in the energy

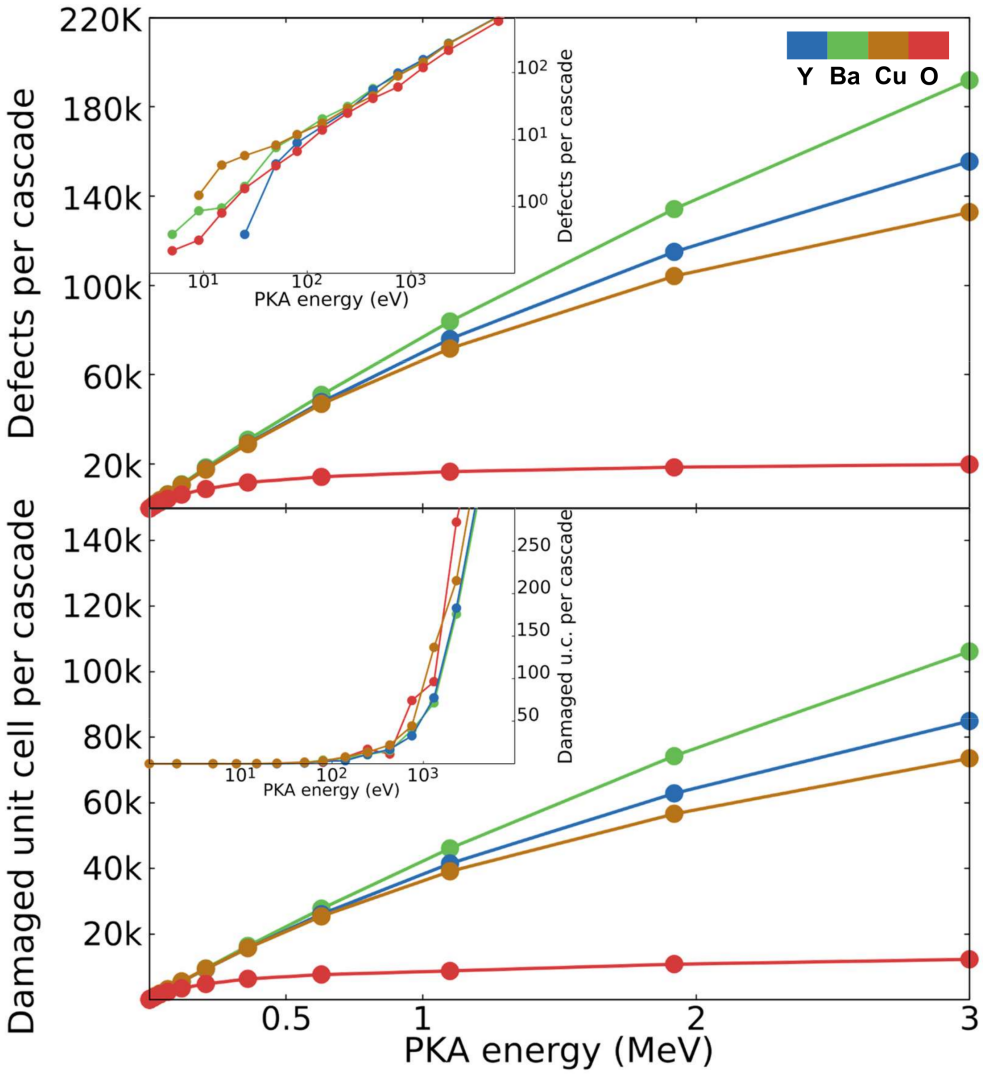

Fig. 3.12 Defect yield (top) and damaged volume in terms of unit cells (bottom) per collision cascade as a function of the PKA energy for the different atomic species at 20 K. Adapted from (8).

partitioning between nuclear and electronic stopping channels: only the fraction of the PKA kinetic energy deposited through nuclear collisions, the damage energy (E), contributes to lattice disorder, while the remainder is dissipated via electronic excitations without generating permanent defects (13). To illustrate this partitioning quantitatively, the damage energy (E) = (E)·E, where (E) is the fraction of kinetic energy deposited into nuclear collisions, was evaluated for each PKA species alongside the nuclear stopping power, computed using the ZBL formulation (169) with com-

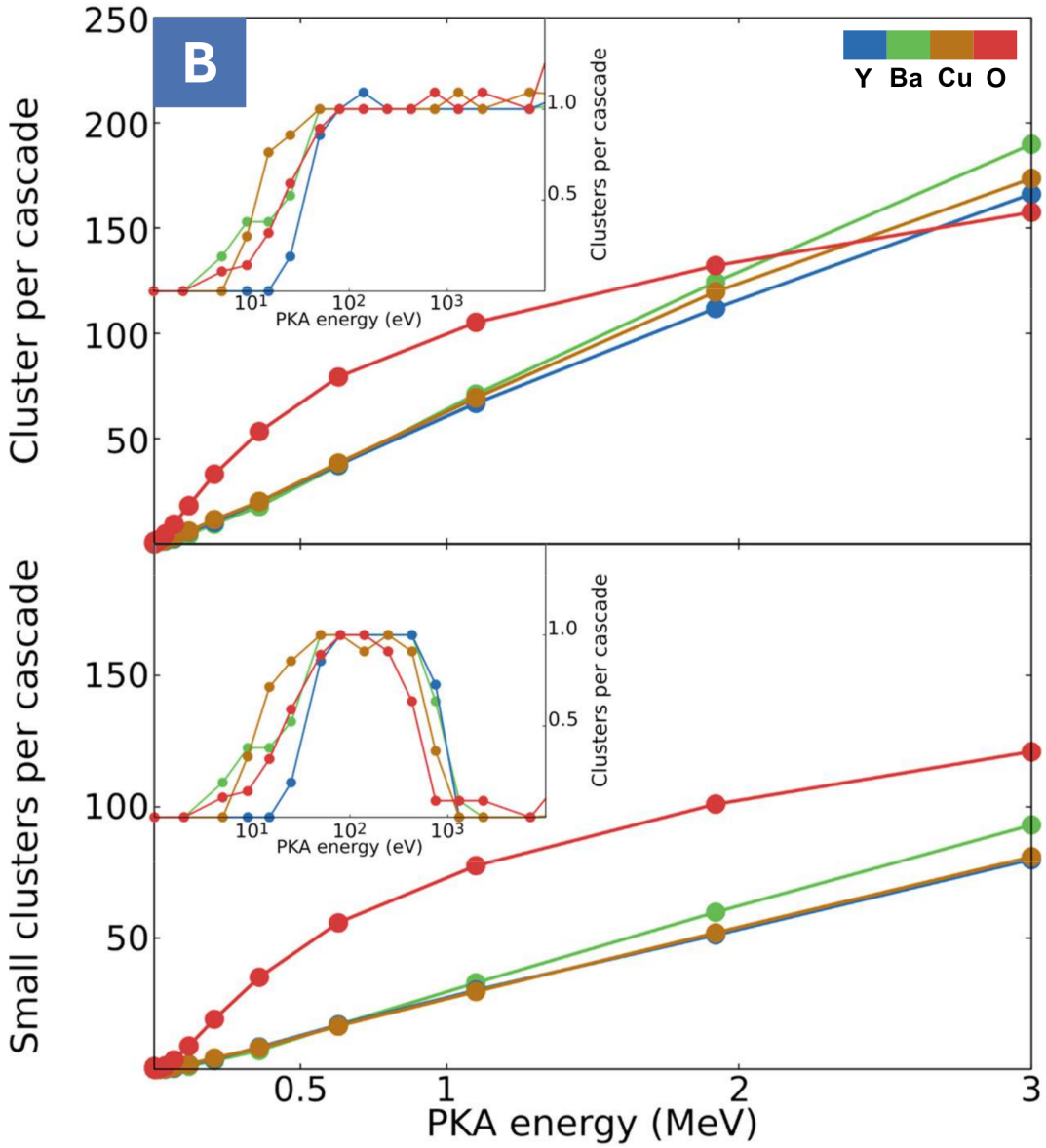

Fig. 3.13 Number of defect clusters (top) and of small clusters (bottom) per cascade as a function of the PKA energy for the different atomic species at 20 K. Adapted from (8).

positional averages Z_2=22.6 and M_2=51.2 for the YBCO target, and the electronic stopping power as provided by SRIM (Fig. 3.14). The relative weight of nuclear and electronic contributions is strongly species-dependent and largely determines the observed differences in damage descriptors across the recoil-energy spectrum. For heavy species such as Y, Ba and Cu, nuclear stopping remains comparable to

electronic stopping throughout the energy range considered, so that (E) increases quasi-linearly with energy, sustaining the production of large, dense cascades. For oxygen, the situation is fundamentally different: nuclear stopping reaches its maximum near 10 keV and decreases rapidly thereafter, becoming negligible above a few hundred keV. As a result, the damage energy saturates at high recoil energies, directly explaining the plateau in defect yield and damaged volume observed for O PKAs. The species dependence extends beyond total defect counts and manifests clearly in the spatial organisation of the damage. For heavy PKAs, the combination of high nuclear stopping and short internuclear distances promotes cascade densification and thermal spike formation, leading to compact damage regions with a tendency towards defect agglomeration into larger clusters. For oxygen recoils, the lower nuclear stopping cross section implies longer mean free paths between successive displacement events, resulting in spatially dilute cascades where individual defects or small groups are produced in isolation. This geometrical dilution suppresses cluster growth, so that O-induced cascades are characterised by a higher density of small, scattered clusters, a morphological signature that persists across most of the energy range despite the lower absolute defect count.

Having established the atomistic response of YBCO to individual recoil events, the framework can now be applied to realistic irradiation scenarios in order to quantify the resulting damage landscape. Before extending the analysis to the reactor scale, it is instructive to examine the defect structures produced by electron and fission-neutron irradiation, each corresponding to an accumulated dose of 1 mdpa, as discussed in the Introduction.

This comparison allows, on the one hand, to test the capability of the method to capture the different defect landscapes produced by markedly different irradiation scenarios at the same dose, thereby overcoming the limitations of the NRT-dpa approximation. On the other hand, it provides a reference set of damage indicators derived from a well-controlled experimental irradiation layout, which can be used to qualify the damage regime encountered in the subsequent reactor-scale analyses.

Although the two irradiation scenarios correspond to the same nominal dose, the atomistic descriptors extracted from the MD–BCA dataset reveal markedly different defect landscapes, as summarised in Table 3.2. The total number of Frenkel pairs in the two cases remains comparable, in agreement with the identical dpa values, while the spatial organisation and morphology of the resulting defects differ substantially.

Quantity	Neutron irradiation	Electron irradiation
Nominal dose (NRT-mdpa)	1	1
Frenkel pair density (cm³)	5.48×10^{20}	2.45×10^{20}
Cluster density (cm³)	1.44×10^{18}	3.45×10^{19}
Small-cluster fraction (%)	53	99
Mean defects per cluster	405	7
Damaged volume fraction (%)	0.98	1.22

Table 3.2 Atomistic damage indicators predicted for YBCO under irradiation conditions corresponding to the same nominal dose of 1 mdpa. The reported values are obtained by coupling the MD–BCA dataset with the appropriate PKA energy distributions. Although the accumulated dose is identical, neutron irradiation is characterised by the formation of fewer, larger and more compact defect clusters, while electron irradiation results in a higher number of small, spatially dispersed defects.

Electron irradiation, dominated by low-energy oxygen recoils (inset of Fig. 1.1A), leads to the formation of a large number of small, spatially isolated clusters. In contrast, neutron irradiation generates a limited number of highly energetic PKAs, producing extended collision cascades and compact regions of intense damage involving hundreds of Frenkel pairs.

This result, fully consistent with well-established experimental observations (113), confirms that the atomistic framework captures fundamental differences in defect production mechanisms associated with different irradiation types, providing information that cannot be accessed through conventional dpa metrics alone. Moreover, the neutron-induced damage characteristics identified here can be adopted as a reference for interpreting the irradiation conditions encountered in the reactor-scale analysis, thereby avoiding the risk of misleading comparisons based solely on integral dose values.

Building on a consistent workflow and on the multi-dimensional reference description of neutron-induced damage established at the atomistic level, the method is now applied to the irradiation conditions predicted for the ARC-like reactor. The inboard segment of the toroidal-field coils was selected for this analysis, as it was identified in the previous sections as the region requiring protection at the earliest stage.

The primary knock-on atom spectra computed for this location were therefore convolved with the atomistic damage dataset, yielding the damage indicators reported in Table 3.3 for the different shielding materials.

Adopted shield	Defect density	Cluster density	Small-clu. fract. (%)	Vol. damage (% s^{-1})	Defects/cluster
Hf_1V_2	1.10×10^{14}	4.55×10^{11}	49.0	1.23×10^{-6}	2.41×10^{2}
V_1B_1	3.27×10^{13}	8.88×10^{10}	44.6	3.31×10^{-7}	3.69×10^{2}
GdH_3	2.37×10^{13}	5.94×10^{10}	49.2	2.29×10^{-7}	3.98×10^{2}
ZrH_2	1.72×10^{13}	4.30×10^{10}	48.6	1.67×10^{-7}	4.01×10^{2}
W_1B_4	1.78×10^{13}	4.62×10^{10}	44.8	1.77×10^{-7}	3.85×10^{2}
Ti_1H_2	1.44×10^{13}	3.64×10^{10}	49.1	1.40×10^{-7}	3.97×10^{2}
W_1C_1	2.84×10^{12}	1.28×10^{10}	57.4	3.05×10^{-8}	2.23×10^{2}
W_1B_1	2.58×10^{12}	7.90×10^{9}	45.4	2.69×10^{-8}	3.27×10^{2}
Hf_1H_2	1.87×10^{12}	4.88×10^{9}	49.6	1.82×10^{-8}	3.82×10^{2}

Table 3.3 Atomistic damage indicators in YBCO for the nine investigated shielding configurations.

Across the investigated compounds, the predicted irradiation response shows substantial variations in the overall rate of damage production, consistent with trends inferred from the corresponding dpa values. Defect density, cluster density, and damaged volume fraction per unit time span nearly two orders of magnitude across the materials considered, highlighting a strong shielding dependence in damage generation efficiency.

Alongside these large quantitative differences, descriptors associated with the average defect morphology display a comparatively limited spread among most shielding materials. In particular, the mean number of defects per cluster varies within less than a factor of two, and the fraction of small clusters for almost all shielding options lies between 44 and 49%. In these cases, the shielding materials appear to primarily affect the intensity of damage production, while keeping the characteristic defect morphology largely similar.

An exception is represented by WC, which exhibits both the highest fraction of small clusters (57 %) and the lowest mean number of defects per cluster, consistent with a more spatially dispersed damage morphology. Such a defect configuration may be associated with a faster degradation of the critical temperature and is therefore considered unfavourable within the present comparison.

Finally, the evaluated atomistic damage indicators can be used to estimate proxy times required to reach the reference damage levels associated with the fission-neutron irradiation condition at 4 mdpa. The ranking across the shielding options is

consistent for all indicators, with HfV_2 yielding the shortest proxy times and HfH_2 the longest.

When considering the defect and cluster density indicators, the materials can be grouped into three distinct performance classes. A first group, comprising HfV_2, VB and GdH_3, yields proxy times of approximately 2–3 years. A second group, including ZrH_2, WB and TiH_2, reaches about 5 years, while a third group of more effective shields, namely WC, WB and HfH_2, exceeds 10 years.

For WC and WB, the difference between the proxy times derived from cluster density and defect density becomes particularly pronounced, with a shorter time required to reproduce the reference cluster density than the corresponding defect density. This behaviour is consistent with a more spatially dispersed damage morphology. In this context, information on the fraction of small clusters produced suggests preferring WB over WC, despite their similar performance in terms of the overall number of clusters and defects produced: for WC, indeed, 57% of the defects are small, compared to only 45% for WB.

In all cases, the damaged-volume indicator yields systematically shorter proxy times. This trend points to a larger spatial footprint of damage per produced defect under fusion-relevant recoil spectra, consistent with the expectation that higher-energy cascades extend over larger volumes even when the average number of defects per cluster remains comparable. From an operational perspective, this result suggests that the evolution of critical properties under fusion irradiation may differ from what is inferred from fission-based experiments, and that further investigation and characterisation of irradiation-induced defects should also consider their potential role as pinning centres.

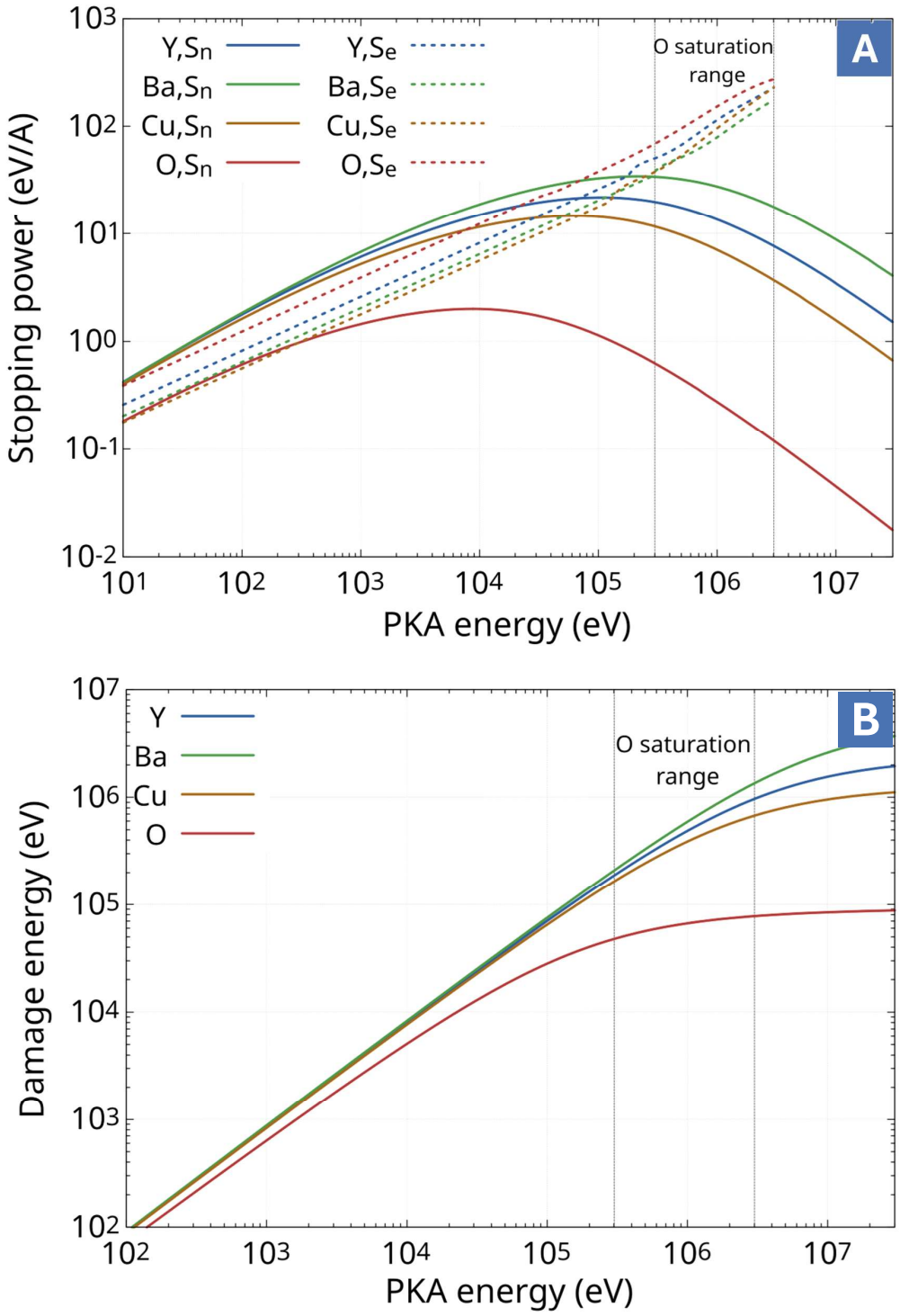

Fig. 3.14 A) Nuclear and electronic stopping powers for the four PKA species in YBCO (Y, Ba, Cu, O) as a function of PKA energy, computed with the ZBL formulation, assuming average target properties. B) Damage energy (E) as a function of PKA energy for the four species in YBCO, computed using the Lindhard partitioning function as parametrised by Norgett et al (13), assuming average target properties. Adapted from (8).

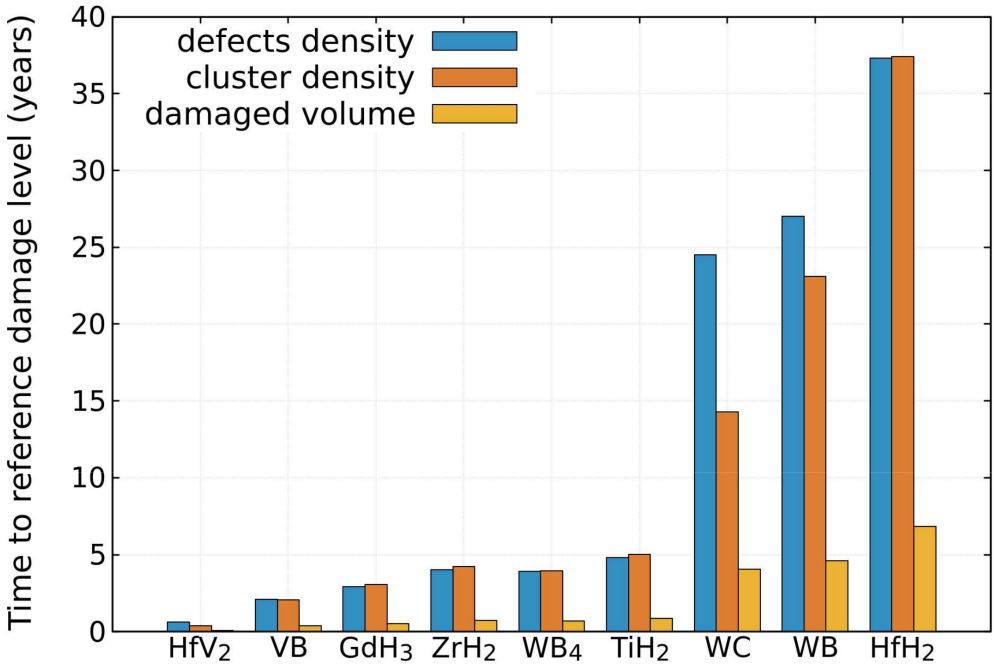

Fig. 3.15 Time (in years) to reach the reference damage level suffered by YBCO under fission neutron irradiation at a dose of 4 mdpa, in terms of defect density, cluster density and damaged volume fraction, for the TFC inboard protected by the 9 candidate shields.

Chapter 4

Conclusions

In conclusion, this thesis addressed the problem of radiation damage in REBCO superconductors with a particular focus on compact fusion reactors, starting from the identification of the limitations of conventional dose-based metrics when applied to different irradiation regimes. While the dpa framework provides a convenient integral measure of damage, it does not capture the diversity of defect landscapes generated by markedly different irradiation conditions, nor does it account for the spatial organisation and morphological features of irradiation-induced defects, which are known to be critical for superconducting performance. In particular, electron and fission-neutron irradiation at the same accumulated dpa were shown to produce markedly different degradation behaviours.

Monte Carlo simulations were employed to characterise the radiation environment at progressively increasing levels of complexity, from simplified reactor-core models to a complete ARC-like reactor geometry including shielding and magnetic systems. The proposed MC workflow (covering code selection, nuclear data libraries, and domain reduction strategies) was developed and systematically tested on the reactor-core model, providing a solid basis for subsequent calculations. The most neutronically loaded position around the core was identified, and the corresponding neutron spectrum was evaluated.

Using this spectrum as boundary input, simulations on a representative HTS cable demonstrated the necessity of dedicated neutron shielding and enabled a first estimate of a suitable shield thickness. These simulations also showed the capability

of PHITS to generate spatially resolved outputs suitable for coupling with finite-element thermal analyses.

Building on these results, the ARC-like reactor model was developed and extended to include the full magnetic system and dedicated shielding elements, and nine different shielding materials were investigated. The inclusion of discrete shielding elements was shown to reduce average irradiation levels on the magnets to values compatible with operation. At the same time, detailed three-dimensional mapping revealed strong spatial inhomogeneities and local hot spots that are not apparent from integrated quantities alone.

Finally, the radiation environment expected on the ARC-like magnetic system was compared with that computed for two designs characterized by a more advanced level of design maturity and different design philosophies, namely VNS and DEMO. The results show a clear dependence of the overall harshness of the radiation environment on the machine size, with VNS emerging as the most critical configuration among the three concepts considered. At the same time, the machine size was shown not to be the only driver of radiation damage, with the location and intensity of neutron flux and power deposition hot-spots being strongly influenced by specific design features, such as port structures in the case of VNS and divertor regions for ARC. In this framework, the adoption of dedicated neutron shielding solutions appears particularly beneficial for ARC, being able to substantially reduce, despite the compact size, the neutron flux and power deposition at the inboard TFC to levels comparable with those of DEMO.

To overcome the limitations of the dpa metric, BCA calculations were coupled with MD simulations, allowing a statistically relevant number of collision cascades to be analysed over the full energy range relevant for fusion applications, from a few eV up to 3 MeV. This approach yielded a set of atomistic damage descriptors, including defect yield, damaged volume, and defect clustering statistics. When applied to markedly different irradiation scenarios by convolution with the corresponding PKA spectra, specifically the electron and fission neutron irradiation discussed above, these indicators successfully captured differences in defect morphology and spatial distribution. This result is of general relevance, as it provides a robust interpretative framework for existing irradiation experiments and a predictive basis for the design of future studies.

When applied to the reactor case, the atomistic damage indicators show that, for most of the investigated shielding materials, the primary effect is a modulation of the overall intensity of damage production, while the characteristic defect morphology at the examined magnet location remains largely similar. Nevertheless, non-negligible differences are observed among specific materials. In particular, WC exhibits a systematically higher fraction of small defect clusters compared to the other shielding options, indicating a tendency to promote a more finely dispersed damage state.

Finally, atomistic damage indicators corresponding to YBCO irradiated by fission neutrons to a dose of 4 mdpa were adopted as a reference to estimate proxy degradation times for the inboard segment of the ARC-like toroidal-field coils. Among the investigated materials, HfH_2 emerged as the most effective shielding option. WC was shown to be able to guarantee, with the adopted thickness, more than 10 years of operation before reaching the reference damage level. However, when combined with its less favourable performance in terms of small-defect production, this result suggests that WC may not represent the most suitable option for the protection of YBCO in a fusion neutron environment. These observations highlight the relevance of an atomistic-level description of radiation damage for the assessment of shielding materials, since differences in defect production mechanisms may not be captured by metrics based only on damage intensity.

While proxy times derived from defect-yield and cluster-density indicators are generally similar across the tested materials, proxy times estimated using the damaged-volume indicator are systematically shorter. This behaviour points to a larger spatial footprint of damage under fusion-relevant recoil spectra compared to fission neutrons, suggesting that operational degradation under fusion irradiation may evolve differently from what is inferred from fission-based experiments, and underscoring the importance of considering defect morphology and spatial extent in addition to integral dose metrics.

Overall, this work provides a physically informed, multiscale description of radiation damage suitable for the reliable assessment of HTS magnets in fusion reactors. The proposed framework enables quantitative comparisons between shielding strategies, offers insight into the nature of the underlying damage regimes, and establishes a pathway toward bridging neutron transport simulations with atomistic damage modelling. Future developments should focus on targeted experimental validation

under fusion-relevant spectra and on the explicit coupling between atomistic damage descriptors and macroscopic superconducting properties.

References

[1] S. E. Wurzel and S. C. Hsu, "Progress toward fusion energy breakeven and gain as measured against the lawson criterion," *Phys. Plasmas*, vol. 29, no. 6, 2022.

[2] M. B. Maple, "High-temperature superconductivity," *J. Magn. Magn. Mater.*, vol. 177, pp. 18–30, 1998.

[3] A. Gurevich, "To use or not to use cool superconductors?" *Nat. Mater.*, vol. 10, no. 4, pp. 255–259, 2011.

[4] M. Búran *et al.*, "Impact of a REBCO coated conductor stabilization layer on the fault current limiting functionality," *Supercond. Sci. Technol.*, vol. 32, no. 9, p. 095008, 2019.

[5] F. M. Sauerzopf *et al.*, "Analysis of pinning effects in $YBa_2Cu_3O_{7-\delta}$ single crystals after fast neutron irradiation," *Phys. Rev. B Condens. Matter*, vol. 51, pp. 6002–6012, 1995.

[6] L. Civale *et al.*, "Defect independence of the irreversibility line in proton-irradiated Y-Ba-Cu-O crystals," *Phys. Rev. Lett.*, vol. 65, pp. 1164–1167, 1990.

[7] A. L. Solovjov *et al.*, "Influence of strong electron irradiation on fluctuation conductivity and pseudogap in $YBa_2Cu_3O_{7-\delta}$ single crystals," *Phys. Rev. B Condens. Matter*, vol. 111, p. 174508, 2025.

[8] F. Ledda *et al.*, "Beyond DPA: An atomistic framework for a quantitative description of radiation damage in $YBa_2Cu_3O_7$," *arXiv preprint arXiv:2512.16249*, 2025.

[9] ——, "3D neutronic analysis on compact fusion reactors: PHITS-OpenMC cross-comparison," *Fusion Eng. Des.*, vol. 202, p. 114323, 2024.

[10] ——, "3D neutronic and secondary particles analysis on YBCO tapes for compact fusion reactors," *IEEE Trans. Appl. Supercond*, vol. 32, no. 9, 2022.

[11] D. Torsello *et al.*, "Radiation environment and damage of HTS magnets in an ARC-like reactor," *IEEE Trans. Appl. Supercond.*, vol. 35, no. 5, pp. 1–6, 2024.

[12] T. S. Pugacheva *et al.*, "Effects of cascade mixing, sputtering and diffusion by high dose light ion irradiation of boron nitride," *Nucl. Instrum. Methods Phys. Res. Sect. B*, vol. 141, pp. 99–104, 1998.

[13] M. J. Norgett *et al.*, "A proposed method of calculating displacement dose rates," *Nucl. Eng. Des.*, vol. 33, no. 1, pp. 50–54, 1975.

[14] B. N. Sorbom *et al.*, "ARC: A compact, high-field, fusion nuclear science facility and demonstration power plant with demountable magnets," *Fusion Eng. Des.*, vol. 100, pp. 378–405, 2015.

[15] V. Smil, "Energy in the twentieth century: Resources, conversions, costs, uses, and consequences," *Annu. Rev. Energy Env.*, vol. 25, no. 1, pp. 21–51, 2000.

[16] G. T. Reader, "Energy, renewables alone?" *Sustaining Resources for Tomorrow*, pp. 1–45, 2020.

[17] M. Balat, "The role of nuclear power in global electricity generation," *Energy Sources, Part B*, vol. 2, no. 4, pp. 381–390, 2007.

[18] P. Slovic, "The perception gap: Radiation and risk," *Bull. At. Sci.*, vol. 68, no. 3, pp. 67–75, 2012.

[19] R. d. Atkinson and F. G. Houtermans, "Zur frage der aufbaumöglichkeit der elemente in sternen," *Zeitschrift für Physik*, vol. 54, pp. 656–665, 1929.

[20] H. A. Bethe, "Energy production in stars," *Phys. Rev.*, vol. 55, pp. 434–456, 1939.

[21] S. Banacloche *et al.*, "Socioeconomic and environmental impacts of bringing the sun to earth: A sustainability analysis of a fusion power plant deployment," *Energy*, vol. 209, p. 118460, 2020.

[22] G. J. Butterworth, "Low activation structural materials for fusion," *Fusion Eng. Des.*, vol. 11, no. 1-2, pp. 231–244, 1989.

[23] J. Wesson and D. J. Campbell, *Tokamaks*. Oxford University Press, 2011, vol. 149.

[24] J. P. Freidberg, *Plasma Physics and Fusion Energy*. Cambridge: Cambridge University Press, 2007.

[25] S. C. Prager, "Nuclear fusion power–an overview of history, present and future," *Int. J. Adv. Netw. Monit. Controls*, vol. 4, no. 4, pp. 1–10, 2020.

[26] S. Meschini *et al.*, "Review of commercial nuclear fusion projects," *Front. Energy Res.*, vol. 11, 2023.

[27] T. H. Johnson, "Inertial confinement fusion: Review and perspective," *Proc. IEEE*, vol. 72, no. 5, pp. 548–594, 1984.

[28] A. B. Zylstra *et al.*, "Experimental achievement and signatures of ignition at the national ignition facility," *Phys. Rev. E*, vol. 106, no. 6, p. 065202, 2022.

[29] R. Boni and J. D. Zuegel, "Status and prospects for inertial fusion energy via lasers," in *Proceedings of SPIE*, vol. 13358. SPIE, 2024, p. 1335802.

[30] H. Alfvén, *Cosmical Electrodynamics*, 2nd ed. Oxford University Press, 1963.

[31] J. Ongena *et al.*, "Magnetic-confinement fusion," *Nat. Phys.*, vol. 12, no. 5, pp. 398–410, 2016.

[32] A. A. Garren *et al.*, "Individual particle motion and the effect of scattering in an axially symmetric magnetic field," Lawrence Berkeley National Laboratory, Technical Report, 1958.

[33] T. K. Fowler and M. Rankin, "Fusion energy balance in mirror machines," *J. Nucl. Energy C*, vol. 8, no. 2, p. 121, 1966.

[34] F. F. Chen *et al.*, *Introduction to Plasma Physics and Controlled Fusion*. Springer, 1984.

[35] A. V. Burdakov *et al.*, "Modern magnetic mirrors and their fusion prospects," *Plasma Phys. Contr. F.*, vol. 52, no. 12, p. 124026, 2010.

[36] D. J. Griffiths, *Introduction to Electrodynamics*. Cambridge University Press, 2023.

[37] L. Spitzer Jr, "Project matterhorn report," PM-S-1 NYO-993, Princeton University, Tech. Rep., 1951.

[38] L. Spitzer, "The stellarator concept," *Phys. Fluids*, vol. 1, no. 4, p. 253, 1958.

[39] F. Warmer *et al.*, "Stellarator fusion power plants," in *Magnetic Fusion Energy*. Elsevier, 2016, pp. 577–598.

[40] J. C. Hosea *et al.*, "Properties of magnetic surfaces in the model c stellarator," *Plasma Phys.*, vol. 13, no. 5, p. 365, 1971.

[41] A. Liyoshi *et al.*, "Confinement of a currentless plasma in the Heliotron-E," *Phys. Rev. Lett.*, vol. 48, no. 11, p. 745, 1982.

[42] G. Grieger *et al.*, "Confinement of stellarator plasmas with neutral beam and rf heating in W VII-A," *Plasma Phys. Contr. F.*, vol. 28, no. 1A, p. 43, 1986.

[43] S. V. Mirnov, "Tokamak evolution and view to future," *Nucl. Fusion*, vol. 59, no. 1, p. 015001, 2018.

[44] B. Lehnert, "Half a century of fusion research towards ITER," *Phys. Scripta*, vol. 87, no. 1, p. 018201, 2012.

[45] T. H. Stix, "Highlights in early stellarator research at princeton," *J. Plasma Fusion Res. SERIES*, vol. 1, no. 3, 1998.

[46] T. F. R. Group *et al.*, "TFR, the tokamak of Fontenay-Aux-Roses," *Nucl. Fusion*, vol. 25, no. 9, p. 1025, 1985.

[47] P. Rutherford, "The tokamak: 1955–80," *Nucl. Fusion*, vol. 20, no. 9, p. 1086, 1980.

[48] H. Zohm, "On the size of tokamak fusion power plants," *Philos. Trans. R. Soc. Math. Phys. Eng. Sci.*, vol. 377, no. 2141, 2019.

[49] K. Ikeda, "ITER on the road to fusion energy," *Nucl. Fusion*, vol. 50, no. 1, p. 014002, 2009.

[50] P. H. Rebut, "The JET preliminary tritium experiment," *Plasma Phys. Contr. F.*, vol. 34, no. 13, p. 1749, 1992.

[51] M. Keilhacker *et al.*, "High fusion performance from deuterium-tritium plasmas in JET," *Nucl. Fusion*, vol. 39, no. 2, p. 209, 1999.

[52] H. Zushi *et al.*, "Steady-state tokamak operation, ITB transition and sustainment and ECCD experiments in TRIAM-1M," *Nucl. Fusion*, vol. 45, no. 10, p. S142, 2005.

[53] Y. Shimomura, "Overview of international thermonuclear experimental reactor (ITER) engineering design activities," *Phys. Plasmas*, vol. 1, no. 5, pp. 1612–1618, 1994.

[54] L. Giancarli *et al.*, "Overview of EU activities on DEMO liquid metal breeder blankets," *Fusion Eng. Des.*, vol. 27, pp. 337–352, 1995.

[55] S. Ciattaglia *et al.*, "The european DEMO fusion reactor: Design status and challenges from balance of plant point of view," in *2017 IEEE International Conference on Environment and Electrical Engineering and 2017 IEEE Industrial and Commercial Power Systems Europe (EEEIC/I&CPS Europe)*. IEEE, 2017, pp. 1–6.

[56] G. Zhou *et al.*, "The european DEMO helium cooled pebble bed breeding blanket: Design status at the conclusion of the pre-concept design phase," *Energies*, vol. 16, no. 14, p. 5377, 2023.

[57] J. Aubert *et al.*, "Development of the water cooled lithium lead blanket for DEMO," *Fusion Eng. Des.*, vol. 89, no. 7-8, pp. 1386–1391, 2014.

[58] G. Zhou *et al.*, "A water cooled lead ceramic breeder blanket for european DEMO," *Fusion Eng. Des.*, vol. 168, p. 112397, 2021.

[59] L. Zani *et al.*, "Overview of progress on the EU DEMO reactor magnet system design," *IEEE Trans. Appl. Supercond.*, vol. 26, no. 4, pp. 1–5, 2016.

[60] P. Bruzzone, "Superconductivity and fusion energy—the inseparable companions," *Supercond. Sci. Technol.*, vol. 28, no. 2, p. 024001, 2014.

[61] G. Federici *et al.*, "Overview of the DEMO staged design approach in europe," *Nucl. Fusion*, vol. 59, no. 6, p. 066013, 2019.

[62] M. Banks, "ITER hit by new decade-long delay," *Phys. World*, vol. 37, no. 8, p. 8, 2024.

[63] D. G. Whyte *et al.*, "Smaller & sooner: Exploiting high magnetic fields from new superconductors for a more attractive fusion energy development path," *J. Fusion Energ.*, vol. 35, no. 1, pp. 41–53, 2016.

[64] I. H. Hutchinson *et al.*, "First results from Alcator-C-Mod," *Phys. Plasmas*, vol. 1, no. 5, pp. 1511–1518, 1994.

[65] A. Baker, "The spherical tokamak for energy production (STEP) in context: UK public sector approach to fusion energy," *Philos. Trans. A*, vol. 382, no. 2280, p. 20230401, 2024.

[66] A. J. Creely *et al.*, "Overview of the SPARC tokamak," *J. Plasma Phys.*, vol. 86, no. 5, p. 865860502, 2020.

[67] D. Torsello *et al.*, "Expected radiation environment and damage for YBCO tapes in compact fusion reactors," *Supercond. Sci. Technol.*, vol. 36, no. 1, p. 014003, 2022.

[68] J. Knaster *et al.*, "Materials research for fusion," *Nat. Phys.*, vol. 12, no. 5, pp. 424–434, 2016.

[69] D. Torsello *et al.*, "Roadmap for the investigation of irradiation effects in HTS for fusion," *Supercond. Sci. Technol.*, vol. 38, no. 5, p. 053501, 2025.

[70] L. Giannini *et al.*, "Conceptual design studies on the magnet system for the volumetric neutron source (VNS)," *IEEE Trans. Appl. Supercond.*, 2024.

[71] M. Tinkham, *Introduction to Superconductivity*, 2nd ed. McGraw-Hill, 1996.

[72] D. Larbalestier *et al.*, "High-T_c superconducting materials for electric power applications," *Nature*, vol. 414, no. 6861, pp. 368–377, 2001.

[73] A. Devred, *Practical Low-Temperature Superconductors for Electromagnets*. CERN, 2004, no. CERN-2004-006.

[74] A. A. Abrikosov, "On the magnetic properties of superconductors of the second group," *Sov. Phys. J.*, vol. 5, pp. 1174–1182, 1957, translation of Zh. Eksp. Teor. Fiz. 32, 1442 (1957).

[75] J. Bardeen *et al.*, "Microscopic theory of superconductivity," *Phys. Rev.*, vol. 106, no. 1, p. 162, 1957.

[76] B. T. Matthias *et al.*, "Superconductivity of Nb_3Sn," *Phys. Rev.*, vol. 95, no. 6, p. 1435, 1954.

[77] J. K. Hulm and R. D. Blaugher, "Superconducting solid solution alloys of the transition elements," *Phys. Rev.*, vol. 123, no. 5, p. 1569, 1961.

[78] C. B. Müller and E. J. Saur, "Influence of mechanical constraints on the superconducting transition of Nb_3Sn-coated niobium wires and ribbons," in *Advances in Cryogenic Engineering: Proceedings of the 1962 Cryogenic Engineering Conference University of California Los Angeles, California August 14–16, 1962*. Springer, 1963, pp. 574–578.

[79] E. Buehler and H. J. Levinstein, "Effect of tensile stress on the transition temperature and current-carrying capacity of Nb_3Sn," *J. Appl. Phys.*, vol. 36, no. 12, pp. 3856–3860, 1965.

[80] J. G. Bednorz and K. A. Müller, "Possible high T_c superconductivity in the Ba–La–Cu–O system," *Z. Phys. B Condens. Matter*, vol. 64, no. 2, pp. 189–193, 1986.

[81] C. Michel *et al.*, "The oxygen defect perovskite $BaLa_4Cu_5O_{13.4}$, a metallic conductor," *Mater. Res. Bull.*, vol. 20, no. 6, pp. 667–671, 1985.

[82] S. Uchida *et al.*, "High T_c superconductivity of La-Ba-Cu oxides," *Jpn. J. Appl. Phys.*, vol. 26, no. 1A, p. L1, 1987.

[83] C. W. Chu *et al.*, "Evidence for superconductivity above 40 K in the La-Ba-Cu-O compound system," *Phys. Rev. Lett.*, vol. 58, no. 4, p. 405, 1987.

[84] M. Wu *et al.*, "Superconductivity at 93 K in a new mixed-phase Y-Ba-Cu-O compound system at ambient pressure," *Phys. Rev. Lett.*, vol. 58, no. 9, p. 908, 1987.

[85] H. Maeda *et al.*, "A new high-T_c oxide superconductor without a rare earth element," *Jpn. J. Appl. Phys.*, vol. 27, no. 2A, p. L209, 1988.

[86] R. Flu *et al.*, "Metallurgy and critical currents in $YBa_2Cu_3O_7$ wires," *Physica C*, vol. 153, pp. 1574–1579, 1988.

[87] D. Dimos *et al.*, "Superconducting transport properties of grain boundaries in $YBa_2Cu_3O_7$ bicrystals," *Phys. Rev. B Condens. Matter*, vol. 41, no. 7, p. 4038, 1990.

[88] K. Heine *et al.*, "High-field critical current densities in $Bi_2Sr_2Ca_1Cu_2O_{8+X}$/Ag wires," *Appl. Phys. Lett.*, vol. 55, no. 23, pp. 2441–2443, 1989.

[89] F. Kametani *et al.*, "Bubble formation within filaments of melt-processed Bi2212 wires and its strongly negative effect on the critical current density," *Supercond. Sci. Technol.*, vol. 24, no. 7, p. 075009, 2011.

[90] D. Uglietti, "A review of commercial high temperature superconducting materials for large magnets: From wires and tapes to cables and conductors," *Supercond. Sci. Technol.*, vol. 32, no. 5, p. 053001, 2019.

[91] T. Hikata *et al.*, "Ag-Sheathed Bi-Pb-Sr-Ca-Cu-O superconducting wires with high critical current density," *Jpn. J. Appl. Phys.*, vol. 28, no. 1A, p. L82, 1989.

[92] S. Kobayashi *et al.*, "Controlled over-pressure sintering process of Bi2223 wires," *Phys. C: Supercond. Appl.*, vol. 426, pp. 1132–1137, 2005.

[93] Y. Iijima *et al.*, "In-plane aligned $YBa_2Cu_3O_{7-X}$ thin films deposited on polycrystalline metallic substrates," *Appl. Phys. Lett.*, vol. 60, no. 6, pp. 769–771, 1992.

[94] S. I. Kim *et al.*, "Influence of the grain boundary network on the critical current density of deformation-textured $YBa_2Cu_3O_{7-x}$ coated conductors made by metal-organic deposition," *Phys. Rev. B Condens. Matter*, vol. 71, no. 10, p. 104501, 2005.

[95] D. T. Verebelyi *et al.*, "Uniform performance of continuously processed MOD-YBCO-coated conductors using a textured Ni–W substrate," *Supercond. Sci. Technol.*, vol. 16, no. 5, p. L19, 2003.

[96] V. Selvamanickam *et al.*, "Fabrication of 100 A class, 1 m long coated conductor tapes by metal organic chemical vapor deposition and pulsed laser deposition," *Physica C*, vol. 392, pp. 859–862, 2003.

[97] P. N. Arendt and S. R. Foltyn, "Biaxially textured IBAD-MgO templates for YBCO-coated conductors," *MRS Bull.*, vol. 29, no. 8, pp. 543–550, 2004.

[98] V. Selvamanickam *et al.*, "Progress in second-generation HTS wire development and manufacturing," *Physica C*, vol. 468, no. 15-20, pp. 1504–1509, 2008.

[99] A. P. Malozemoff *et al.*, "Low-cost YBCO coated conductor technology," *Supercond. Sci. Technol.*, vol. 13, no. 5, p. 473, 2000.

[100] X. Li *et al.*, "High critical current YBCO films prepared by an MOD process on RABiTS templates," *IEEE Trans. Appl. Supercond.*, vol. 17, no. 2, pp. 3553–3556, 2007.

[101] M. A. Beno *et al.*, "Structure of the single-phase high-temperature superconductor $YBa_2Cu_3O_{7-\delta}$," *Appl. Phys. Lett.*, vol. 51, pp. 57–59, 1987.

[102] Y. Tokura *et al.*, "Broader perspective on the high-temperature superconducting $YBa_2Cu_3O_y$ system: The real role of the oxygen content." *Phys. Rev. B Condens. Matter*, vol. 38, no. 10, pp. 7156–7159, 1988.

[103] J. K. Burdett, "Oxygen ordering and plane-to-chain electron transfer in $YBa_2Cu_3O_{7-\delta}$)," *Physica C*, vol. 191, pp. 282–291, 1992.

[104] B. Roas *et al.*, "Anisotropy of the critical current density in epitaxial $YBa_2Cu_3O_x$ films," *Phys. Rev. Lett.*, vol. 64, no. 4, pp. 479–482, 1990.

[105] J. D. Jorgensen *et al.*, "Structural properties of oxygen-deficient $YBa_2Cu_3O_{7-\Delta}$," *Phys. Rev. B Condens. Matter*, vol. 41, pp. 1863–1877, 1990.

[106] K. N. Yang *et al.*, "High temperature superconductivity in rare-earth (R)-barium copper oxides $(RBa_2)Cu_3O_{9-\sigma}$," *Solid State Commun.*, vol. 63, pp. 515–519, 1987.

[107] R. Unterrainer *et al.*, "Responsibility of small defects for the low radiation tolerance of coated conductors," *Supercond. Sci. Technol.*, vol. 37, no. 10, p. 105008, 2024.

[108] J. L. MacManus-Driscoll *et al.*, "Systematic enhancement of in-field critical current density with rare-earth ion size variance in superconducting rare-earth barium cuprate films," *Appl. Phys. Lett.*, vol. 84, no. 26, pp. 5329–5331, 2004.

[109] P. Przysłupski *et al.*, "Neutron irradiation damage effect on superconducting and normal state properties of the $YBa_2Cu_3O_7$ system," *Physica C*, vol. 153, pp. 345–346, 1988.

[110] L. Civale, "Irradiation processing for flux pinning enhancement in high-T_c superconductors," *Processing And Properties Of High-T_c Superconductors-Volume 1: Bulk Materials*, p. 299, 1991.

[111] G. Blatter *et al.*, "Vortices in high-temperature superconductors," *Rev. Mod. Phys.*, vol. 66, no. 4, p. 1125, 1994.

[112] A. M. Campbell and J. E. Evetts, "Flux vortices and transport currents in type II superconductors," *Adv. Phys.*, vol. 21, no. 90, pp. 199–428, 1972.

[113] L. Civale, "Comparative analysis of particle irradiation and second phases additions on the critical current densities of $YBa_2Cu_3O_7$ single crystals, thin films, and coated conductors: Implications for fusion reactors magnets," *Supercond. Sci. Technol.*, vol. 38, no. 4, p. 043003, 2025.

[114] B. S. Brown and T. H. Blewitt, "Critical current density changes in irradiated Nb_3Sn," *J. Nucl. Mater.*, vol. 80, no. 1, pp. 18–23, 1979.

[115] R. B. Van Dover *et al.*, "Critical currents near 10^6 A cm^{-2} at 77 K in neutron-irradiated single-crystal $YBa_2Cu_3O_7$," *Nature*, vol. 342, no. 6245, pp. 55–57, 1989.

[116] H. W. Weber, "Neutron irradiation effects in high-T_c single crystals," *Physica C*, vol. 185, pp. 309–314, 1991.

[117] A. Wisniewski *et al.*, "Influence of oxygen deficiency and of neutron-induced defects on flux pinning in melt textured bulk $YBa_2Cu_3O_{7-X}$ samples," *Physica C*, vol. 266, no. 3-4, pp. 309–319, 1996.

[118] J. Giapintzakis *et al.*, "Determination of the symmetry of the superconducting pairing state and formation of a low-temperature normal metallic state in YBCO by electron irradiation," Argonne National Lab. (ANL), Argonne, IL (United States), Tech. Rep., 1995. [Online]. Available: https://www.osti.gov/biblio/510599

[119] L. Civale *et al.*, "Vortex confinement by columnar defects in $YBa_2Cu_3O_7$ crystals: Enhanced pinning at high fields and temperatures," *Phys. Rev. Lett.*, vol. 67, no. 5, p. 648, 1991.

[120] ——, "Reducing vortex motion in $YBa_2Cu_3O_7$ crystals with splay in columnar defects," *Phys. Rev. B Condens. Matter*, vol. 50, no. 6, p. 4102, 1994.

[121] M. A. Kirk and H. W. Weber, *Studies of High Temperature Superconductors*. New York: Nova Science Publishers, 1992.

[122] K. Nordlund *et al.*, "Primary radiation damage: A review of current understanding and models," *J. Nucl. Mater.*, vol. 512, pp. 450–479, 2018.

[123] F. F. Komarov, "Defect and track formation in solids irradiated by superhigh-energy ions," *Phys. Usp.*, vol. 46, no. 12, p. 1253, 2003.

[124] R. L. Fleischer *et al.*, *Nuclear Tracks in Solids*. Berkeley: University of California Press, 1975.

[125] R. L. Fleischer, "Ion tracks in solids: From science to technology to diverse applications," *MRS Bull.*, vol. 20, no. 12, pp. 17–21, 1995.

[126] A. I. Larkin and Y. N. Ovchinnikov, "Pinning in type II superconductors," *J. Low Temp. Phys.*, vol. 34, no. 3, pp. 409–428, 1979.

[127] L. A. Openov, "Irradiation-induced suppression of the critical temperature in high-T_c superconductors: Pair breaking versus phase fluctuations," *JETP Lett.*, vol. 81, no. 1, pp. 39–42, 2005.

[128] S. K. Tolpygo *et al.*, "Effect of oxygen defects on transport properties and T_c of $YBa_2Cu_3O_{6+X}$: Displacement energy for plane and chain oxygen and implications for irradiation-induced resistivity and T_c suppression," *Phys. Rev. B Condens. Matter*, vol. 53, no. 18, p. 12462, 1996.

[129] A. Legris *et al.*, "Effects of electron irradiation on $YBa_2Cu_3O_{7-\delta}$ superconductor," *J. Phys. I*, vol. 3, no. 7, pp. 1605–1615, 1993.

[130] R. L. Gray *et al.*, "Molecular dynamics simulations of radiation damage in $YBa_2Cu_3O_7$," *Supercond. Sci. Technol.*, vol. 35, no. 3, p. 035010, 2022.

[131] P. K. Romano and B. Forget, "The OpenMC monte carlo particle transport code," *Ann. Nucl. Energy*, vol. 51, pp. 274–281, 2013.

[132] J. Leppänen *et al.*, "The serpent monte carlo code: Status, development and applications in 2013," *Ann. Nucl. Energy*, vol. 82, pp. 142–150, 2015.

[133] F. Tabbakh, "Particles transportation and nuclear heating in a tokamak by MCNPX and Geant4," *J. Fusion Energ.*, vol. 35, no. 2, pp. 401–406, 2016.

[134] T. Goorley *et al.*, "Initial MCNP6 release overview," *Nucl. Technol.*, vol. 180, no. 3, pp. 298–315, 2012.

[135] Y. Iwamoto *et al.*, "Benchmark study of the recent version of the PHITS code," *J. Nucl. Sci. Technol.*, vol. 54, no. 5, pp. 617–635, 2017.

[136] H. Yashima *et al.*, "Measurement and calculation of radioactivities of spallation products by high-energy heavy ions," *Radiochim. Acta*, vol. 91, no. 12, pp. 689–696, 2003.

[137] L. Sihver *et al.*, "Simulations of the matroshka experiment at the international space station using PHITS," *Radiat. Environ. Bioph.*, vol. 49, no. 3, pp. 351–357, 2010.

[138] F. Calzavara *et al.*, "Systematic monte carlo analysis of binary compounds for neutron shielding in a compact nuclear fusion reactor," *Appl. Sci.*, vol. 15, no. 21, 2025.

[139] K. Shibata *et al.*, "JENDL-4.0: A new library for nuclear science and engineering," *J. Nucl. Sci. Technol.*, vol. 48, no. 1, pp. 1–30, 2011.

[140] I. Meleshenkovskii *et al.*, "Optimization of a 9 Mev electron accelerator bremsstrahlung flux for photofission-based assay techniques using PHITS and MCNP6 monte carlo codes," *Nucl. Instrum. Methods Phys. Res., Sect. B*, vol. 483, pp. 5–14, 2020.

[141] M. C. Han *et al.*, "Multi-threading performance of Geant4, MCNP6, and PHITS monte carlo codes for tetrahedral-mesh geometry," *Phys. Med. Biol.*, vol. 63, no. 9, p. 09NT02, 2018.

[142] Y. S. Yeom *et al.*, "Computation speeds and memory requirements of mesh-type ICRP reference computational phantoms in Geant4, MCNP6, and PHITS," *Health Phys.*, vol. 116, no. 5, pp. 664–676, 2019.

[143] Z. Yang *et al.*, "Inter-comparison of dose distributions calculated by FLUKA, Geant4, MCNP, and PHITS for proton therapy," *EPJ Web Conf.*, vol. 153, p. 04011, 2017.

[144] S. K. Aghara *et al.*, "Shielding evaluation for solar particle events using MCNPX, PHITS and OLTARIS codes," *Life Sci. Space Res.*, vol. 4, pp. 79–91, 2015.

[145] B. Haack *et al.*, "Superconductivity for nuclear fusion: Past, present, and future trends," *Arab. J. Sci. Eng.*, vol. 49, no. 5, pp. 3733–3753, 2024.

[146] L. Sihver *et al.*, "Benchmarking of calculated projectile fragmentation cross-sections using the 3D MC codes PHITS, FLUKA, HETC-HEDS, MCNPX-HI, and NUCFRG2," *Acta Astronaut.*, vol. 63, no. 7, pp. 865–877, 2008.

[147] A. M. Sukegawa *et al.*, "Neutronic analysis of fusion tokamak devices by PHITS," *Prog. Nucl. Sci. Technol.*, vol. 1, pp. 36–39, 2011.

[148] ——, "Conceptual radiation shielding design of superconducting tokamak fusion device by PHITS," *Prog. Nucl. Sci. Technol.*, vol. 2, pp. 375–381, 2011.

[149] C. Fausser *et al.*, "Tokamak D-T neutron source models for different plasma physics confinement modes," *Fusion Eng. Des.*, vol. 87, no. 5, pp. 787–792, 2012.

[150] Z. S. Hartwig *et al.*, "Viper: An industrially scalable high-current high-temperature superconductor cable," *Supercond. Sci. Technol.*, vol. 33, no. 11, p. 11LT01, 2020.

[151] S. Segantin *et al.*, "Preliminary investigation of neutron shielding compounds for ARC-Class tokamaks," *Fusion Eng. Des.*, vol. 185, p. 113335, 2022.

[152] J. W. Bae *et al.*, "ARC reactor neutronics multi-code validation," *Nucl. Fusion*, vol. 62, no. 6, p. 066016, 2022.

[153] A. Q. Kuang *et al.*, "Conceptual design study for heat exhaust management in the ARC fusion pilot plant," *Fusion Eng. Des.*, vol. 137, pp. 221–242, 2018.

[154] J. B. Vetrano, "Hydrides as neutron moderator and reflector materials," *Nucl. Eng. Des.*, vol. 14, no. 3, pp. 390–412, 1971.

[155] R. Heidinger *et al.*, "Observation of radiation damage in HfV_2 and its hydrides by TDPAC," *Phys. Status Solidi A*, vol. 121, no. 2, pp. 445–454, 1990.

[156] H. Kawanishi and S. Ishino, "A tem study of V and V-Lat.% 10b with fast neutron irradiations," *Am. Soc. Test. Mater.*, p. 179, 1990.

[157] B. Muth *et al.*, "A radiation shielding sensitivity analysis based on metal hydrides multilayers," *J. Radiol. Prot.*, vol. 40, no. 3, p. 774, 2020.

[158] J. P. Pollard *et al.*, "Hydrogen desorption kinetics of hafnium hydride powders," *J. Nucl. Mater.*, vol. 604, p. 155499, 2025.

[159] D. Bhardwaj *et al.*, "Fabrication of neutron absorbing metal hydride entrained ceramic matrix shield composites," *Front. Nucl. Eng.*, vol. 3, 2024.

[160] EUROfusion Consortium, "Document referenced by eurofusion idm with uid 2segb8," https://idm.euro-fusion.org/?uid=2SEGB8, access requires login. Accessed: 28 Jan. 2026.

[161] A. Valentine *et al.*, "Neutronics assessment of EU DEMO alternative divertor configurations," *Fusion Eng. Des.*, vol. 169, p. 112663, 2021.

[162] Japan Atomic Energy Agency (JAEA), *PHITS User's Manual, Version 3.35*, Japan Atomic Energy Agency, 2016, accessed: 28 Jan. 2026. [Online]. Available: https://phits.jaea.go.jp/manual/manualE-phits.pdf

[163] "Demo low aspect ratio basic point (process run results)," EUROfusion, Tech. Rep., 2020, available at EUROfusion website.

[164] EUROfusion Consortium, "Eurofusion idm web portal," https://idm.euro-fusion.org/, access to documents requires login via EUROfusion IDM. Accessed: 28 Jan. 2026.

[165] L. Giannini *et al.*, "Overview and assembly strategy of the VNS magnet system: Innovations and challenges," *IEEE Trans. Appl. Supercond.*, vol. 36, no. 3, pp. 1–5, 2025.

[166] Y. Iwamoto *et al.*, "Estimation of reliable displacements-per-atom based on athermal-recombination-corrected model in radiation environments at nuclear fission, fusion, and accelerator facilities," *J. Nucl. Mater.*, vol. 538, p. 152261, 2020.

[167] A. P. Thompson *et al.*, "LAMMPS - a flexible simulation tool for particle-based materials modeling at the atomic, meso, and continuum scales," *Comp. Phys. Comm.*, vol. 271, p. 108171, 2022.

[168] K. Nordlund *et al.*, "Defect production in collision cascades in elemental semiconductors and FCC metals," *Phys. Rev. B Condens. Matter*, vol. 57, pp. 7556–7570, 1998.

[169] J. F. Ziegler *et al.*, "SRIM– the stopping and range of ions in matter," *Nucl. Instrum. Methods Phys. Res. Sect. B*, vol. 268, no. 11-12, pp. 1818–1823, 2010.

[170] A. Stukowski, "Visualization and analysis of atomistic simulation data with OVITO-the Open Visualization Tool," *Model. Simul. Mater. Sci. Eng*, vol. 18, no. 1, p. 015012, 2010.

[171] Y. Ando and K. Segawa, "Magnetoresistance of untwinned $YBa_2Cu_3O_7$ single crystals in a wide range of doping: Anomalous hole-doping dependence of the coherence length," *Phys. Rev. Lett.*, vol. 88, p. 167005, 2002.

[172] A. De Backer *et al.*, "Subcascade formation and defect cluster size scaling in high-energy collision events in metals," *Europhys. Lett.*, vol. 115, no. 2, p. 26001, 2016.

[173] C. Geuzaine and J.-F. Remacle, "Gmsh: A three-dimensional finite element mesh generator with built-in pre- and post-processing facilities," *Int. J. Numer. Meth. Eng.*, vol. 79, no. 11, pp. 1309–1331, 2009.

[174] A. Aimetta *et al.*, "Neutronic analysis of the fusion reactor ARC: Monte carlo simulations with the serpent code," *Fusion Sci. Technol.*, vol. 78, no. 4, pp. 275–290, 2022.

[175] "Java based nuclear information software janis- nuclear energy agency," accessed Aug.2023. [Online]. Available: https://www.oecd-nea.org/jcms/pl_39910/janis

[176] G. W. Morgan, "Some practical considerations in radiation shielding,isotopes division circular B-4," *U.S. Atomic Energy Commission, Oak Ridge*, 1949.

[177] U. Fischer *et al.*, "Neutronics requirements for a DEMO fusion power plant," *Fusion Eng. Des.*, vol. 98, pp. 2134–2137, 2015.

[178] S. Sparacio *et al.*, "Analysis framework for nuclear heating effects on HTS-based conductors in fusion power plants," *IEEE Trans. Appl. Supercond.*, vol. 34, no. 3, pp. 1–8, 2024.

[179] K. Adams *et al.*, "Comparing neutron and helium ion irradiation damage of $REBa_2Cu_3O_{7-\delta}$ coated conductor using X-Ray absorption spectroscopy," *Supercond. Sci. Technol.*, vol. 36, no. 10, p. 10LT01, 2023.

[180] Z. S. Hartwig *et al.*, "The SPARC toroidal field model coil program," *IEEE Trans. Appl. Supercond.*, vol. 34, no. 2, pp. 1–16, 2024.